TECHNISCHE UNIVERSITÄT DRESDEN

MASTERARBEIT

Theory and simulation on nonlinear spin-wave dynamics in magnetic vortices

---

vorgelegt von

Lukas Körber
geboren am 20.02.1994 in Zwickau

Abschlussarbeit zur Erlangung des Hochschulgrades
Master of Science im Studiengang Physik
an der *Fakultät Physik* der Technischen Universität Dresden

angefertigt am

Institut für Ionenstrahlphysik und Materialforschung
Helmholtz-Zentrum Dresden - Rossendorf

eingereicht am 22. Oktober 2019

Dieses Dokument wurde mit LaTeX auf Basis der Vorlage *Masters/Doctoral Thesis* von Steve R. Gunn, Sunil Patel und Vel erstellt.

latextemplates.com/template/masters-doctoral-thesis

Betreuer
Dr. Helmut Schultheiß
Prof. Dr. Jürgen Fassbender

1. Gutachter
Prof. Dr. Jürgen Fassbender

2. Gutachter
Prof. Dr. Sebastian Goennenwein

TECHNISCHE UNIVERSITÄT DRESDEN

Abstract

Fakultät Physik
Helmholtz-Zentrum Dresden - Rossendorf

Master of Science

Theory and simulation on nonlinear spin-wave dynamics in magnetic vortices

by Lukas Körber

One of the fascinating qualities of spin waves (or magnons), which are the elementary excitations in magnetically ordered substances, is their nonlinear behavior at moderate excitation powers. This makes spin waves not only an attractive model system to study general nonlinear systems, but it also provides a way to utilize nonlinear dynamics in possible technical applications. In a ferromagnetic nano disk which is magnetized in the vortex state, the spin-wave modes meet strict boundary conditions and therefore inherit a discrete spectrum. When driven with a large enough excitation field, they can decay into other spin-wave modes within well-defined channels due to a nonlinear process called three-magnon scattering. The aim of this thesis is to explore this phenomenon within nonlinear spin-wave theory and by means of micromagnetic simulations. For this purpose, first the linear dynamics are mapped out and the possible scattering channels are predicted. The stability of these channels with respect to static external fields is studied. Within this context, exotic spin-wave modes which arise in a broken cylindrical symmetry are found. Moreover, a model to predict the temporal evolution of the spin-wave modes is developed within the classical Hamiltonian formalism for nonlinear spin-wave dynamics. Together with micromagnetic simulations, this model is then applied in order to study the power-dependence of three-magnon scattering as well as to uncover a phenomenon called stimulated three-magnon scattering, which may allow for an integration of this nonlinear process in magnonics circuits. The results are compared with Brillouin light-scattering experiments which were conducted prior to this thesis or were motivated by it.

Kurzfassung in deutscher Sprache

Eine der faszinierenden Eigenschaften von Spinwellen (oder Magnonen), den elementaren Anregungen in magnetisch geordneten Substanzen, ist ihr nichtlineares Verhalten bei moderaten Anregungsleistungen. Dies macht Spinwellen nicht nur zu einem attraktiven Modellsystem zur Untersuchung von nichtlinearen Systemen im allgemeinen, sondern bietet auch die Möglichkeit, nichtlineare Dynamik in möglichen technischen Anwendungen zu nutzen. In einer ferromagnetischen Nano-Disk, die im Vortex-Zustand magnetisiert ist, erfüllen die Spinwellenmoden strenge Randbedingungen und weisen daher ein diskretes Spektrum auf. Wenn sie mit einem ausreichend großen Anregungsfeld getrieben werden, können sie aufgrund eines nichtlinearen Prozesses, der Drei-Magnonen-Streuung genannt wird, in wohldefinierten Kanälen in andere Spinwellenmoden zerfallen. Ziel dieser Arbeit ist es, dieses Phänomen innerhalb der nichtlinearen Spinwellentheorie und mittels mikromagnetischer Simulationen zu untersuchen. Dazu wird zunächst die lineare Dynamik ausgearbeitet und die möglichen Streukanäle werden vorhergesagt. Daraufhin wird die Stabilität dieser Kanäle in Bezug auf statische externe Felder untersucht. In diesem Zusammenhang werden exotische Spinwellenmoden gefunden, die durch eine gebrochene Zylindersymmetrie entstehen. Darüber hinaus wird innerhalb des klassischen Hamilton-Formalismus für nichtlineare Spinwellendynamik ein Modell zur Vorhersage der zeitlichen Entwicklung der Spinwellenmoden entwickelt. Dieses Modell wird anschließend zusammen mit mikromagnetischen Simulationen angewendet, um die Leistungsabhängigkeit der Drei-Magnonen-Streuung zu untersuchen und das Phänomen der stimulierten Drei-Magnonen-Streuung aufzudecken, das wiederum eine Integration dieses nichtlinearen Prozesses in magnonischen Schaltungen ermöglichen könnte. Die Ergebnisse werden mit Brillouin-Lichtstreu-Experimenten verglichen, die vor dieser Arbeit durchgeführt oder durch sie motiviert wurden.

Contents

Abstract iii

Acknowledgements vii

List of abbrevations ix

List of symbols xii

1 Motivation 1

2 Theoretical background 3
2.1 Magnetic interactions and equilibrium 3
2.2 Equation of motion of magnetization 7
2.3 Spin waves in ferromagnets 9

3 Overview of methods 19
3.1 Micro-focused Brillouin light-scattering spectroscopy 20
3.2 Micromagnetic simulations 21
3.3 Classical Hamiltonian formalism 22

4 Mapping of the mode spectrum 23
4.1 Initial considerations 23
4.2 Calculation of vortex state 25
4.3 Calculation of the dispersion relation 27

5 Prediction of the scattering channels 31
5.0 Selection rules of three-magnon scattering in a magnetic vortex 32
5.1 Finding the resonant channels 33
5.2 Inclusion of thresholds 39

6 Influence of static external fields 43
6.0 Azimuthal in-plane field 43
6.1 Homogeneous out-of-plane field 44
6.2 Homogeneous in-plane field 46

7 Rate equations for nonlinear dynamics 49
7.1 Linear mode damping 50
7.2 Pumping by external microwave fields 51
7.3 Modeling of thermal magnons 54
7.4 Nonlinear interactions 57
7.5 Comparison with experiment 59

8 Power dependence **61**
- 8.1 Change of time scales . . . 61
- 8.2 Activation of higher-threshold channels and frequency shift . . . 64

9 Towards application: Stimulated three-magnon scattering **67**
- 9.1 Motivation of stimulation and design . . . 68
- 9.2 Stimulation and channel selection below threshold . . . 69
- 9.3 Stimulation above threshold . . . 72

10 Summary and outlook **73**

Own publications and given talks **75**

Bibliography **77**

A Appendix **85**
- A.1 Total energy spectogram . . . 85
- A.2 Calculation of the mode coupling to external fieds . . . 87
- A.3 Implementation of the rate equations in Python . . . 91
- A.4 Analytical solution of the rate equation of the direct mode below threshold . . . 92

Selbstständigkeitserklärung **93**

Acknowledgements

This thesis would not have been possible without the involvement of a number of people. First of all, I would like to thank *Dr. Helmut Schultheiß* for giving me the opportunity to work in his research group all these years, for the respect he has shown me and for always supporting me and my work. His trust and his advice contributed greatly to my development as a scientist. I truly appreciate the time working with him.

Additionally, I would like to thank *Prof. Dr. Jürgen Fassbender* from the Helmholtz-Zentrum Dresden - Rossendorf for supervising and reviewing this thesis. Equal thanks go to *Prof. Dr. Sebastian Goennenwein* from the Technische Universität Dresden for kindly taking over the second opinion.

From the National Academy of Sciences of Ukraine I want to thank *Dr. Roman Verba* for providing data which was used to perform calculations for this thesis. Furthermore, I gratefully acknowledge him and *Prof. Dr. Boris Ivanov* for fruitful scientific discussions as well as the collaboration with them.

I would also like to acknowledge *Dr. Kai Wagner* for the scientific and not so scientific discussions during the past years, furthermore him, *Franziska Wehrmann*, *Tobias Hula*, *Toni Hache* and in particular *Dr. Katrin Schultheiß* for preparing and conducting the experiments which were relevant for this thesis. In addition, I want to thank Katrin for her kindness and the productive collaboration.

For teaching me in micromagnetic simulations, micromagnetism in general and, most importantly, for his friendship, I am deeply grateful to *Dr. Attila Kákay*. I can not remember a day together at the institute where we did not share a laugh.

As for the former and present members of the magnonics research group (and members of the Helmholtz-Zentrum Dresden - Rossendorf in general), I would like to thank all which have not already been mentioned, in particular *Christian Riedel*, *Mauricio Bejarano*, *Tillmann Weinhold*, *Dr. Tobias Kosub*, *Eoghan Cullen* and *Ondrej Wojewoda* for the pleasant and funny times at and off work.

Finally, I want to express special thanks to my *family* and *friends* all of whom play an invaluable role in my life. They contributed strongly to my personal development – they still do – and I am truly grateful for their continuous support, trust and love.

List of abbrevations

μBLS	Brillouin light-scattering microscopy.
BLS	Brillouin light-scattering spectroscopy.
CW	continuous-wave.
FFT	fast Fourier transform.
IP	in-plane.
LLG	Landau-Lifshitz and Gilbert.
ODE	ordinary differential equation.
OOP	out-of-plane.
RF	radio-frequency.
STFT	short-time Fourier transform.

List of symbols

Frequently used quantities

A_ex	exchange stiffness constant	J/m
α_G	Gilbert-damping parameter	
b_crit	critical radio-frequency field magnitude of three-magnon channel	T
b_RF	magnitude of radio-frequency excitation field	T
$\mathbf{B}, \mathbf{b}$	magnetic field vector and its dynamical component	T
c.c.	complex conjugate of the previous term in an equation	
$c_\mathbf{k}$	complex spin-wave amplitude	
$c_{\mathbf{k},\mathrm{th}}$	complex spin-wave amplitude of thermal level	
D	constant diameter (of disk)	m
f, f_RF	frequency and excitation frequency	Hz
γ	modulus of gyromagnetic ratio	rad/Ts
$\Gamma_\mathbf{k}$	linear spin-wave damping rate	Hz
$\mathcal{H}, \hat{\mathcal{H}}$	Hamiltonian function and operator	J
$\mathbf{k}$	wave vector	rad/m
L	constant thickness (of disk)	m
λ_ex	exchange length	m
L_P	experimental microwave power level	dBm
M_s	saturation magnetization	A/m
$\mathbf{M}, \mathbf{m}$	magnetization vector and its dynamical component	A/m
n, m	radial and azimuthal mode index	
$N_\mathbf{k}$	spin-wave (occupation) number	
$N_{\mathbf{k},\mathrm{th}}$	thermal level of spin-wave mode with wave vector **k**	
$\omega, \omega_\mathrm{RF}$	angular frequency and angular excitation frequency	$\mathrm{rad} \cdot \mathrm{Hz}$
$P_\mathbf{k}$	coupling of spin-wave mode to RF field	$\mathrm{rad} \cdot \mathrm{T/s}$
$\boldsymbol{\Phi}_\mathbf{k}$	azimuthal mode profile	

$\Psi_{\mathbf{k}}$	radial mode profile	
R	constant radius (of disk)	m
$\mathbf{r}$	space vector	m
$\hat{\mathbf{S}}$, $\hat{\mathbf{s}}_i$	total spin operator and spin operator at lattice site i	Js
t	time	s
T	absolute temperature	K
$\mathcal{U}$	Hamiltonian function in frequency units	rad · Hz
$\mathcal{U}^{(i)}$	term of the Hamiltonian describing i-magnon interaction	rad · Hz
V	constant volume	m^3
$V_{\mathbf{0},\mathbf{12}}$	three-magnon efficiency	rad · Hz
$W_{\mathbf{12},\mathbf{34}}$	four-magnon efficiency	rad · Hz
x, y, z	carthesian space coordinates	m
ρ, ϕ, z	polar space coordinates	m, rad, m
r, θ, ϕ	sperical space coordinates	m, rad, rad

Constants

$\hbar$	reduced Plank constant	6.62607×10^{-34} Js
μ_0	vacuum permeability	$4\pi \times 10^{-7}$ N/A^2
μ_B	Bohr magneton	9.274×10^{-24} J/T
k_B	Boltzmann constant	1.38×10^{-23} J/K

Chapter 1

Motivation

> *"Productive stupidity means being ignorant by choice. Focusing on important questions puts us in the awkward position of being ignorant. One of the beautiful things about science is that it allows us to bumble along, getting it wrong time after time, and feel perfectly fine as long as we learn something each time."*
>
> – Martin A. Schwartz, *The importance of stupidity in scientific research* [1]

The study of nonlinear dynamical systems is both a fascinating as well as a challenging one. A number of interesting phenomena can emerge in nonlinear systems – such as solitons, multi-stability, wave turbulence and chaos [2–5] – all of which are not present in their linearized counterparts. It is hardly surprising, that predicting the evolution of such a system may be cumbersome, as the underlying equations of motion are of course nonlinear. As a consequence, basic ideas of linear theory, like for instance the superposition principle, do not hold anymore. Nevertheless, it is important to overcome this impediment, because our world is full of nonlinear systems (e.g. fluid dynamics, weather and climate, gravitational waves, social dynamics, neuronal systems [6–10]). In general, all of these systems can be quite different from each other. However, understanding and developing methods for a particular nonlinear system may be very fruitful for studying others.

In the study of spin waves (or magnons), which are the elementary wave-like excitations in magnetically ordered substances, nonlinearities are sometimes treated as a necessary evil. But in fact, a ferromagnet is a perfect model system to study nonlinear dynamics, because almost all important (material) parameters can be obtained experimentally and dynamics can be documented using state-of-the-art magnetic imaging techniques [11, 12]. Moreover, recent advances in patterning nano-sized magnetic structures pave the way for utilizing nonlinear phenomena in possible technical applications which could not be realized in a linear system (at least on a hardware level). On top of that, the excitation power needed to drive spin waves in the nonlinear regime is relatively low. The history of nonlinear magnetization dynamics already started in the 1950s, when Bloemergen, Damon and Wang experimentally investigated the para- and ferromagnetic resonance at large excitation powers [13–15]. Since then, a lot of progress has been made in this field. Today, a number of implementations of nonlinear magnetization dynamics (e.g. auto-oscillations or intensity-dependent spin-wave switching) have been proposed and are under investigation [16–19]. In particular, the nonlinear mode conversion in ferromagnets (multi-magnon scattering) could be of great interest in the development of nonlinear networks. To summarize, the study of nonlinear spin-wave dynamics is not only interesting in terms of fundamental physics but also from a technical point of view.

Recently, it has been shown – with the involvement of the author – that spin-wave modes in magnetic nano disks magnetized in the vortex state can decay into other *secondary* modes by obeying special selection rules [20], if they are excited above a certain threshold power using an oscillating external magnetic field. These selections rules put constraints on the frequency and structure of the secondary modes, resulting in well-defined decay channels. Moreover, the confinement of the spin-wave modes in small magnetic elements leads to an increased stability of the nonlinear precession [21] as well as the appearance of standing waves, further reducing the power needed to drive dynamics into the nonlinear regime. The presence of resonant three-magnon scattering channels in the gigahertz range lead to a rich nonlinear response within magnetic vortices, with certain signals arising directly from the secondary modes, others from second harmonics or frequency mixing. Naturally, these dynamics show a peculiar temporal evolution which can change depending on the input power.

The present work builds on the experimental works by Wehrmann [22], Hula [23] and Schultheiß et al. [20] with the aim of painting a concise picture of the nonlinear spin-wave dynamics at hand. Namely, the scattering channels, their dependence on changing parameters such as excitation power or external fields, as well as the temporal evolution of the concerned spin-wave modes are to be studied. In order to achieve this, theoretical as well as numerical methods will be utilized, comparing the results with experimental data obtained on micrometer-sized ferromagnetic disks made of $Ni_{81}Fe_{19}$ (also referred to as permalloy). Following the theoretical background in Chap. 2, the methods being used will be described in Chap. 3.

In order to understand the nonlinear dynamics, we will first need to find the mode profiles as well as the dispersion of the spin-wave modes in a vortex (Chap. 4). Following up in Chap. 5, we will map the possible scattering channels and discuss which ones will be activated for low excitation powers above a certain nonlinear threshold. The knowledge of these resonant three-magnon channels is important for possible technical applications. After that, we will examine the influence of static external magnetic fields on these channels in Chap. 6.

In Chap. 7, a theoretical model will be developed which will allow to model the temporal evolution of the spin-wave modes that are part of three-magnon scattering processes. After that, this model as well as the acquired knowledge from before is put to use in order to explore the power-dependence of the nonlinear dynamics in Chap. 8 and to touch the idea of possible technical applications in Chap. 9.

In addition to the scientific objectives set out above, the author had several personal goals which will hopefully be shown to be achieved in the course of this thesis. Namely, the author wanted to deepen his knowledge in the theory of magnetism and nonlinear phenomena in general. Furthermore, one goal was to acquire theoretical as well as numerical methods. Last but not least, the author wanted to learn how to *connect the dots*, that is, to explore a research topic in an overarching way while attempting to stand more and more on one's own scientific feet.

Chapter 2

Theoretical background

Before tackling the scientific objectives layed out in the previous chapter, it is necessary to introduce the basic notions of magnetization dynamics, both linear and nonlinear. For this purpose, we will first cover the interactions which lead to the emergence of ferromagnetism, the vortex ground state and ultimately constitute the characteristics of spin waves. After having discussed their quantum mechanical origin, we will quickly employ a very important framework – the *micromagnetic limit* – which allows us to discuss the vortex ground state, as well as the spin-wave excitations, very elegantly. Following up, the equation of motion of magnetization will be introduced, finally leading to the concept of spin waves. We will discuss their linear as well as some of their nonlinear characteristics in the important exemplary case of thin magnetic film. In order to discuss nonlinear phenomena, it will be useful to introduce the *classical Hamiltonian formalism* for nonlinear spin-wave dynamics.

A much more detailed introduction into the basics of magnetism is found in the excellent book by Blundell [24], whereas the theory of magnetization dynamics and spin waves is covered in great detail in the works of reference by Stancil and Prabhakar [25] or Gurevich and Melkov [26]. A very comprehensive investigation of nonlinear spin-wave dynamics was written by Victor S. L'vov [4] and will be referenced a couple of times during the course of this thesis.

As a personal statement: It was the author's intention to present the following theoretical chapter as deductive as possible. Several steps along the way (such as carrying out the micromagnetic limit) are typically taken for granted and left out for good reasons. However, for the sake of epistemology as well as for personal education, the author decided to explicitly include such steps.

2.1 Magnetic interactions and equilibrium

2.1.1 Quantum mechanical origin of ferromagnetism

Substances which exhibit a *spontaneous* magnetization in the absence of an external magnetic field are called magnetically ordered [26]. In materials of this nature, the uncompensated elementary magnetic moments of the electrons $\hat{\boldsymbol{\mu}}_i$ within the respective lattice align with each other spontaneously due to the so-called *exchange interaction*. This interaction is a consequence of the Pauli exclusion principle and can be expressed using the effective Hamiltonian operator

$$\hat{\mathcal{H}}_{\text{exch}} = -\sum_{\langle ij \rangle} J_{ij} \hat{\mathbf{s}}_i \cdot \hat{\mathbf{s}}_j. \tag{2.1}$$

Here, $\hat{\mathbf{s}}_i$ and $\hat{\mathbf{s}}_j$ are the electron spin operators at lattice site i and j, respectively. The *exchange integral* J_{ij} is in the simplest case dependent on the overlap of the electronic wave functions.[1] In most cases, this overlap is only large for nearest neighbors $\langle ij \rangle$. For this reason, it is often enough to reduce the summation over all lattice-site combinations to a nearest neighbor sum. The Hamiltonian operator defined by Eq. 2.1 is also called the *Heisenberg Hamiltonian*. Strictly speaking, it only describes insulating materials, where the spin carriers (electrons) are localized. The exchange interaction in metallic alloys (such as $Ni_{81}Fe_{19}$) is more properly treated within the Hubbard model, more specifically the Stoner mean-field theory [27, 24, pp. 141-163]. However, in certain cases the exchange can be described in a form very similar to the Heisenberg Hamiltonian. In the sense of a tight-binding approximation and for the sake of this argument, we will assume that the electrons travel within the metal only by *hopping* from one lattice site to the other such that each site is singly occupied at all times. As a result, we may use the Heisenberg Hamiltonian again, at least in a phenomenological manner.

In a substance, in which $J_{ij} > 0$, a parallel alignment of the electronic spins is preferred. The material is then called *ferromagnetic* and can be described by a spontaneous magnetization $\mathbf{M}$ within a certain unit volume ΔV, which is constituted by all magnetic moments

$$\mathbf{M} = \frac{1}{\Delta V} \sum_{i \in \Delta V} \langle \hat{\boldsymbol{\mu}}_i \rangle \,, \tag{2.2}$$

with $\langle \ldots \rangle$ denoting the expectation value of a quantum mechanical operator. For the sake of simplicity and to streamline the present theoretical introduction to some extent, we will assume that the total magnetic moment of an electron can be approximated by only considering the magnetic moment produced by the electron spin,

$$\hat{\boldsymbol{\mu}}_i \approx -\frac{g\mu_B}{\hbar} \hat{\mathbf{s}}_i, \tag{2.3}$$

with the anomalous g-factor of the electron, the Bohr-magneton μ_B and the reduced Planck constant $\hbar$. This approximation is allowed for example if the orbital magnetic moment is *quenched* (its expectation value is almost zero due to the symmetry of the respective crystal). This spin-only approximation is reasonable e.g. for crystals of the transition metals nickel, iron or cobalt (and their alloys) [24, pp. 48-50, 28, p. 406], all of which are ferromagnetic at room-temperature.

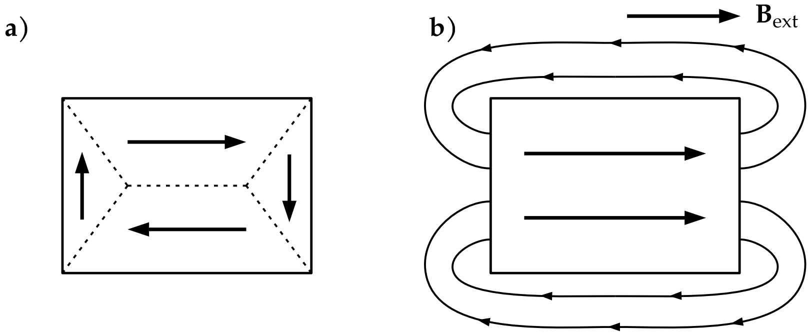

FIGURE 2.1: Schematic magnetization and stray field of a magnetic element which is **a)** unsaturated and divided into domains or **b)** has been saturated into the single-domain state by an external field.

If a magnet is fully saturated, meaning that all magnetic moments are aligned, it has reached its so-called *saturation magnetization* M_S which is the maximum possible modulus of magnetization for the material at hand. However, most ferromagnetic bodies of finite size are observed to be not fully magnetized, but are rather divided into smaller regions in which the magnetic moments are parallel again (see Fig. 2.1a). The formation of these domains is a consequence of the *dipolar interaction* (or dipole-dipole interaction) between the magnetic moments,

---

[1] This simple case is referred to as *direct exchange*.

$$\hat{\mathcal{H}}_{\text{dip}} = \frac{g^2\mu_0\mu_B^2}{4\pi\hbar^2}\sum_{ij}\frac{3(\hat{\mathbf{s}}_i\cdot\mathbf{r}_{ij})(\hat{\mathbf{s}}_j\cdot\mathbf{r}_{ij}) - r_{ij}^2\hat{\mathbf{s}}_i\cdot\hat{\mathbf{s}}_j}{r_{ij}^5} \tag{2.4}$$

which favors an anti-parallel alignment of the spins to minimize the overall stray field – or in other words – to close the magnetic flux. This demagnetizing effect of the dipolar interaction can be overcome by applying an external magnetic field $\mathbf{B}_{\text{ext}}$ described the by *Zeemann interaction*

$$\hat{\mathcal{H}}_{\text{Z}} = \frac{g\mu_B}{\hbar}\sum_i \hat{\mathbf{s}}_i\cdot\mathbf{B}_{\text{ext}}. \tag{2.5}$$

If the external field is strong enough, the magnetic moments will align parallel with the field until the magnet reaches saturation again (see Fig. 2.1b).[2]

The dipolar interaction is much weaker than exchange, but is – in contrast to the latter – a long-range interaction. It will therefore play an important role in the formation of ground states in larger magnetic structures as well as in the dynamics of long-wavelength spin waves.

In certain cases, other phenomena such as crystal anisotropy, magnetostriction or the asymmetric exchange interaction between electrons (known as Dzyaloshinskii–Moriya interaction) may be of importance, too, and need to be added to the Hamiltonian $\hat{\mathcal{H}} = \hat{\mathcal{H}}_{\text{exch}} + \hat{\mathcal{H}}_{\text{dip}} + \hat{\mathcal{H}}_{\text{Z}}$. As this is not the case in the present thesis, such interactions remain only mentioned.

2.1.2 Micromagnetic limit

On the length scales of magnetic elements which can span several nanometers or even micrometers, it is often not necessary to treat the magnetic properties of a solid on the level of individual quantum mechanical spins. In fact, it will be more practical to treat magnetization dynamics in the *micromagnetic limit* which is both classical on the one hand and a continuum theory on the other hand.

In a solid body, where the number of electrons is macroscopic ($\sim 10^{23}$), the modulus of the total spin S becomes very large. In the limit of $S \to \infty$, the uncertainty of the spin components become negligible and one can replace the operators with real three-dimensional vectors $\mathbf{s}_i \in \mathbb{R}^3$.[3] Due to the strengh of the exchange interaction, one can assume the angle β_{ij} between neighboring spins to be small and write for the exchange interaction

$$\mathcal{H}_{\text{exch}} = -Js^2\sum_{\langle ij\rangle}\cos\beta_{ij} \approx \text{const.} + \frac{Js^2}{2}\sum_{\langle ij\rangle}\beta_{ij}^2. \tag{2.6}$$

---

[2] The usual minus sign is missing in the expression of the Zeemann energy, because we have defined the magnetic moment to be anti-parallel to the spin.

[3] One can rescale the spin operators $\hat{\mathbf{s}}_i$ by S and then show that the well known commutation relations for quantum mechanical angular momenta vanish for $S \to \infty$.

The constant term is the energy of the equilibrium state. As it will not affect the dynamics, we can ignore it at this point. The next approximation towards micromagnetism is taking the continuum limit and ignoring the discrete nature of the lattice. The summation becomes an integral over the whole volume V of the lattice. The angle β_{ij} can be replaced by a vector gradient of the reduced magnetization $\mathbf{M}/M_s$ which is now a continuous function of real space,

$$\mathcal{H}_{\text{exch}} = \frac{A_{\text{ex}}}{M_s^2} \int_V \mathrm{d}^3 r \, (\nabla \mathbf{M}(\mathbf{r}))^2 = \frac{\mu_0 \lambda_{\text{ex}}^2}{2} \int_V \mathrm{d}^3 r \, (\nabla \mathbf{M}(\mathbf{r}))^2, \tag{2.7}$$

where $A_{\text{ex}} = 2Js^2 Z/a$ is the so-called *exchange stiffness constant* (a is the lattice constant and Z is the coordination number of the lattice). It is also quite common to express the exchange energy using the *exchange length* $\lambda_{\text{ex}} = \sqrt{2A_{\text{ex}}/\mu_0 M_s^2}$, which defines the characteristic length scale of the micromagnetic exchange. For $\text{Ni}_{81}\text{Fe}_{19}$, which is the material used in this thesis, this length scale is approximately 5 nm. In a similar fashion the micromagnetic dipolar energy becomes

$$\mathcal{H}_{\text{dip}} = \frac{1}{2} \frac{\mu_0}{4\pi} \iint_V \mathrm{d}^3 r \, \mathrm{d}^3 r' \, \frac{(\nabla_{\mathbf{r}} \mathbf{M}(\mathbf{r}))(\nabla_{\mathbf{r}'} \mathbf{M}(\mathbf{r}'))}{|\mathbf{r} - \mathbf{r}'|}. \tag{2.8}$$

Finally, the continuum limit of the Zeemann energy is simply

$$\mathcal{H}_Z = - \int_V \mathrm{d}^3 r \, \mathbf{M}(\mathbf{r}) \cdot \mathbf{B}_{\text{ext}}(\mathbf{r}). \tag{2.9}$$

The strength of the micromagnetic limit is that the microscopic origins of the magnetic interactions are abstracted into the continuous vector field $\mathbf{M}(\mathbf{r})$ as well as the material parameters A_{ex}, M_s and so forth. In particular, in the rudimentary micromagnetic energy functionals, there is no difference between magnetic insulators or metallic ferromagnets such as permalloy. Moreover, magnetic ground states or dynamic properties can be obtained using methods of vector calculus.

2.1.3 The vortex state

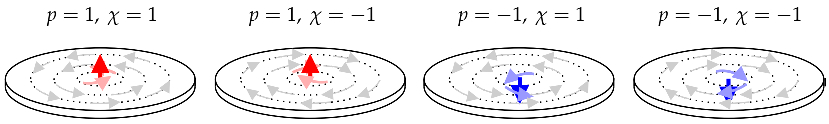

FIGURE 2.2: Examples for different vortices with varying polarity p and vorticity χ. The color code illustrates the out-of-plane-component $M_{\text{eq},z}$ from negative extremum (blue) to positive extremum (red).

Depending on its geometry and size, a ferromagnetic body can have various equilibrium configurations $\mathbf{M}_{\text{eq}}(\mathbf{r})$. In the case of thin micrometer-sized disks (which are relevant for this thesis), the most probable spontaneously forming ground state is a (circular) magnetic vortex.[4] In such a configuration, the static equilibrium magnetization continuously rotates around the center of the disk and is in-plane almost everywhere, which allows for almost zero stray field. The sense of rotation is denoted by the vorticity $\chi = \pm 1$. Due to the presence of the exchange interaction, the magnetization must be sufficiently continuous and therefore, to avoid a point of singularity, has to point out of the disk plane in a small region around the center of the disk, called the *vortex core*. The size of this core is determined by the interplay between exchange and dipolar interaction and is usually in the order of the exchange length λ_{ex}. The direction in which the core points is denoted by the vortex polarity $p = \pm 1$. In Fig. 2.2, we see the four possible states of a circular vortex in a small magnetic disk.

---

[4] It can be noted that depending on the dimensions and aspect ratio the magnetic disk, different configurations other than the vortex state might be favored (e.g. as presented in [29]).

These four states are energetically degenerate except with respect to the application of an external out-of-plane field $\mathbf{B} = B_z \mathbf{e}_z$. In this case, the two possible vortex polarities will be energetically split. The equilibrium magnetization can be obtained in the continuum limit by minimizing the energy functional $\mathcal{H} = \mathcal{H}_{\text{exch}} + \mathcal{H}_{\text{dip}} + \mathcal{H}_{\text{Z}} + \ldots$ with the terms given in the previous sections. In cylindrical coordinates (with z-axis oriented along the symmetry axis of the disk), it can be written as

$$\mathbf{M}_{\text{eq}}(\mathbf{r}) = M_s(\chi \sin\theta(\rho)\mathbf{e}_\phi + p\cos\theta(\rho)\mathbf{e}_z). \tag{2.10}$$

Here, $\theta(\rho)$ is the spherical angle denoting the vortex core profile. It takes the value of $\pi/2$ almost everywhere except in the small vortex core region. An exact expression for this function in the case of soft magnetic materials, such as permalloy, is for example given approximately by the Usov-Peschany ansatz [30]. A proper numerical study describing the exact vortex profile was performed by Ha, Hertel and Kirchner [31].

2.2 Equation of motion of magnetization

Due to the strong contribution of the exchange interaction the modulus of the magnetization vector $\mathbf{M}(\mathbf{r}, t)$ must – at least for sufficiently low temperatures – be constant in time [32, p. 44]. As a consequence, the variation of magnetization in time can only be of a precessional character (in leading order),

$$\frac{\partial \mathbf{M}}{\partial t} = -\gamma[\mathbf{M} \times \mathbf{B}_{\text{eff}}], \tag{2.11}$$

where $\gamma = g\mu_B/\hbar$ is the modulus of the gyromagnetic ratio of the electron and $\mathbf{B}_{\text{eff}}(\mathbf{r}, t)$ is the effective magnetic field. This torque equation of motion can be seen as a continuum limit of the precessional motion an elementary magnetic moments in an effective magnetic field.[5] This effective field $\mathbf{B}_{\text{eff}}(\mathbf{r}, t)$, which at this point has come out of the blue, is given by the fact that the torque equation Eq. 2.11 must be conservative. In other words, the total energy $\mathcal{H}$, which is a functional of the magnetization, must be constant in time,

$$\begin{aligned}\frac{\partial \mathcal{H}}{\partial t} &= \int_V \mathrm{d}^3 r \, \frac{\delta \mathcal{H}}{\delta \mathbf{M}(\mathbf{r}, t)} \cdot \frac{\partial \mathbf{M}(\mathbf{r}, t)}{\partial t} \\ &= -\gamma \int_V \mathrm{d}^3 r \, \frac{\delta \mathcal{H}}{\delta \mathbf{M}(\mathbf{r}, t)} \cdot [\mathbf{M} \times \mathbf{B}_{\text{eff}}] \\ &\equiv 0\end{aligned} \tag{2.12}$$

---

[5] For the curious reader: The micromagnetic torque equation can be seen as the classical continuum limit of the equation of motion of the spin operator $\hat{\mathbf{s}}_i$ in the Heisenberg picture, which is $\mathrm{d}\hat{\mathbf{s}}_i/\mathrm{d}t = i/\hbar[\hat{\mathcal{H}}, \hat{\mathbf{s}}_i]$ (with $[\cdot, \cdot]$ being the commutator of two operators on a Hilbert space).

In order for this integral to vanish for all possible $\mathbf{M}(\mathbf{r}, t)$, the varation $\delta\mathcal{H}/\delta\mathbf{M}$ and the effective field $\mathbf{B}_{\text{eff}}$ must be parallel. The exact proportionality factor can be determined to be -1 [4]. This means that the effective field is

$$\mathbf{B}_{\text{eff}} = -\frac{\delta\mathcal{H}}{\delta\mathbf{M}(\mathbf{r}, t)}, \tag{2.13}$$

and one can also write,

$$\frac{\partial\mathbf{M}}{\partial t} = \gamma\left[\mathbf{M} \times \frac{\delta\mathcal{H}}{\delta\mathbf{M}(\mathbf{r}, t)}\right]. \tag{2.14}$$

However, considering the effective field $\mathbf{B}_{\text{eff}} = \mathbf{B}_{\text{ext}} + \mathbf{B}_{\text{exch}} + \mathbf{B}_{\text{dip}} + \ldots$, which is constituted of the external field as well as the fields produced by the magnetization itself, allows for a much more intuitive understanding of the equation of motion of magnetization. For example, we observe, that in equilibrium, $\mathbf{M}$ and $\mathbf{B}_{\text{eff}}$ must be parallel to each other. Only when there is a component of the effective field – for example an oscillatory external field – which is non-parallel to the magnetization, it will start to precess. In a real magnetic sample, the magnetization will not maintain its precessional motion but rather spiral on a loxodrome back into its equilibrium configuration due to the presence of damping (see Fig. 2.3). The reason of this energy dissipation is the coupling of the magnetic oscillations to thermal baths such as the photonic or the electronic system. The influence of viscous damping was included in phenomenological manner by Gilbert [33, 34] as

$$\frac{\partial\mathbf{M}}{\partial t} = -\gamma[\mathbf{M} \times \mathbf{B}_{\text{eff}}] + \frac{\alpha_G}{M_s}\left[\mathbf{M} \times \frac{\partial\mathbf{M}}{\partial t}\right]. \tag{2.15}$$

with the dimensionless phenomenological Gilbert damping constant α_G. The torque equation Eq. 2.15 is called the Landau-Lifshitz and Gilbert (LLG) equation of motion and is widely used in magnetization dynamics.

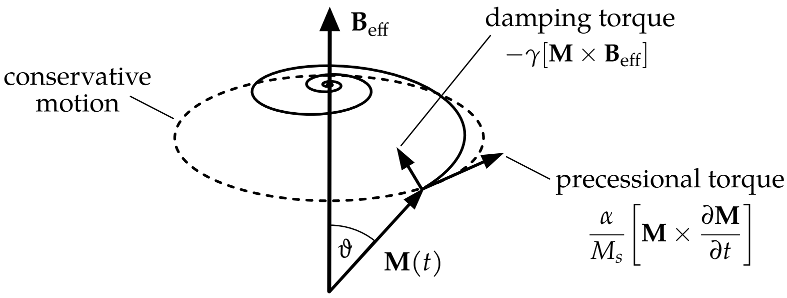
$\mathbf{B}_{\text{eff}}$
damping torque
$-\gamma[\mathbf{M} \times \mathbf{B}_{\text{eff}}]$
conservative motion
precessional torque
$\frac{\alpha}{M_s}\left[\mathbf{M} \times \frac{\partial\mathbf{M}}{\partial t}\right]$
ϑ
$\mathbf{M}(t)$

FIGURE 2.3: Illustration of the precessional motion of magnetization at a certain point in space, according to the LLG equation of motion.

The damping of individual oscillation modes (spin waves) will lead to a finite life time as well as a nonzero line width of these modes. Moreover, it will be of great importance for the nonlinear phenomena studied in this thesis. Therefore, we will address this point again in more detail in Sec. 2.3.3 as well as in Chap. 5 and Chap. 7.

2.3 Spin waves in ferromagnets

We have already discussed in the previous chapter that the magnetization $\mathbf{M}(\mathbf{r},t)$ of a ferromagnetic body will locally perform a precessional motion around the effective field if it is brought out of its equilibrium. This precessional motion can propagate as a wave-like excitation within the ferromagnet. These low-energy excitations are called spin waves. Their quantum mechanical origin are the quasi-particle magnons, which are found as the low-energy excited states of the Hamiltonian operator discussed in Sec. 2.1.1. Although, spin waves described in micromagnetism are only the classical long-wavelength limit of quantum mechanical magnons, it is common to use both terms equivalently and, within the course of this thesis, the term *magnon* instead of *spin wave* will sometimes be used for the sake of brevity. Moreover, in order to discuss nonlinear spin-wave dynamics, it is quite useful to call upon the quasi-particle picture.

2.3.1 Linear spin-wave dynamics

In order to obtain a dispersion for the spin-wave modes in a ferromagnet, one has to linearize the lossless LLG equation ($\alpha_G = 0$) by splitting the magnetization into a static part and a dynamical component

$$\mathbf{M}(\mathbf{r},t) = \mathbf{M}_{\text{eq}}(\mathbf{r}) + \mathbf{m}(\mathbf{r},t), \tag{2.16}$$

and then keep only the terms up to first order in the dynamical component $\mathbf{m}$, which is perpendicular to $\mathbf{M}_{\text{eq}}$. The effective field is split in the same fashion. Finally, the resulting linearized LLG equation

$$\frac{\partial \mathbf{m}}{\partial t} = -\gamma\left[\mathbf{M}_{\text{eq}} \times \mathbf{b}(t) + \mathbf{m}(t) \times \mathbf{B}_{\text{eq}}\right] \tag{2.17}$$

can be solved by expanding the dynamical component into a serious of harmonic waves,

$$\mathbf{m}(\mathbf{r},t) = \sum_{\mathbf{k}} (\mathbf{m}_{\mathbf{k}}(\mathbf{r}) e^{-i\omega_{\mathbf{k}} t} + \text{c.c.}) \tag{2.18}$$

Here, $\mathbf{k}$ is the wave vector, $\mathbf{m}_{\mathbf{k}}(\mathbf{r})$ is the spatial mode profile and $\omega_{\mathbf{k}}$ is the angular frequency of the respective spin-wave mode. The abbreviation "c.c." denotes the complex conjugate of the term in front of it.[6]

Here, we will discuss the important case of spin waves propagating in a thin-film ferromagnet, which is homogeneously magnetized in-plane. An approximate dispersion for this case was first calculated by Kalinikos and Slavin [36],

$$\omega_l^2(\mathbf{k}) = \begin{cases} \left[\omega_0 + \omega_M \lambda_{\text{ex}}^2 k_l^2\right] & \text{for} \quad \mathbf{k} \parallel \mathbf{M}_{\text{eq}} \\ \qquad \times \left[\omega_0 + \omega_M \lambda_{\text{ex}}^2 k_l^2 + \omega_M (1 - K_{ll})\right] & \\ & \\ \left[\omega_0 + \omega_M \lambda_{\text{ex}}^2 k_l^2 + \omega_M K_{ll}\right] & \text{for} \quad \mathbf{k} \perp \mathbf{M}_{\text{eq}} \\ \qquad \times \left[\omega_0 + \omega_M \lambda_{\text{ex}}^2 k_l^2 + \omega_M (1 - K_{ll})\right] & \end{cases} \tag{2.19}$$

---

[6] The solutions of the linearized equation of motion always come in complex conjugated pairs (see e.g. [35]).

with

$$\begin{aligned}\omega_0 &= \gamma B_{\text{ext}},\\ \omega_M &= \gamma\mu_0 M_s,\\ k_l^2 &= k^2 + \left(\frac{l\pi}{d}\right)^2,\\ K_{ll} &= \frac{k^2}{k_l^2}\left[1 - \left(\frac{2}{1+\delta_{0l}}\right)\frac{k^2}{k_l^2}\left(\frac{1-(-1)^l e^{-|k|d}}{|k|d}\right)\right].\end{aligned} \tag{2.20}$$

Here, **k** is the wave-vector component in the film plane, l denotes the index of quantization along the film thickness d. The exchange length is again given by $\lambda_{\text{ex}} = \sqrt{2A_{\text{ex}}/\mu_0 M_s^2}$.

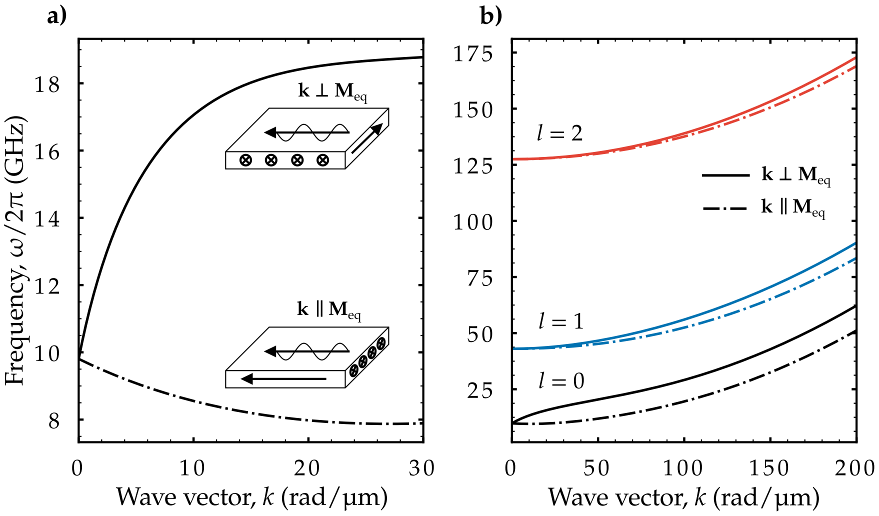

FIGURE 2.4: Approximate spin-wave dispersion in an infinitely extended film which is in-plane magnetized. **a)** shows the two possible species in the dipolar regime, the surface waves ($\mathbf{k} \perp \mathbf{M}_{\text{eq}}$) and the backward-volume waves ($\mathbf{k} \parallel \mathbf{M}_{\text{eq}}$), for the lowest order modes ($l = 0$) in a film with 75 nm thickness. Higher order modes in the exchange regime are presented in **b)** in a film with 20 nm thickness. All curves were obtained using the formulas 2.19 with typical material parameters for Permalloy: saturation $M_s = 830\,\text{kA}\,\text{m}^{-1}$, exchange stiffness $A_{\text{ex}} = 16\,\text{pJ}\,\text{m}^{-1}$, gyromagnetic ratio $\gamma/2\pi = 29\,\text{GHz}\,\text{T}^{-1}$ and static external field $B_{\text{ext}} = 100\,\text{mT}$.

Although, this dispersion describes the waves propagating in an infinitely extended film, it will introduce some important qualities of spin waves which we will observe for the spin-wave modes in a finite magnetic disk, as well.

(i) For small wave vectors, the dispersion is strongly anisotropic, with its origin in the dipolar interaction. For the case of $\mathbf{k} \parallel \mathbf{M}_{\text{eq}}$ (called backward-volume waves), the dispersion has a negative slope, whereas for $\mathbf{k} \perp \mathbf{M}_{\text{eq}}$ (called magnetostatic surface waves or sometimes Damon-Eshbach waves) the frequency increases strongly with the wave vector (see Fig. 2.4a).

(ii) Depending on the external field, there is a band gap in the spin-wave spectrum. In a vortex disk, this band gap will be present even without an external field, as it arises from the confinement of the possible spin-wave modes. It will play a crucial role in the set of possible three-magnon scattering channels.

(iii) With increasing wave vector, neighboring magnetic moments will be more and more tilted to each other, leading to an increase in exchange energy. This in return leads to an increase of the frequency $\omega \propto k^2$ (see Fig. 2.4b).

(iv) Over the film thickness, only a discrete set of wave-vectors is allowed due to the confinement in this dimension. These perpendicular standing spin waves with quantization index $l > 0$ are much higher in frequency (see Fig. 2.4b). Because of this, they can be ignored during the course of this thesis.

2.3.2 Nonlinear spin-wave dynamics

The LLG equation is a nonlinear differential equation which means that spin-wave dynamics are inherently nonlinear, too. Physically speaking, an individual spin wave will always perturb the medium it is propagating in. As a consequence, it will change the effective field that itself and other spin-wave modes experience. Such a feedback loop can lead to interesting effects such as frequency shift or multi-magnon scattering.

By linearizing the torque equation, the dispersion as well as the mode profiles can be obtained. However, all nonlinear effects have been neglected taking this step. Describing dynamics for which the dynamical component of the magnetization $\mathbf{m}(\mathbf{r}, t)$ is not small makes analytical considerations cumbersome because the initial torque equation is nonlinear. In this case, terms proportional to $\mathcal{O}(\mathbf{m}^2)$ can not be neglected anymore. Although, numerical integration of the full torque equation can still be of use, any attempt to include higher-order terms into the linearized LLG is very difficult (but neither impossible nor uncommon for $k = 0$ [37, 38, 26, pp. 234-237]).

A very helpful solution to study nonlinear spin-wave dynamics is to make use of the quasi-particle picture and express all nonlinear processes as interactions of different *linear* spin-wave modes. In quantum mechanics, this would correspond to writing the Hamiltonian from Sec. 2.1.1 in second quantization, meaning in terms of creation and annihilation operators of the different spin-wave modes. Before we formalize this idea within the continuum limit, we briefly introduce some of the phenomena which will be important for this thesis.

Multi-magnon scattering

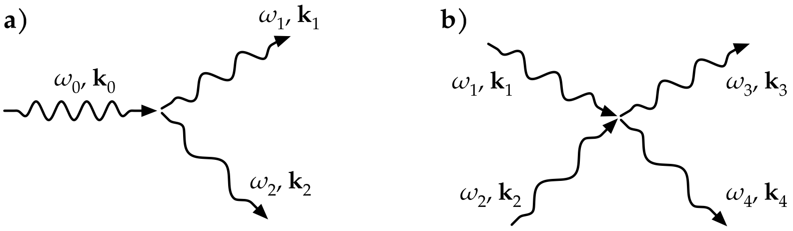

FIGURE 2.5: Examplary processes of **a)** three-magnon scattering and **b)** four-magnon scattering.

Processes of multi-magnon scattering refer to the conversion of different spin-wave modes into others. It is often enough to restrict considerations to processes of three or four waves interacting with each other. All scattering processes that include more spin-wave modes will contribute less and less to the total magnetic energy, that is, to the Hamiltonian. All processes of multi-magnon scattering have to conserve both the total energy as well as the total momentum,

$$\sum_{\text{in}} \omega_i = \sum_{\text{out}} \omega_j \quad \text{and} \quad \sum_{\text{in}} \mathbf{k}_i = \sum_{\text{out}} \mathbf{k}_j. \tag{2.21}$$

This is the reason, why three-magnon scattering can be *forbidden* or *non-resonant* in some parts of the spin-wave spectrum, whereas four-magnon scattering is always allowed.

Multi-magnon scattering processes are also often called *parametric*. Due to the intrinsic damping of the spin-wave modes, often a certain threshold in wave amplitude needs to be overcome, in order for these processes to happen (we will come back to this point in Sec. 5.2).

Nonlinear frequency shift

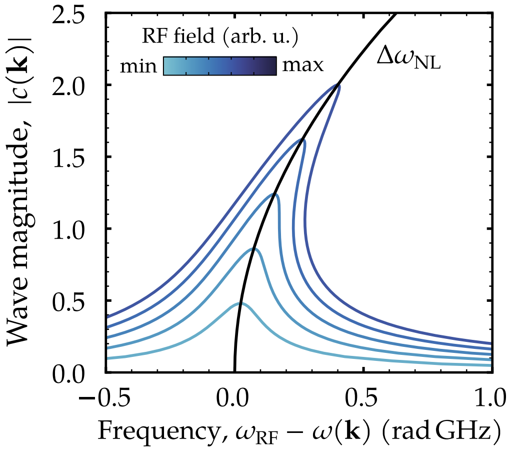

FIGURE 2.6: Fold-over effect in the resonance curve of a certain spin-wave mode due to the nonlinear frequency shift. The resonance curve was obtained by solving Eq. 2.24 for the frequency of the excitation field ω_{RF} and then plotting the resulting two possible solutions for the toy parameters Γ, $W = 100\,\mathrm{MHz}$ as a function of the magnitude $|c(\mathbf{k})|$.

Much like in a driven classical pendulum for larger angles, the frequency of a spin-wave mode will change with increasing amplitude, leading to a *fold-over* of the resonance curve of the wave (see Fig. 2.6). Moreover, a large amplitude of a certain spin-wave mode can also influence the frequency of other modes, as it changes the effective field. The latter phenomenon is also referred to as *nonlinear cross-shift*. Under the assumption, that for weakly nonlinear excitation, the precessional motion of the magnetization will still be harmonic and only its frequency will be shifted, the nonlinear frequency of a spin-wave mode is often written as

$$\omega_{\mathrm{NL}}(\mathbf{k}) = \omega(\mathbf{k}) + \Delta\omega_{\mathrm{NL}}(\mathbf{k}) \tag{2.22}$$

with

$$\Delta\omega_{\mathrm{NL}}(\mathbf{k}) = \sum_i W_i |c(\mathbf{k}_i)|^2. \tag{2.23}$$

Moreover, $c(\mathbf{k}_i)$ are the yet-to-be-defined complex amplitudes of the spin waves in the system and W_i are certain frequency-cross-shift parameters. Within the classical Hamiltonian formalism, which will be introduced in the next section, these frequency-shift parameters can be identified in lowest order of approximation as the four-magnon-scattering efficiencies of the spin-wave modes in the system scattering with the mode that is shifted.

For example, the resonance curve of a spin-wave mode which is excited by an external radio-frequency (RF) field, including only the nonlinear self-shift (here W) [39, 40], is given by

$$|c(\mathbf{k})| = \frac{P(\mathbf{k}) b_{\mathrm{RF}}}{\sqrt{\Gamma^2 + (\omega(\mathbf{k}) + W|c(\mathbf{k})|^2 - \omega_{\mathrm{RF}})^2}}, \tag{2.24}$$

with the coupling $P(\mathbf{k})$ of a the mode to a RF field with magnitude b_{RF}. The damping rate of mode is denoted by Γ. We will cover these parameters later in detail in Chap. 7, when constructing rate equations to describe the temporal evolution of spin-wave modes.

2.3.3 Classical Hamiltonian formalism for nonlinear spin-wave dynamics

In reminiscence of second quantization, within the classical Hamiltonian formalism for spin waves, the total magnetic energy is expressed in terms of the time-dependent spin-wave amplitudes $c_{\mathbf{k}}(t) = c(\mathbf{k}, t)$ and $c^*_{\mathbf{k}}(t) = c^*(\mathbf{k}, t)$ with a given dispersion law $\omega_{\mathbf{k}} = \omega(\mathbf{k})$. These complex amplitudes are classical analoga of the bosonic annihilation and creation operators $\hat{c}_{\mathbf{k}}$ and $\hat{c}^\dagger_{\mathbf{k}}$ of magnons. We will cover, how they are obtained from the continuum magnetization, shortly. The spin-wave Hamiltonian (which we will call $\mathcal{U}$), is then written as a pertubative expansion in terms of increasing number of spin-wave amplitudes,

$$\mathcal{U} = \mathcal{U}^{(0)} + \mathcal{U}^{(1)} + \mathcal{U}^{(2)} + \mathcal{U}_{\mathrm{int}}, \tag{2.25}$$

with $\mathcal{U}^{(0)} = \mathrm{const}$ and not important for the following dynamical equations. The term $\mathcal{U}^{(1)}$ is often set nil due to the assumption to be in equilibrium in the absence of spin-waves. However, it will be nonzero in the presence of external pumping. The second-order term,

$$\mathcal{U}^{(2)} = \sum_{\mathbf{k}} \omega_{\mathbf{k}} c^*_{\mathbf{k}} c_{\mathbf{k}} \tag{2.26}$$

represents the linear spin-wave dynamics. It looks identical to the Hamiltonian of a system of non-interacting bosons, written in diagonal form. All higher-order processes, such as three-wave or four-wave interactions, are contained in the interaction Hamiltonian,

$$\mathcal{U}_{\mathrm{int}} = \mathcal{U}^{(3)} + \mathcal{U}^{(4)} + \dots \tag{2.27}$$

The dynamics of the different $\mathbf{k}$-modes can then by obtained by the corresponding canonical equations,

$$\frac{\mathrm{d}c_{\mathbf{k}}(t)}{\mathrm{d}t} = -i\frac{\partial\mathcal{U}}{\partial c^*_{\mathbf{k}}(t)} \quad \text{and} \quad \frac{\mathrm{d}c^*_{\mathbf{k}}(t)}{\mathrm{d}t} = i\frac{\partial\mathcal{U}}{\partial c_{\mathbf{k}}(t)}. \tag{2.28}$$

These canonical equations (or rate equations) for the spin-wave amplitudes $c_{\mathbf{k}}(t)$ and $c^*_{\mathbf{k}}(t)$ take the role of the equation of motion for the magnetization $\mathbf{M}(\mathbf{r}, t)$. In accordance to the quantum mechanical description of many-particle systems by creation and annihilation operators ($\hat{c}^\dagger_{\mathbf{k}}(t)$ and $\hat{c}_{\mathbf{k}}(t)$, respectively), different orders of magnon interactions, such as three-magnon or four-magnon scattering, can be efficiently described.

Such a classical Hamiltonian approach for spin waves was first introduced by Schlömann in 1959 [41, 42] and has since then become one of the standard tools to describe weakly nonlinear spin-wave dynamics as well as fluid dynamics [43–45] or plasma physics [46, 47], to begin with. It has been formulated in numerous reviews [48–50], books [4, 25], and more recently by Krivosik and Patton [39]. It played an important role in this thesis to derive rate equations for the nonlinear interaction of spin waves in a magnetic vortex. As the formalism is presented in great detail in the aforementioned literature, only a short derivation of the spin-wave Hamiltonian will be presented here.

Derivation of the Hamiltonian

Recall, that in a non-dissipative system (that is, without Gilbert damning), the effective magnetic field is connected to the total magnetic energy $\mathcal{H}$ by the variational derivative

$$\mathbf{B}_{\text{eff}} = -\frac{\delta \mathcal{H}}{\delta \mathbf{M}} \tag{2.29}$$

In principle, this $\mathcal{H}$ (later expressed in canonical variables) can be taken as the spin-wave Hamiltonian. However, following the convention in [39], it proves more apparent to convert the magnetic energy to frequency units

$$\mathcal{U} = \frac{\gamma \mathcal{H}}{M_s V}, \tag{2.30}$$

with again the modulus of the gyromagnetic ratio γ and the saturation magnetization of the sample M_s. Then, the complex spin-wave amplitudes $c_{\mathbf{k}}(t)$, $c^*_{\mathbf{k}}(t)$ will later be dimensionless. After the conversion, one proceeds with the following steps:

Step 0. This step is only necessary, if the equilibrium magnetization $\mathbf{M}_{\text{eq}}(\mathbf{r})$ is not collinear. In this case, the local components of the total magnetization M_x, M_y, M_z in the lab system must first be expressed in the spatially dependent coordinate system of $\mathbf{M}_{\text{eq}}(\mathbf{r})$ as M_1, M_2 (orthogonal to $\mathbf{M}_{\text{eq}}$) and M_3 (parallel to $\mathbf{M}_{\text{eq}}$). Of course, for samples with inhomogeneous magnetic textures such as vortices or domain walls, this step is important.

Step 1. The total magnetization is then expressed in the canonical variables $a(\mathbf{r}, t)$ and $a^*(\mathbf{r}, t)$ using the Schlömann transformation

$$\begin{aligned} \frac{iM_1 + M_2}{M_s} &= a(\mathbf{r}, t)\sqrt{2 - a^*(\mathbf{r}, t)a(\mathbf{r}, t)} \\ &\approx \sqrt{2}a(\mathbf{r}, t)\left(1 - \frac{1}{4}a^*(\mathbf{r}, t)a(\mathbf{r}, t)\right) \\ \frac{M_3}{M_s} &= 1 - a^*(\mathbf{r}, t)a(\mathbf{r}, t). \end{aligned} \tag{2.31}$$

This corresponds to a classical version of the well-known Holstein-Primakoff transformation [51], where the total operator $\hat{\mathbf{S}}$ is expressed in bosonic creation and annihilation operators $\hat{a}$ and $\hat{a}^\dagger$. Each created magnon then reduces the total spin by one $\hbar$. The latter approach can be used to derive magnons in the quantum mechanical Heisenberg model.

Step 3. Now, the canonical variables are expanded into the eigenmodes of the magnetic system. For example, in an unbound ferromagnet, this expansion is simply a Fourier transformation,

$$a(\mathbf{r}, t) = \sum_{\mathbf{k}} c_{\mathbf{k}}(t) e^{i\mathbf{k}\cdot\mathbf{r}}. \tag{2.32}$$

In more complex magnetic textures, the spin-wave normal modes will not be plane waves anymore and their spatial profile $e^{i\mathbf{k}\cdot\mathbf{r}}$ can be different. However, the spatial information of the modes will *disappear* in the integration over the sample volume.[7]

---

[7] Recall, that for example $\mathcal{H}_Z = -\int_V \mathrm{d}V\, \mathbf{M}(\mathbf{r}, t) \cdot \mathbf{B}_{\text{ext}}(\mathbf{r}, t)$.

This information will be contained in the coefficients of the Hamiltonian. Only the time-dependence will remain.

Step 4. At this point, the different terms can be collected and ordered by their appearance of the spin-wave amplitude (i.e. $\mathcal{U}^{(3)}$ will contain only terms containing products of three amplitudes, etc.). If the two-magnon term $\mathcal{U}^{(2)}$ is not diagonal which means that terms such as $c_{\mathbf{k}}c_{-\mathbf{k}}$ or $c^*_{\mathbf{k}}c^*_{-\mathbf{k}}$ appear in it, a Bogoliubov transformation is required to switch to the circularly polarized modes

$$d_{\mathbf{k}}(t) = u_{\mathbf{k}}c_{\mathbf{k}}(t) + v_{\mathbf{k}}c_{-\mathbf{k}}(t) \tag{2.33}$$

with appropriate $u_{\mathbf{k}}$ and $v_{\mathbf{k}}$ [39]. This step is important, if the eigenmodes $c_{\mathbf{k}}(t)$ are elliptically polarized.

Step 5. In certain regions of the spectrum $\omega(\mathbf{k})$, three-magnon scattering might not be allowed in terms of conservation of momentum and energy, meaning that $\mathcal{U}^{(3)} = 0$ for the corresponding modes. However, these non-resonant terms can still account significantly in the four-magnon scattering processes $\mathcal{U}^{(4)}$ as initially described by Zakharov [52].

Both the fourth and the fifth step are quantitatively important in certain situations, but they will go well beyond the scope of this thesis and will therefore not be carried out as for most situations, we will start at the finished Hamiltonian which takes the form

$$\begin{aligned}
\mathcal{U}^{(2)} &= \sum_{\mathbf{k}} \omega_{\mathbf{k}} c^*_{\mathbf{k}} c_{\mathbf{k}} \\
\mathcal{U}^{(3)} &= \frac{1}{2}\sum_{\mathbf{0,12}} [V_{\mathbf{0,12}} c^*_{\mathbf{0}} c_{\mathbf{1}} c_{\mathbf{2}} + \text{c.c.}]\delta(\mathbf{0}-\mathbf{1}-\mathbf{2}) \\
&\quad + \frac{1}{6}\sum_{\mathbf{123}} [U_{\mathbf{123}} c_{\mathbf{1}} c_{\mathbf{2}} c_{\mathbf{3}} + \text{c.c.}]\delta(\mathbf{1}+\mathbf{2}+\mathbf{3}) \\
\mathcal{U}^{(4)} &= \frac{1}{2}\sum_{\mathbf{12,34}} W_{\mathbf{12,34}} c^*_{\mathbf{1}} c^*_{\mathbf{2}} c_{\mathbf{3}} c_{\mathbf{4}} + \dots
\end{aligned} \tag{2.34}$$

Here, the short form $\mathbf{0} = \mathbf{k}_0$ (and so forth) is used for the sake of brevity. The first sum in the three-magnon Hamiltonian $\mathcal{U}^{(3)}$ describes the decay of one magnon into two other magnons $\mathbf{0} \to (\mathbf{1},\mathbf{2})$ with the scattering amplitude $V_{\mathbf{0,12}}$ (in units of angular frequency) as well as the inverse processes indicated by the complex conjugate term "+c.c.". The second sum describes the creation of three magnons from the vacuum $\varnothing \to (\mathbf{1},\mathbf{2},\mathbf{3})$ and vice versa. Usually these terms are only nonzero in active media [4]. The δ-functions assure the conservation of momentum. The terms in $\mathcal{U}^{(4)}$ describe four-magnon processes in which two existing magnons scatter into two new magnons.

The classical Hamiltonian formalism presented here has the advantage that it is expressed in linear spin-wave modes. All the linear information is encoded in the dispersion law $\omega(\mathbf{k})$ and the spatial profiles of the normal modes. Both can be obtained for example by the linearized LLG equation. All the coupling coefficients of higher-order processes (i.e. $V_{\mathbf{0,12}}$ or $W_{\mathbf{12,34}}$) are then derived from the mode profiles together with the corresponding interactions at hand (dipolar interaction, exchange and so forth). Albeit being only of an algebraic nature, this procedure can be very cumbersome for four-magnon scattering and higher orders (e. g. see the expression of the full $W_{\mathbf{12,34}}$ for unbound media in [39]). But at some points, useful approximations can be made. The reader is advised to not confuse the symbol $V_{\mathbf{0,12}}$ with V (for constant volume). The author has chosen to follow this overloaded naming convention, because unfortunately both notations are common in the theory of nonlinear spin-wave interactions [4, 25, 39, 40, 53].

Spin-wave occupation numbers & relation to second quantization

In repeated analogy with quantum mechanics, we call $N_{\mathbf{k}} = c^*_{\mathbf{k}} c_{\mathbf{k}} = |c_{\mathbf{k}}|^2$ the *spin-wave occupation number* or *spin-wave number* with wave vector $\mathbf{k}$. The analogy between both formalisms is presented for the exemplary case of $\mathbf{k} = 0$ in Fig. 2.7. Taken, that there is no interference between different waves, the spin-wave occupation number is the real quantity, which can be directly compared to experimental data found e.g. by means of Brillouin light-scattering spectroscopy (BLS) as it is directly proportional to the average measured photon counts in such an experiment – we will cover the details for this briefly in the next chapter.

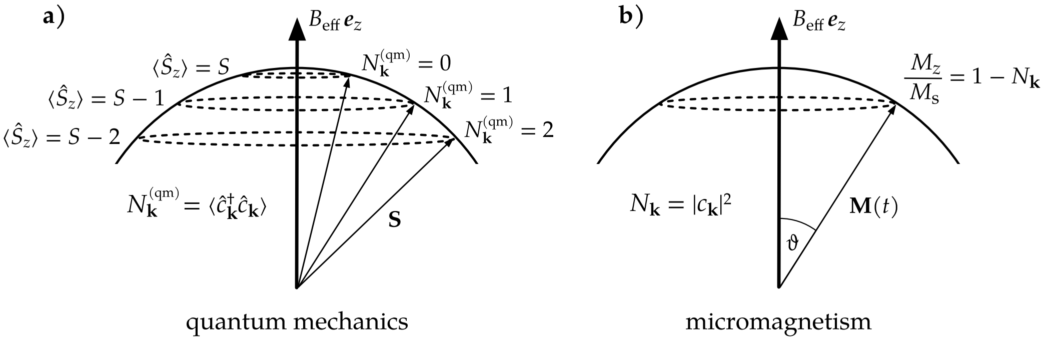
a)
$B_{\text{eff}}\,\boldsymbol{e}_z$
$\langle \hat{S}_z \rangle = S$
$\langle \hat{S}_z \rangle = S - 1$
$\langle \hat{S}_z \rangle = S - 2$
$N^{(\text{qm})}_{\mathbf{k}} = 0$
$N^{(\text{qm})}_{\mathbf{k}} = 1$
$N^{(\text{qm})}_{\mathbf{k}} = 2$
$N^{(\text{qm})}_{\mathbf{k}} = \langle \hat{c}^\dagger_{\mathbf{k}} \hat{c}_{\mathbf{k}} \rangle$
$\mathbf{S}$
quantum mechanics
b)
$B_{\text{eff}}\,\boldsymbol{e}_z$
$\frac{M_z}{M_s} = 1 - N_{\mathbf{k}}$
$N_{\mathbf{k}} = |c_{\mathbf{k}}|^2$
ϑ
$\mathbf{M}(t)$
micromagnetism

FIGURE 2.7: Schematic comparison of the roles of **a)** the quantum mechanical annihilation and creation operators $c_{\mathbf{k}}$ and $c^\dagger_{\mathbf{k}}$ which reduce the z-component of the total spin $\mathbf{S}$, as well as the magnon particle number $N^{(\text{qm})}_{\mathbf{k}}$ (here, $\hbar = 1$) against **b)** the micromagnetic spin-wave amplitudes $c_{\mathbf{k}}$ and $c^*_{\mathbf{k}}$ as well as the occupation number $N_{\mathbf{k}}$ within the classical Hamiltonian formalism. For simplicity, the magnet is assumed to be saturated in z-direction and the only mode which is populated is $\mathbf{k} = 0$.

In some publications [17, 54–57], especially in the theory of auto-oscillations, the modulus square of a complex mode amplitude $|c|^2$ is also called the dimensionless *oscillator power* p. However, in order to not confuse this quantity with the power of the external excitation field on the one hand and to avail ourselves of the quasi-particle vocabulary on the other hand, the above-mentioned terminology will be used in this thesis, although $N_{\mathbf{k}}$ hardly takes the values of natural numbers. This is because we have rescaled the Hamiltonian in micromagnetic units. We could have also boldly rescaled it with the reduced Planck constant $\hbar$ if we were to convert the total magnetic energy to units of angular frequency. Following this argument, the here-introduced micromagnetic spin-wave occupation number $N_{\mathbf{k}}$ can be related to the expectation value of the quantum mechanical particle number operator $N^{(\text{qm})}_{\mathbf{k}} = \langle \hat{c}^\dagger_{\mathbf{k}} \hat{c}_{\mathbf{k}} \rangle$ by

$$N^{(\text{qm})}_{\mathbf{k}} \approx \frac{M_s V}{\gamma \hbar} N_{\mathbf{k}} \quad \text{if} \quad N^{(\text{qm})}_{\mathbf{k}} \gg 1. \tag{2.35}$$

Within the rate equation calculations in the nonlinear regime performed later, the micromagnetic spin-wave numbers will be in order of $N_{\mathbf{k}} \sim 10^{-4}$, which – for the micrometer-sized permalloy disks addressed in this thesis – corresponds to a quantum mechanical number of magnons of about $N_{\mathbf{k}}^{(\mathrm{qm})} \sim 10^{6}$. This, in return, justifies the use of a classical theory to describe magnetization dynamics.[8]

---

[8] To be precise, even in the classical case, we would have to define $N_{\mathbf{k}} = \langle |c_{\mathbf{k}}|^2 \rangle$ as an average over chaotic wave phases (see e.g. [4]). However, during this thesis, we assume a coherent excitation of the modes taking part.

Chapter 3

Overview of methods

For this thesis, a mixture of experiments, simulation and theory was utilized to study the nonlinear dynamics in magnetic vortices. On the experimental side, results of Brillouin light-scattering microscopy (µBLS) experiments [12] conducted prior to this thesis by Franziska Wehrmann [22], Kai Wagner, Katrin Schultheiß [20, 58] and Tobias Hula [23] (among others) as well as experiments conducted during this thesis (mostly by Katrin Schultheiß, with the humble involvement of the author) are used to compare with the results of this thesis. Micromagnetic simulations were conducted using a custom version of MuMax^3 [59, 60], a micromagnetic solver which is widely used to study magnetization dynamics. In order to predict the temporal evolution of nonlinear interactions at hand, a theoretical model consisting of rate equations for the spin-wave modes in a magnetic vortex was developed using the classical Hamiltonian formalism for nonlinear spin-wave dynamics [39].

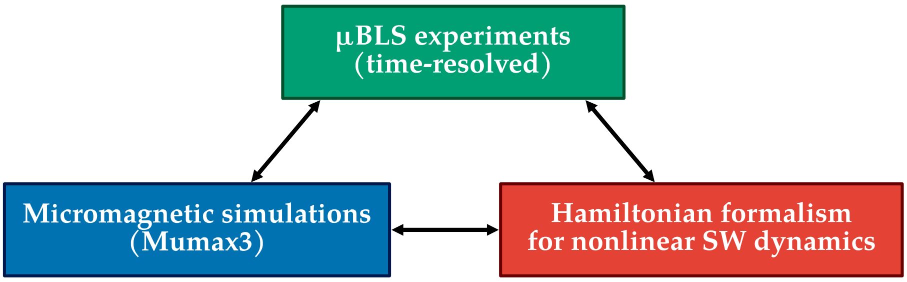

All methods presented here motivated and stimulated each other. Although the present work is more of numerical as well as theoretical nature, it also produced results which motivated and/or were confirmed later in experiments (with involvement of the author). In the following, an overview of the experimental, numerical and theoretical techniques will be given. The specific details will be explained when needed in the corresponding sections.

3.1 Micro-focused Brillouin light-scattering spectroscopy

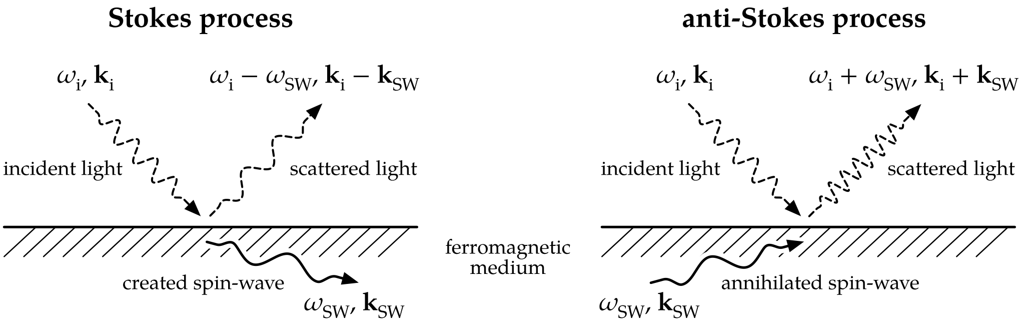
Stokes process
$\omega_i, \mathbf{k}_i$
$\omega_i - \omega_{SW}, \mathbf{k}_i - \mathbf{k}_{SW}$
incident light
scattered light
created spin-wave
$\omega_{SW}, \mathbf{k}_{SW}$
ferromagnetic medium
anti-Stokes process
$\omega_i, \mathbf{k}_i$
$\omega_i + \omega_{SW}, \mathbf{k}_i + \mathbf{k}_{SW}$
incident light
scattered light
annihilated spin-wave
$\omega_{SW}, \mathbf{k}_{SW}$

FIGURE 3.1: Schematics of the creation (Stokes) and annihilation (anti-Stokes) of a spin wave using monochromatic light which is scattered at a ferromagnetic medium.

The experiments presented in this thesis rely on the inelastic scattering of monochromatic light at ferromagnetic materials, commonly referred to as BLS [61, 62]. When an incident photon with frequency ω_i and wave vector $\mathbf{k}_\mathrm{i}$ is scattered at the surface of a ferromagnetic medium,[1] it may either create (Stokes process) or annihilate (anti-Stokes process) a spin-wave (see Fig. 3.1). The difference in frequency and wave vector of the scattered photon $(\mathbf{k}_\mathrm{s}, \omega_\mathrm{s})$ to the incident light is equal to that of the spin wave ($\mathbf{k}_\mathrm{SW}$ and ω_SW).

$$\begin{aligned}\omega_\mathrm{s} &= \omega_\mathrm{i} \pm \omega_\mathrm{SW} \\ \mathbf{k}_\mathrm{s} &= \mathbf{k}_\mathrm{i} \pm \mathbf{k}_\mathrm{SW}\end{aligned} \tag{3.1}$$

The frequency of the scattered light – and with it the frequency of the spin wave – is measured using a Tandem-Fabry-Pérot interferometer [63], with the frequency of the incident light ω_i serving as a reference signal. The incoming photons are detected using a photo detector. In the resulting frequency spectrum, one can see both the Stokes as well as the anti-Stokes signal as photon counts at that particular frequency (see Fig. 3.2).

In a *conventional* (or wave-vector selective) BLS measurement performed on thin magnetic films, the in-plane component of the spin-wave wave vector can be obtained from conservation of momentum by choosing the incident angle of the light accordingly. However, in the µBLS experiments relevant for this thesis the wave-vector resolution is exchanged for a spatial resolution by focusing the beam of the incident light down to a 300 nm spot size (without a well-defined incident angle).

Spin waves in magnetic nanostructures can be excited using a patterned microwave antenna, connected to an external microwave source, which generates a magnetic RF field at the site of the sample. In our case the antenna is an Ω-shaped current loop [20] around the vortex disk. In order to allow for a time-resolved measurement up to 50 ps precision, this external RF field is applied in a stroboscopic fashion, synchronized with the photo detector. The detected photons can then be related to scattering events on the disk using a time-of-flight technique.

The author would like to point out again, that although experimental results are shown, the present thesis does not have its focus on the experimental realization

---

[1] Strictly speaking, the photon is diffracted by the periodic change in the optical properties of the ferromagnet, caused by the spin wave and magneto-optical effects.

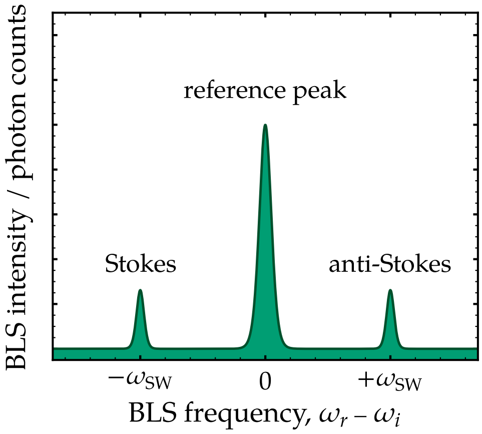

FIGURE 3.2: Schematic frequency spectrum of a BLS experiment, with spin waves at frequency ω_{SW}.

and results of that nature, which are not already published, will be elsewhere in the future. For a detailed description of the µBLS system used to produce the presented experimental data (regarding optics, software, etc.) the reader is kindly directed to the experimental works described in [20, 22, 23] as well as to the review on µBLS by Sebastian et al. [12].

3.2 Micromagnetic simulations

Micromagnetic simulations are often used in the field of magnetization dynamics to help explain experimental observations or to predict new experimental designs. They rely on solving the equation of motion of the magnetization $\mathbf{M}(\mathbf{r}, t)$, namely the LLG equation of motion from Sec. 2.2 on a discrete grid. Essentially, micromagnetic simulations allow to conduct virtual experiments in an idealized system in which all interactions and material parameters are known and the magnetization can be probed with an arbitrary high spatio-temporal precision. All further dynamic properties such as spectra, mode profiles, dispersions, damping rates, etc. are – like in most real experiment – acquired in post-processing.

For this thesis, a custom version of the popular GPU-accelerated micromagnetic solver MuMax^3 [59, 60] was used which solves the LLG equation on a rectangular grid using a Runge-Kutta Dormand-Prince method [64]. To allow for such a numerical integration, the torque equation is evaluated in its explicit form

$$\frac{\partial \mathbf{M}}{\partial t} = -\frac{\gamma}{1+\alpha_G^2}[\mathbf{M} \times \mathbf{B}_{\mathrm{eff}}] - \frac{\gamma \alpha_G}{(1+\alpha_G^2) M_s} \mathbf{M} \times [\mathbf{M} \times \mathbf{B}_{\mathrm{eff}}], \tag{3.2}$$

which can be obtained by left-crossing $\mathbf{M}$ into Eq. 2.15. At each step in time, the effective field $\mathbf{B}_{\mathrm{eff}}$ is calculated and the magnetization is subsequently integrated forward in time. The resulting time-dependent magnetization at each grid point, $\mathbf{M}(\mathbf{r}, t)$, as well as other figures of merit, such as the total magnetic energy or external field amplitudes, can be sampled at a given time step and stored for post-processing. Magnetic oscillations such as spin-wave modes are usually retrieved from micromagnetic simulation by employing a fast Fourier transform (FFT) at each grid point.

3.3 Classical Hamiltonian formalism

The classical Hamiltonian formalism outlined in 2.3.3 has been utilized to derive rate equations for the complex spin-wave amplitudes $c^*_{\mathbf{k}}(t)$ and $c_{\mathbf{k}}(t)$, which are again classical analoga to the quantum mechanical Bose creation and annihilation operators. With such rate equations, the nonlinear interaction of the spin waves that take part in a scattering event can be described on a mode level. The derivation of these equations for the three-magnon scattering in magnetic vortices was a major part of this thesis and will be described in detail in Chap. 7.

Chapter 4

Mapping of the mode spectrum

As the excitations in a vortex have been examined in experiments [20, 40, 65], theory [40, 66–73], as well as simulations [20, 74–76] in countless works, there exists a good understanding of these modes. Much like the magnonic excitations in infinitely extended thin films, the spin waves in a vortex disk will be characterized by their wave vector. However, the spin-wave manifold for thin films was continuous in the direction of propagation. Even in narrow waveguides, where there is an additional quantization along the width of the waveguide, continuous sets of modes can be found. This will not be the case anymore for magnetic nanodisks in the vortex state. Here, we have dominant boundary conditions in every direction resulting in a completely discrete set of modes. This chapter will deal with the mapping of this set. First from a conceptual view and then via micromagnetic simulations. A knowledge of the dispersion law $\omega(\mathbf{k})$ will be essential for understanding the linear as well as the nonlinear phenomena discussed later.

4.1 Initial considerations

The equilibrium magnetization in a vortex state is obviously not collinear. The orientation of the magnetization vector is a very *local* quantity. However, waves are *global* in that sense. In order to effectively describe the dynamics of the time dependent magnetization $\mathbf{M}(t) = \mathbf{M}_{\text{eq}} + \mathbf{m}(t)$, one must first transform from the lab system, expressed in cylindrical coordinates (M_ϱ, M_ϕ, M_z), to the local reference frame, that consists of two components M_1 and M_2 perpendicular and one component M_3 parallel to the equilibrium. The two types of reference frame are illustrated in Fig. 4.1a,b. The analytic details for this transformation can be found in Appx. A.2. In the linear approximation ($M_3 = \text{const.}$) we can decompose the dynamics into normal modes via

$$\frac{iM_1 + M_2}{M_s} = \sum_{\mathbf{k}} c_{\mathbf{k}}(t)\Psi_{\mathbf{k}}(\varrho)\Phi_{\mathbf{k}}(\phi) \tag{4.1}$$

with the time-dependent spin-wave amplitudes $c_{\mathbf{k}}(t)$, the radial profiles $\Psi_{\mathbf{k}}(\varrho)$ and the azimuthal profiles $\Phi_{\mathbf{k}}(\phi)$. The wave vector $\mathbf{k}$ needs yet to be defined at this point. As we consider a thin magnetic disk, the magnetization can be viewed as translational invariant along the thickness direction (z). This is substantiated by the fact that higher order modes, such as perpendicular-standing spin waves are much higher in frequency for thin magnetic elements (see again Fig. 2.4b). Thus, the canonical wave vector can be seen as the two-dimensional quantity $\mathbf{k} = (k_\varrho, k_\phi)$ with a component in ϱ-direction and an angular-momentum-like component in ϕ-direction (see Fig. 2.4c for an illustration). The possible values for canonical wave vector components are set by the boundary conditions in each coordinate together with the linearized LLG. The azimuthal part must obey a periodic boundary condition in ϕ

and – for pinned spins at the edge – the radial part must vanish at the edge of the disk.[1] As a consequence, only a discrete set of spin-wave modes is allowed, counted by $n \in \mathbb{N}$ in the radial and $m \in \mathbb{Z}$ in the azimuthal direction. The mode profiles (for $m > 1$) can be approximated as

$$\Phi_{\mathbf{k}}(\phi) \equiv \Phi_m(\phi) = e^{im\phi} \tag{4.2}$$

$$\Psi_{\mathbf{k}}(\varrho) \equiv \Psi_n(\varrho) = \kappa_n J_1(k_n \rho) \tag{4.3}$$

with the azimuthal part following from the cylindrical symmetry. The radial part is constituted by the first-order Bessel function J_1 and some unimportant normalization constant κ_n. The possible effective radial wave vectors k_n are obtained using the above-mentioned boundary conditions. The expression for Ψ_n was found by Buess et al. [77], but unfortunately, is only a good approximation in the dipolar regime (for small wave vectors). With the exception of $m = \pm 1$, the modes for $\pm m$ share approximately the same radial profile. The former anomaly stems also from the interaction with the vortex core [66, 67, 78–80]. In Fig. 4.2, we see exemplary mode profiles for the first five radial modes of $m = \pm 8$, calculated by means of micromagnetic simulations. The details are discussed in the next sections.

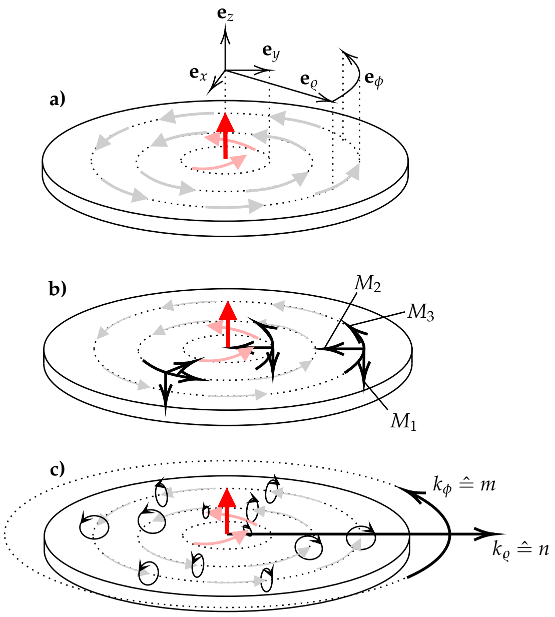

FIGURE 4.1: Schematics of a magnetic nanodisk in the vortex state showing **a)** the equilibrium magnetization. The color code illustrates the out-of-plane component $M_{\mathrm{eq},z}$ from zero (gray) to maximum value (red). The unit vectors are not true to scale. **b)** shows examples for the spatially dependent local coordinate system which is useful for describing the dynamics such as the magnon modes which are characterized **c)** by their canonical radial wave vector k_ϱ and their azimuthal wave vector k_ϕ (or mode index n and m, respectively).

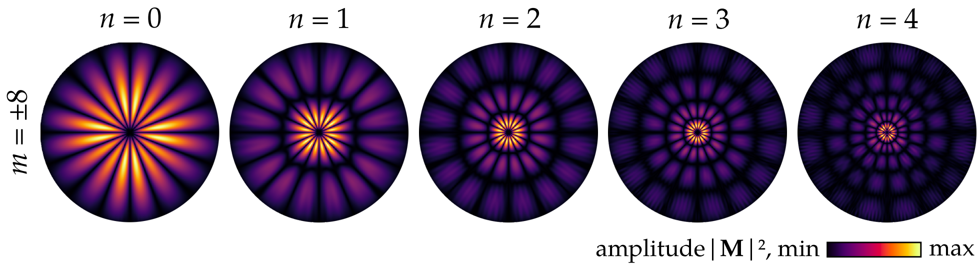

FIGURE 4.2: Intensity plots (squared mode amplitudes) for the first five radial modes with an azimuthal index $m = \pm 8$. The profiles were obtained for a permalloy disk with 5.1 µm diameter using micromagnetic simulations. All material parameters is found in Tab. 4.1.

---

[1] To be precise, that radial part must also satisfy $\Psi'_{nm}(0) = 0$.

4.2 Calculation of vortex state

To obtain the spin-wave modes in a disk using micromagnetic simulations, one must first calculate the equilibrium magnetization $\mathbf{M}_{\mathrm{eq}}$. In MuMax^3, this was done by modeling different permalloy disks of 50 nm thickness and various radii on a rectangular grid of 512×512×1 cells. The material parameters are summarized in Tab. 4.1. For most simulations in this thesis, a disk of 5.1 µm diameter was used. This choice was made in order to achieve a comparison with measurements based on real samples with the same dimensions and material parameters.

Material parameters	
exchange stiffness, A_{ex}	13 pJ/m
saturation, M_s	810 kA/m
reduced gyromagnetic ratio, $\gamma/2\pi$	29.6 GHz/T
Gilbert damping, α_G	0.008
thickness, L	50 nm
diameter, $2R$	1 µm, 2 µm, 5.1 µm
Mesh parameters	
mumber of cells (x, y, z)	512×512×1
cell size over thickness (z)	50 nm
lateral cell size (x, y)	1.95 nm, 3.90 nm, 9.96 nm

TABLE 4.1: Material and mesh parameters for the permalloy disks used in the simulations.

At this point a crucial reason for the nature of these simulations has to be made. In principle, if one had the task to perform micromagnetic simulations on a (rigid) vortex, one would initially not turn to a finite-difference approach (rectangular grid), like the approach used in this thesis, but instead rather use a finite-element approach. Software solutions include TetraMag [81], magpar [82], NMag [83], and FinMag [84], among others. These solutions model the magnetization using polygons, such as tetraheders, which in this case would allow for a finer modeling both of the vortex core as well as of the edge of the disk. However, using a finite-difference approach provides the striking advantage of making the computation of the dipolar field much faster. On a polygonial grid, the demagnetizing field has to be calculated by solving the Poisson equation of the magnetostatic potential. So, for each cell and for each time step, one has to integrate over the whole sample. This can be taken care of much faster on a rectangular grid, for which the calculation of the dipolar field can be simplified to a FFT [59]. If one is to perform studies on nonlinear behavior or carry out simulations covering a wide parameter space, a large number of simulations has to be made. This is simply not possible in a reasonable amount of time using a polygonial grid. The point of simulation time together with the economical reason of not producing unnecessary large amounts of data has led to the decision to limit the mesh size for the disks to 512×512×1 cells. For the largest disk size, this leads to a lateral cell size of approximately 10 nm (see again Tab. 4.1). This is larger than the exchange length in permalloy which is about 5 nm. However, we will see, that in the dipolar spin-wave regime and even at the beginning of the exchange reqime, this will not be of a great concern as there will be a very good agreement with results obtained from other techniques such as semi-analytics or BLS experiments. To make the numerics consistent over the whole thesis, the same mesh is used for all simulations for which th same disk is of concern. The disadvantage of having not as precise numerics is overcompensated by having the possibility to perform a very large number of simulations.

To calculate the equilibrium magnetization, a template vortex with given chirality and polarity can be initialized in MuMax^3 at the center of the disk. From this starting point, the magnetic system is then allowed to relax into its equilibrium. In general, for this purpose the built-in `relax()` method may be used. However, in some cases, as well as in this one, this method does not find the right equilibrium and it proves more sufficient to relax *manually* by setting the Gilbert damping to $\alpha_G = 0.5$ and letting the magnetization evolve for a period of 20 ns.

Finally, modes in the system are excited by applying an external magnetic RF field. In particular, a homogeneous out-of-plane (OOP) field is used. For example, an OOP field exciting such a disk can be set up by patterning an Ω-shaped antenna around it [20]. In Fig. 4.3, we see the schematics of the mesh housing the equilibrium magnetization $\mathbf{M}_{\text{eq}}$ in the vortex state together with the orientation of the external RF field $\mathbf{b}_{\text{ext}}(t)$. The excitation field can either be pulsed to contain a broad frequency spectrum or it can be a continuous-wave (CW) excitation with a fixed frequency.

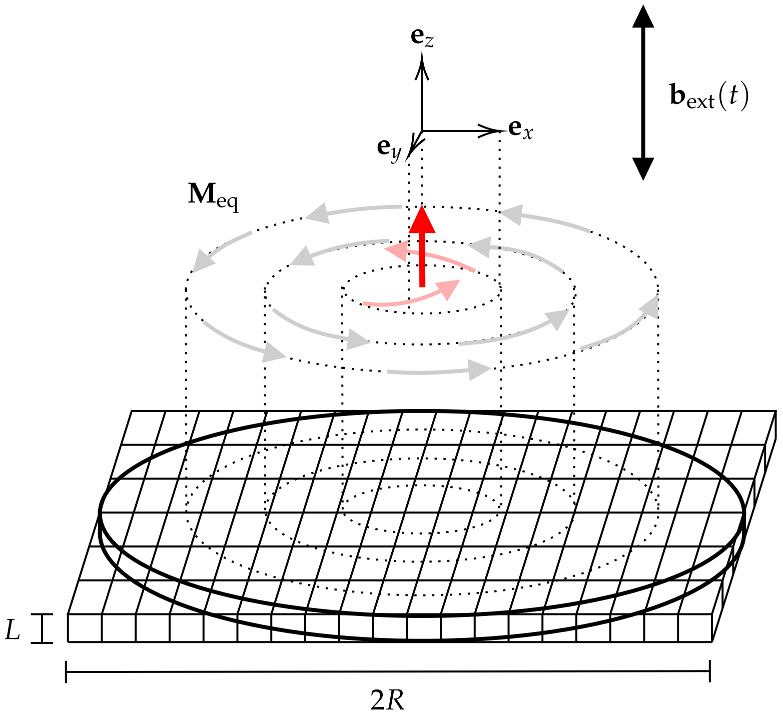

FIGURE 4.3: Schematics of the mesh used to simulate the vortex disks. The cells are not true to scale.

4.3 Calculation of the dispersion relation

The dispersion of the spin-wave modes in a vortex up to $|m| = 30$ was recently calculated semi-analytically by Dr. Roman Verba, a collaborator on this project from Kyiv , for a 5.1 µm diameter disk. For this, a projection method similar to the one presented in [77] was used with the difference that exchange was also included.

In an effort to be more flexible and being able to calculate the dispersion *in-house* for different parameters and higher azimuthal wave vectors, a method was developed to extract the dispersion by means of micromagnetic simulations. The result presented in this section will be shown to have very good agreement with the dispersion calculated by Dr. Verba.

Method Obtaining the dispersion relation of the spin-wave modes with micromagnetic simulations comes down to exciting these modes at the same time using an external field and then isolating them by means of FFT of the time dependent magnetization. One transformation is performed in the time domain to acquire the frequency response, and a transformation in the spatial domain is made to obtain the wave-vector response. This works for all the propagation directions in which the normal modes are propagating as plane waves proportional to $\exp(i\mathbf{kr})$ (e.g. in a infinitely extended thin film, this works for all in-plane directions or in a domain wall for the direction parallel to the wall).

In the case of a vortex, the situation is a little bit more complicated as it is not directly clear how to perform a FFT due to the geometry of the problem. And of course, the normal modes are not plane waves. Therefore, the approach will be a little different yet somehow similar. In order to calculate the dispersion for a vortex, OOP RF fields with a particular spatial symmetry have to be used. To excite azimuthal modes, one can use a field with the corresponding profile proportional to $\cos(m'\phi)$, with m' being a principal number and representing the azimuthal index of the field. Such a field can easily be implemented in micromagnetic simulations. Fig. 4.4 illustrates snapshots of the OOP component of such a field for different m'.

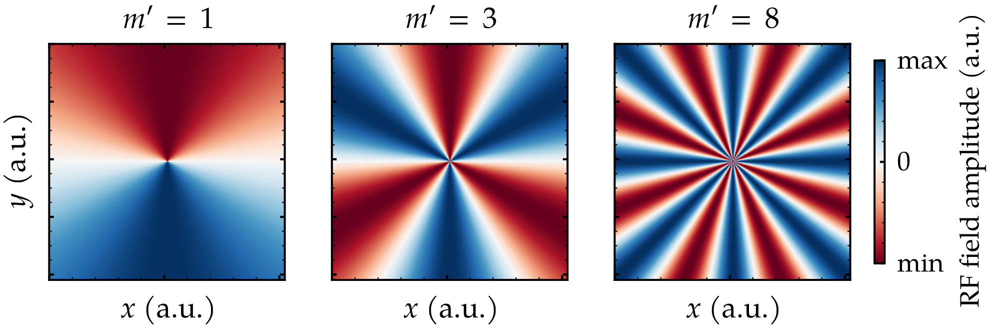

FIGURE 4.4: Spatial profiles of an out-of-plane RF field with a spatial dependence of $\cos(m'\phi)$ for different indeces m'.

In fact, a field with a particular m' can only couple to modes with the same or the negated azimuthal index $m = \pm m'$. This will be shown explicitly in Sec. 7.2 when deriving the rate equations for the spin-wave normal modes.

In order to excite all the duplets $(n, \pm m')$ for different radial indices n in one simulation, a pulsed OOP field proportional to $\operatorname{sinc}(\omega_{\max} t)$ is used to equally excite a wide range of frequencies. In summary, the field may be written as

$$\mathbf{b}_{\text{ext}}(\phi, t) = b_{\text{pulse}} \cdot \cos(m'\phi) \cdot \text{sinc}(\omega_{\max}(t - t_0)), \tag{4.4}$$

with the amplitude of the pulse $b_{\text{pulse}} = 1\,\text{mT}$, the cut-off frequency $\omega_{\max}/2\pi = 40\,\text{GHz}$ and a shift of the pulse with respect to zero $t_0 = 50\,\text{ps}$ to avoid a rapid switch on of the field. The system is allowed to evolve for 25 ns and the resulting time-dependent magnetization is sampled at 10 ps and then Fourier transformed into the frequency domain at each cell separately. The resulting amplitudes and phases are then spatially averaged yielding the power spectrum of the whole disk. To carry out these calculations, a program based on the work by Attila Kákay was used.

Last but not least, only to calculate, the dispersion, the damping was slightly tweaked. With a reduced Gilbert damping parameter $\alpha_G = 0.0007$ the line widths are much smaller allowing for a better peak extraction. This is justified as long as we are only interested in the linear resonance frequencies of the modes.

In Fig. 4.5, we see the power spectrum of the time-dependent magnetization when excited with a pulsed field of azimuthal index $m' = 8$. By performing a windowed backwards Fourier transform around the frequency of each peak, one obtains the mode profiles as well as the phases of these Fourier components.

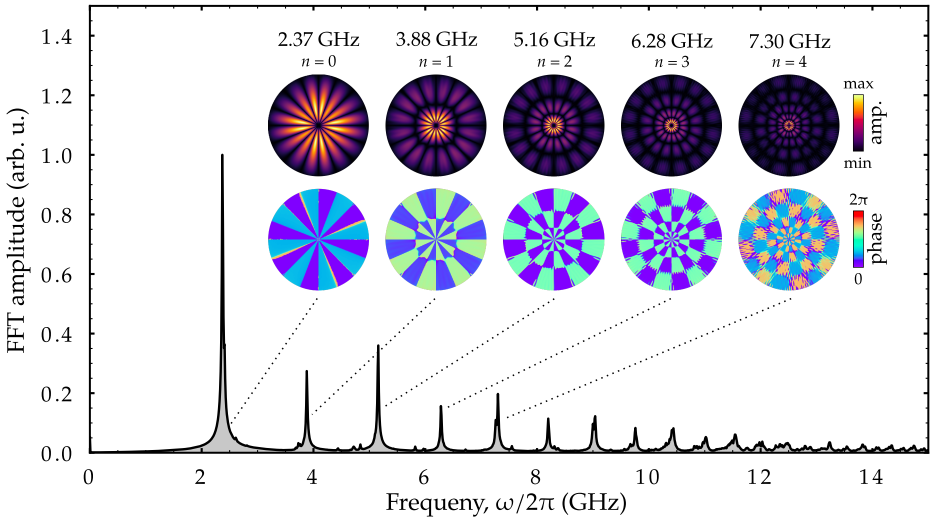

FIGURE 4.5: Spectrum of a permalloy disk with a diameter of 5.1 µm that is excited with a sinc-pulse in time and an azimuthal profile with $m' = 8$ in space. The insets show the amplitudes and phases of the first five duplets with $m = \pm 8$.

The mode profiles seen in Fig. 4.5 confirm that indeed each peak corresponds to one radial index. From the step-like behavior of the phases one can see that standing waves are excited. This, of course, are the respective duplet modes that are excited by the azimuthal field $m' = \pm m$.

Finally, to calculate the full dispersion one needs to redo this whole procedure for all desired azimuthal indices. Given the computational load, this is a rather time-consuming task. To reduce the overhead, the author wrote several scripts to automatize the generation of MuMax^3 problem definitions as well as calculating the power spectrum for a large number of simulations. As a result, the computation of a full dispersion takes about one day.

Results & discussion Exemplary dispersion relations calculated using the method described above are seen in Fig. 4.6 for 50 nm thick permalloy disks with 1 µm, 2 µm and 5.1 µm diameter. Each column of the heatmaps is the power spectrum of one pulsed simulation with the corresponding azimuthal field. For the 5.1 µm diameter disk shown in Fig. 4.6c, there is a very good agreement with the result calculated by Dr. Verba (drawn as red data points with lines to guide the eye).

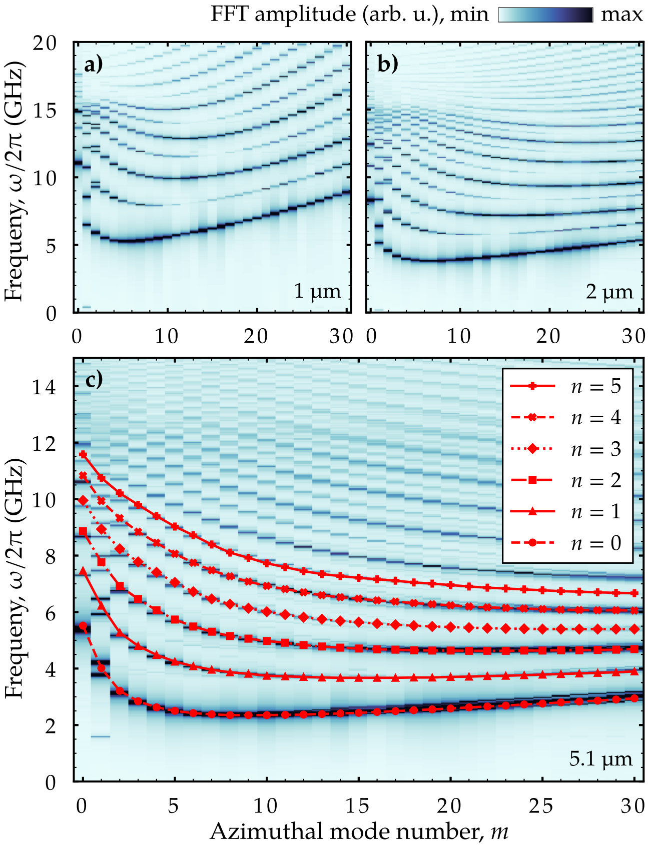

FIGURE 4.6: Dispersion relation of the vortex normal modes calculated by micromagnetic simulation (colormap) for a permalloy disk of 50 nm thickness and **a)** 1 µm, **b)** 2 µm and **c)** 5.1 µm diameter. The results in **c)** are compared as with a diagonalization approach (red points) for the first six radial indices. The dispersion shows a backward-volume character in azimuthal direction (varying m) and a surface-wave character in radial direction (varying n). Additionally, one can observe that the duplets for $m = \pm 1$ are split in frequency. With decreasing disk diameter, the dispersion becomes steeper (more quadratic) for the same $|m|$ and the band gap increases.

To begin with, several features reminiscent of the thin-film spin-wave dispersion are recovered. It can be seen that with increasing azimuthal mode number, the dispersion shows a backward-volume-like behavior. This is expected, as increasing $|m|$ means increasing the canonical wave vector k_ϕ in azimuthal direction, that is parallel to the equilibrium magnetization. For small m, this result was already found in [77], where modes with negative dispersion were observed in a vortex. In radial direction, of course increasing index n increases the canonical wave vector k_ρ that is perpendicular to the magnetization. As a consequence we observe an increase in frequency with each branch.

Overall, comparing different disk sizes, the mode frequencies go down for larger disks. However, looking closer, we see two trends. Of course, with increasing disk diameter the mean inter-branch distance becomes smaller similar to the convergence of the mode frequencies in any potential well with extending size.

At the same time, the minima of the dispersion branches shift towards higher $|m|$ for larger disk diameters. This is due to the fact that, for larger disks, the modes can save exchange energy at higher azimuthal wave vectors by shifting the intensity towards the perimeter of the disk. This mechanism leads to the appearance of whispering gallery magnons [20].

Another feature that can be observed in the dispersion is the splitting of the $m = \pm 1$ duplets. This splitting becomes larger for smaller disks and is due to hybridization with the gyrotropic mode [66, 67, 78–80]. It is only mentioned here for the sake of completeness.

Chapter 5

Prediction of the scattering channels

After we have mapped out the necessary linear information (mode profiles and dispersion) in the previous chapter, we are able to move forward by mapping the nonlinear dynamics. More specifically we want to study the possible resonant three-magnon-scattering channels. In anticipation of Chap. 9, a knowledge about these channels is essential in the design of technical applications.

As the three-magnon scattering in magnetic vortices obeys certain selection rules [20], not all combinations of spin-wave modes are allowed. Consequently, the set of possible scattering channels will have to obey a certain structure. The aim of the present chapter is to predict this set of possible three-magnon scattering channels.

In the first part of this chapter, we will see that one can obtain a surprising amount of clarity by only applying the selection rules of the three-magnon scattering to the dispersion $\omega(\mathbf{k})$; that is, in other words, search for the resonant scattering channels. In the second part, this search will be extended by taking into account the individual thresholds of the different channels, narrowing down the number of secondary spin-wave modes that will be observed for excitation powers slightly above the threshold. But before going into this effort, the reader deserves a brief explanation of the aforementioned selection rules.

5.0 Selection rules of three-magnon scattering in a magnetic vortex

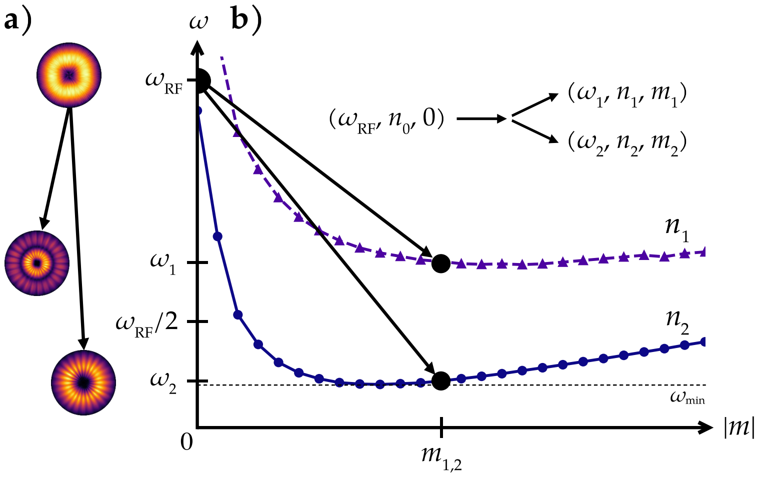

FIGURE 5.1: Schematics of the selection rules of three-magnon scattering in a magnetic vortex showing **a)** the mode profiles and **b)** the mode numbers and frequencies of an exemplary resonant scattering channel in context of the dispersion $\omega(\mathbf{k})$.

The three-magnon scattering process in a magnetic vortex which is of interest for this thesis is the decay of a radial mode $(n, 0)$ into two azimuthal modes (see Fig. 5.1). Focusing only on this class of three-wave processes is justified for the following reasons: First, when using a current-loop microwave antenna around the ferromagnetic disk, a spatially homogeneous RF field is produced, which can only couple to spin-wave modes with zero azimuthal periods, $m = 0$. As a consequence, only these radial modes can be pumped to achieve their threshold amplitude. Second, the dispersion $\omega(\mathbf{k})$ shows a characteristic backward-volume behavior in azimuthal direction, with a certain band gap ω_{min} (see Fig. 5.1b). Since the RF field directly excites a certain spin-wave mode with ω_{RF}, conservation of energy demands that the frequency of the directly excited mode ω_{RF} must be at least twice as large as the band gap, $\omega_{\mathrm{RF}} \geq 2\omega_{\mathrm{min}}$. With increasing excitation frequency, this condition is satisfied foremost for radial modes. Focusing now on the decay of a radial mode ω_{RF} into two other modes $\omega_{1,2}$, the selection rules are

(i) conservation of energy. Of course, all scattering processes must be close to resonance. Since we already know that the two secondary modes will have different frequencies, we can write this rule as

$$\omega_{1,2} \approx \omega_{\mathrm{RF}}/2 \pm \Delta\omega. \tag{5.1}$$

In a discrete spectrum like the one of a magnetic vortex, this condition can hardly be satisfied. In most cases, this resonance condition is only guaranteed within a certain line width, hence the "$\approx$". Later, this fact will lead to a renormalization of the threshold fields.

(ii) conservation of angular momentum. The equilibrium magnetization exhibits a rotational symmetry in azimuthal direction. As a consequence, the canonical angular momentum k_ϕ of a spin-wave, associated with the mode index m, is a conserved quantity, too. A radial mode has $k_\phi = 0$. Thus, the secondary modes must have opposite azimuthal indices,

$$m_{1,2} = \pm m. \tag{5.2}$$

(iii) dipolar coupling. This particular selection rule is what makes three-magnon scattering in a magnetic vortex quite exotic, as it leads to the a split in frequency of the secondary modes. It is a consequence of the symmetry of the dipolar interaction in such systems and was found in by Roman Verba using a qualitative evaluation of the three-magnon scattering efficiency $V_{\mathbf{0,12}}$ of the vortex modes within the classical Hamiltonian formalism [20]. He derived, that only the dipolar interaction contributes to the decay channels at hand. More specifically,

$$\begin{aligned} V^{\text{dip}}_{\mathbf{0,12}} = \frac{im\omega_M}{2\sqrt{2}R^2} \iiint (J_{m+1}(k\rho) - J_{m-1}(k\rho))J_m(k\rho\prime)\times \\ p(kL)\Psi_{\mathbf{0}}(\rho\prime)[\Psi_{\mathbf{1}}(\rho)\Psi_{\mathbf{2}}(\rho\prime) - \Psi_{\mathbf{2}}(\rho)\Psi_{\mathbf{1}}(\rho\prime)]\rho \,\mathrm{d}\rho \,\mathrm{d}\rho\prime \,\mathrm{d}k\,, \end{aligned} \tag{5.3}$$

with the demagnetizing factor for thin films $p(x) = 1 - (1 - e^{-|x|})/|x|$, thickness and radius of the vortex disk L and R, the Bessel functions of the first kind J_m and $\omega_M = \mu_0\gamma M_S$. It follows that the efficiency is only non-zero, if the radial mode profiles of the secondary modes $\Psi_{\mathbf{1}}$ and $\Psi_{\mathbf{2}}$ are distinct from each other (note the expression within the brackets). As the azimuthal mode numbers must be opposite and modes within one duplet $\pm m$ have the same radial profile (see again Sec. 4.1), the radial mode numbers of the secondary modes have to be different,

$$n_1 \neq n_2. \tag{5.4}$$

In other words, the secondary modes must come from different branches of the dispersion. There is no strict relation to the radial number of the directly excited mode. Unfortunately, the explanation for this selection rule remains in its exact form to be rather mathematical and without an intuitive picture. It appears, that sometimes physics is not simple and beautiful. If one was to look for a more *physically* sound but maybe inaccurate explanation, one could think of this selection rule as the following: The two secondary modes by themselves do not exhibit a magnetic moment ($m \neq 0$). However, together they can produce a magnetic moment to which the dipolar field of the directly excited mode ($m = 0$) can couple, but only if they have different mode profiles.

5.1 Finding the resonant channels

5.1.1 Algorithm

After having calculated the dispersion and having expressed the selection rules, the task of finding the possible three-magnon scattering channels is straightforward. For this purpose, a Python script was written which takes a given dispersion data set and outputs the channels in the following way:

(i) For each excitation frequency ω_{RF}, select all duplets $(n_2, |m_2|)$ which are below $\omega_{\text{ex}}/2$ in frequency. This yields a set of possible secondary modes, which are lower in frequency $\omega_2 = \omega_{\text{RF}}/2 - \Delta\omega_2$.[1]

---

[1] Here, the frequency split $\Delta\omega_2$ is also indexed, since, at this point, we do not know yet, whether this particular mode will contribute to a resonant channel.

(ii) For each of these duplets, find all partner duplets $(n_1, |m_1|)$ that have a *different* radial index n, but the *same* modulus of azimuthal index $|m|$. The result is a set of possible secondary modes which are higher in frequency $\omega_1 = \omega_{\mathrm{RF}}/2 + \Delta\omega_1$.

(iii) In the last step, only the combinations of modes are kept, which are close to resonance. The modes must satisfy

$$|\omega_{\mathrm{RF}}/2 + \Delta\omega - \omega_1| < \Omega \quad \text{with} \quad \Delta\omega = |\omega_{\mathrm{RF}}/2 - \omega_2|. \tag{5.5}$$

Here, the parameter Ω represents the word "close" as it defines how far a channel can be from resonance and still be allowed. It is reasonable to set this parameter to be equal to the smallest line width of the modes taking part in that channel, which is in this case Γ_2. Of course, condition 5.5 is equivalent to $|\Delta\omega_1 - \Delta\omega_2| < \Omega$.

This algorithm can now be applied to any magnon system with a discrete spectrum and structurally the same above-mentioned selection rules. For example, later we will compare the effects of different nanodisk dimension.

However, first of a all, the resonant three-magnon channels in a 5.1 µm diameter permalloy disk will be studied in more detail. For example, in Fig. 5.2a, we see the resonant three-magnon channels for an excitation frequency of 6.1 GHz, acquired by applying the algorithm to the respective dispersion from Sec. 4.3. In fact, these are the channels for the lowest possible excitation frequency, which can be predicted with this method. By sweeping the excitation frequency (seen in Fig. 5.2b), we find that below 6.1 GHz, there are no resonant channels. This frequency sweep exhibits a pattern which is already quite similar to the experimentally observed data obtained by means of µBLS in Fig. 5.2c.

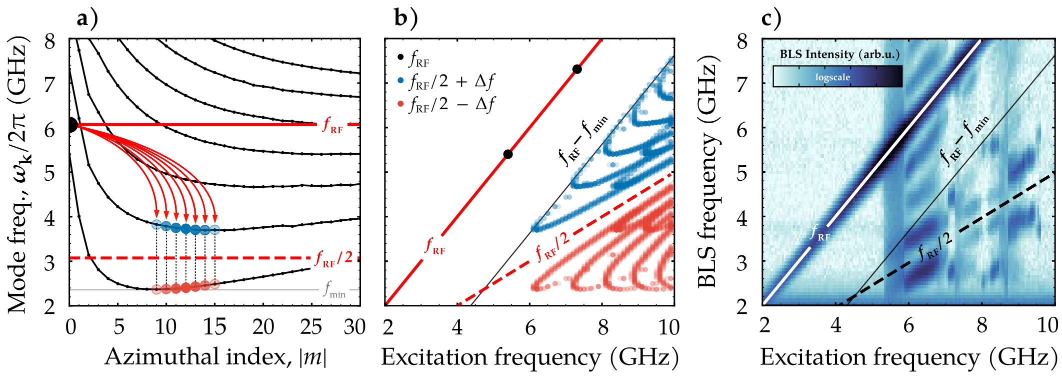

FIGURE 5.2: Result of the algorithm to find the resonant three-magnon channels for a 5.1 µm diameter disk, showing **a)** the channels for an excitation frequency of $f_{\mathrm{RF}} = 6.1\,\mathrm{GHz}$ overlayed on the dispersion as well as **b)** the full frequency sweep with all resonant channels in that range. Each mode (dot) is drawn less transparent the more resonant the respective channel is. **c)** shows the corresponding experimental data obtained with µBLS. Details on the experiments are found in [20].

5.1.2 Comparison with experiments

The first conclusion which can be drawn from the resonant channels is an observation that has already been anticipated in the motivation in Chap. 1, where only some of the modes in the experimental data have been identified to originate from three-magnon scattering with the directly excited mode. In Fig. 5.2b, we see that there can be indeed no secondary modes above $f_{\mathrm{RF}} - f_{\min}$ (at last within their line width), with $f_{\min}$ being the spin-wave band gap. Having pointed it out, such an observation may occur trivial, as it is a direct consequence of conservation of energy. Still, it substantiates that fact that all signals in the experimental data (see again Fig. 5.2c) above that line must either be higher harmonics and/or come from higher-order magnon-magnon interactions. Furthermore, there are two discrepancies between experimental data and the predicted channels:

(i) In experiments, we also observe resonant channels below 6.1 GHz. Several reasons for this are possible. First, the set of resonant channels is very sensitive to changes in the dispersion. For the numerical calculation of the dispersion and therein the prediction of the channels, MuMax^3 data was used. In the real existing sample, the dispersion can be slightly different (e.g. due to changes in the material parameters, defects in the real sample, discretization effect in the simulation and so forth). This, in return, will alter the resonant channels. Second, the interaction tolerance $\Omega = \Gamma_2$ could have been chosen to be too small and some channels could have been missed. In fact, for the search of the channels, we used $\Gamma = \alpha_G \omega$, but the real line width of the modes is slightly increased, which will be discussed in Sec. 7.1. Third, even channels which are more off-resonant than allowed by the tolerance Ω could be activated if their scattering efficiency $V_{0,12}$ is large enough. However, the scattering efficiency was completely neglected in this approximate prediction. The last possible reason is the nonlinear frequency shift, namely the cross-shift of the secondary modes due to the directly excited mode. The first radial mode $(0, 0)$ is at about 5.4 GHz. Closer to its resonance, the nonlinear ferromagnetic resonance could come into play [40].

(ii) In experiments and also in simulations, we do not observe all of the resonant channels. In a way, we predict too many channels. This is because all channels will have different threshold amplitudes. Once the channel with the lowest threshold is activated, the respective secondary modes will take up energy off the directly excited mode, increasing the threshold fields for the remaining channels. For low excitation powers, the remaining channels will stay *silent*. With increasing power, they will be activated one-by-one, depending on their threshold (see Chap. 8). In fact, these silent channels can even be activated below their threshold by stimulating them (see Chap. 9). In the last part of the current chapter, the scattering efficiency $V_{0,12}$ and, therefore, the thresholds will be taken into account to address the matter of having a decreased number of scattering channels. However, even having predicted *too many* channels, we can still learn a lot about the experimental data.

5.1.3 Focus on azimuthal index

In Fig. 5.3, the predicted frequency sweep is compared with the experimental data, with the predicted secondary modes color-coded by their modulus of the azimuthal index $|m|$. This may help explain the decreased μBLS intensity highlighted by the elliptic area. In this region, the secondary modes exhibit a large azimuthal index $|m| > 30$, leading to large in-plane wave vectors for which μBLS is less sensitive [12]. This is because the wave-vector coverage of a micro-focused laser beam is ultimately limited by the angle range that can be re-collected using an certain objective.

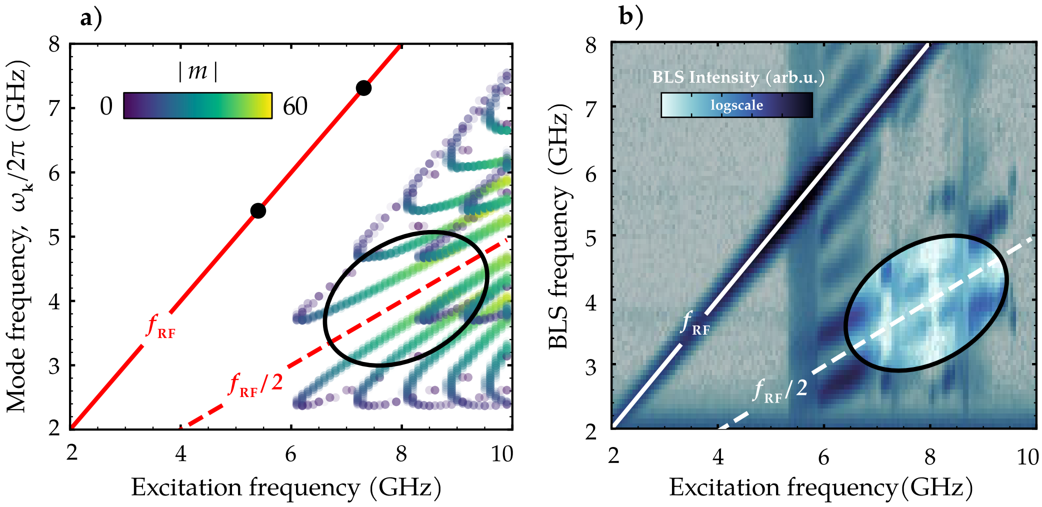

FIGURE 5.3: **a)** Predicted resonant channels color-coded with their azimuthal index $|m|$, compared with **b)** experimental data. The large ellipse marks a region of large $|m|$ / reduced μBLS intensity.

5.1.4 Focus on radial index

An even more interesting feature of these frequency sweeps are the apices that appear for excitation frequencies of 6.1 GHz, 7.2 GHz and 8.0 GHz, among others. In the experiments, depending on the excitation power level, we observe only the tip of them (see 5.4a and 5.4b in comparison). Color-coding the secondary modes with their radial index n reveals that those tips mark points for which the next branch of the dispersion starts to take part in the scattering. In Fig. 5.4c-e, we see the respective resonant scattering channels which mark these beginnings.

As a result of this analysis, it becomes quite obvious what defines the split in frequency $\Delta\omega$ of the secondary modes. It is, of course nothing more than the distance between the different branches of the dispersion at that particular $|m|$.

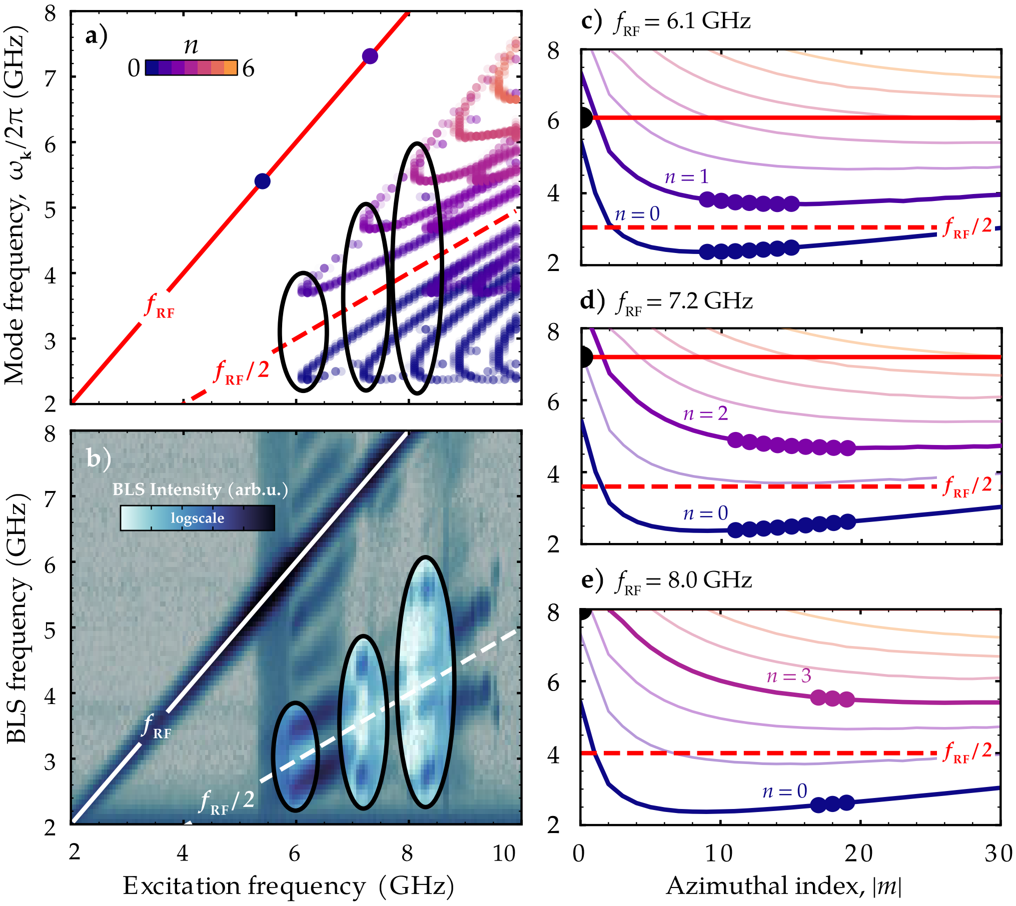

FIGURE 5.4: Origin of apices in frequency sweeps. Elliptic regions in resonant channels **a)** color-coded by their radial index n and **b)** experimental data mark frequencies for which the next branch of the the dispersion takes part in the scattering. **c-e**) show the respective resonant channels.

5.1.5 Effect of nanodisk dimension

The effect of changing the dimension of the nanodisk (here: the diameter D, the thickness $L = 50\,\mathrm{nm}$ is kept constant) on the dispersion of the spin-wave modes has already been discussed in Sec. 4.3. As a consequence, the resonant channels are changed accordingly. For small disk diameters, the average inter-branch distance (of modes with same $|m|$ but different n) is increased, leading to a more pronounced split in frequency $\Delta\omega$ of the secondary modes. Moreover, as the frequencies increase with decreasing diameter, the resonant channels are shifted up in the dispersion. These trends can be seen in Fig. 5.5.

For the 1 µm disk (see Fig. 5.5a,b), another effect can be observed. As the dispersion becomes more and more quadratic, because the exchange regime is reached for smaller $|m|$, the radial modes are not far above a large number of azimuthal modes anymore. As a consequence, one needs to excite fairly high-order radial modes in order to exhaust the collection of channels. For example, to achieve secondary modes with $n_1 = 2$ and $n_2 = 0$, one needs to directly excite radial modes with $n_0 \geq 5$, which couple less effectively to an external field (see Appx. A.2) than lower-order radial modes. In comparison, for the 5.1 µm diameter disk, this was possible with $n_0 = 1$.

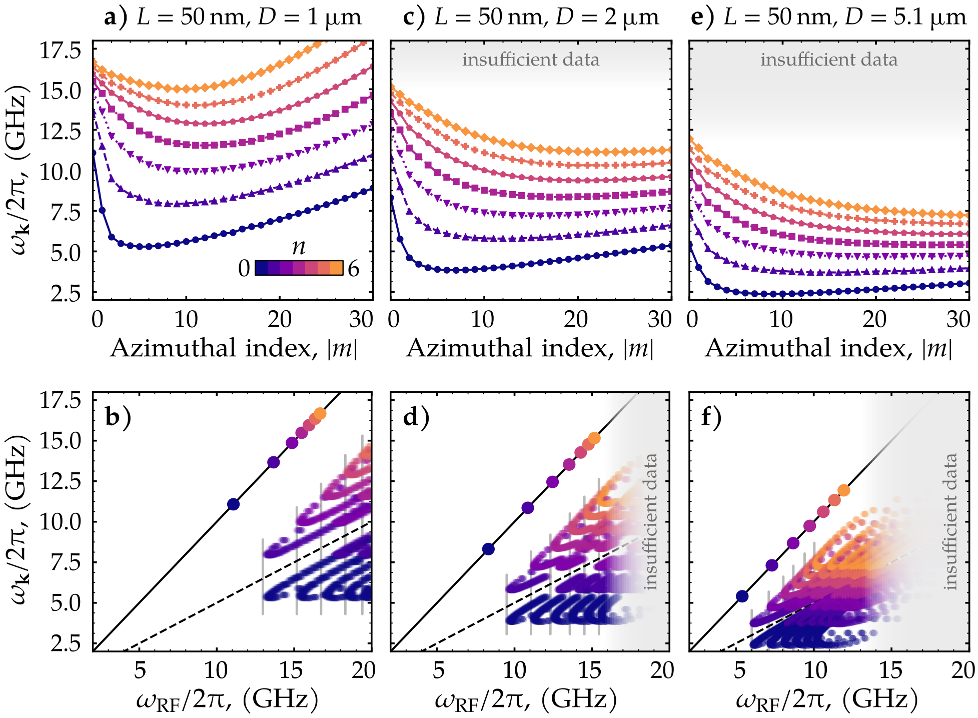

FIGURE 5.5: Comparison of dispersion and resonant scattering channels for 50 nm thick permalloy disks with **a), b)** 1 µm, **c), d)** 2 µm and **c), f)** 5.1 µm diameter. All modes are color-coded with their radial index. the gray overlays indicates regions where the dispersion data was not sufficient to calculate the scattering channels properly. The horizontal gray lines mark the excitation frequencies for which the next higher radial branches takes part in the scattering.

5.2 Inclusion of thresholds

In order to predict the channels which will be excited for the lowest excitation powers, one has to take into account the three-magnon scattering efficiency $V_{\mathbf{0},\mathbf{12}}$ to compare the threshold fields. Theoretical values for these fields have been obtained by our collaborator Roman Verba also using the dispersion data acquired by simulation in Sec. 4.3. The results have been verified by experimental data as well as micromagnetic simulations, but are – as of the submission date of this thesis – not yet published in a journal but will be as a talk at MMM Las Vegas 2019 [85]. The contribution of the author of this thesis to the aforementioned effort is documented in this section. Specifically, next to calculating and supplying the dispersion, threshold fields as well as mode numbers for the secondary modes for selected excitation frequencies were obtained by micromagnetic simulations.

5.2.1 Theoretical threshold fields

In the case of a continuous spin-wave spectrum and ignoring nonlinear frequency shift as well as feedback on the directly excited mode, the threshold field of a particular channel would be [4]

$$b_{\text{crit}} \propto |c_{\mathbf{0},\text{crit}}| = \frac{\sqrt{\Gamma_{\mathbf{1}}\Gamma_{\mathbf{2}}}}{|V_{\mathbf{12},\mathbf{0}}|}. \tag{5.6}$$

with the damping rates of the secondary modes $\Gamma_{\mathbf{1},\mathbf{2}}$. In the end, this simply means that the secondary modes are lifted from their thermal level as soon as the energy flux, which is supplied by the decay of the directly excited mode overcompensates the internal losses of the secondary modes. However, we have already discussed that in our case we have a discrete mode spectrum for which exact resonance of the three-magnon scattering can hardly be realized. This slight detuning from the resonance condition will renormalize the threshold fields [4]

$$b_{\text{crit}} \propto |c_{\mathbf{0},\text{crit}}| = \frac{\sqrt{\Gamma_{\mathbf{1}}\Gamma_{\mathbf{2}}}}{|V_{\mathbf{12},\mathbf{0}}|}\left(1 + \frac{\Delta\Omega^2}{(\Gamma_{\mathbf{1}} + \Gamma_{\mathbf{2}})^2}\right)^{\frac{1}{2}}. \tag{5.7}$$

Here, $\Delta\Omega = \omega_{\text{RF}} - (\omega_{\mathbf{1}} + \omega_{\mathbf{2}})$ is the detuning of a particular channel from the resonance condition. It becomes clear that the threshold fields in a discrete system are very sensitive to the frequencies of the modes. This is the reason, why for the final calculation of the threshold fields, the dispersion data from Sec. 4.3 was used by Dr. Verba. Otherwise, the comparison with simulation would be ambitious, which the reader will see soon.

The damping rates as well as the three-magnon efficiency were calculated from the mode profiles. In particular, $V_{\mathbf{12},\mathbf{0}}$ was derived as one of the first exertions of a newly developed vector-Hamiltonian formalism for nonlinear spin-wave dynamics. Again, the details on this theoretical analysis will be submitted for publication soon.

5.2.2 Numerical determination of threshold fields

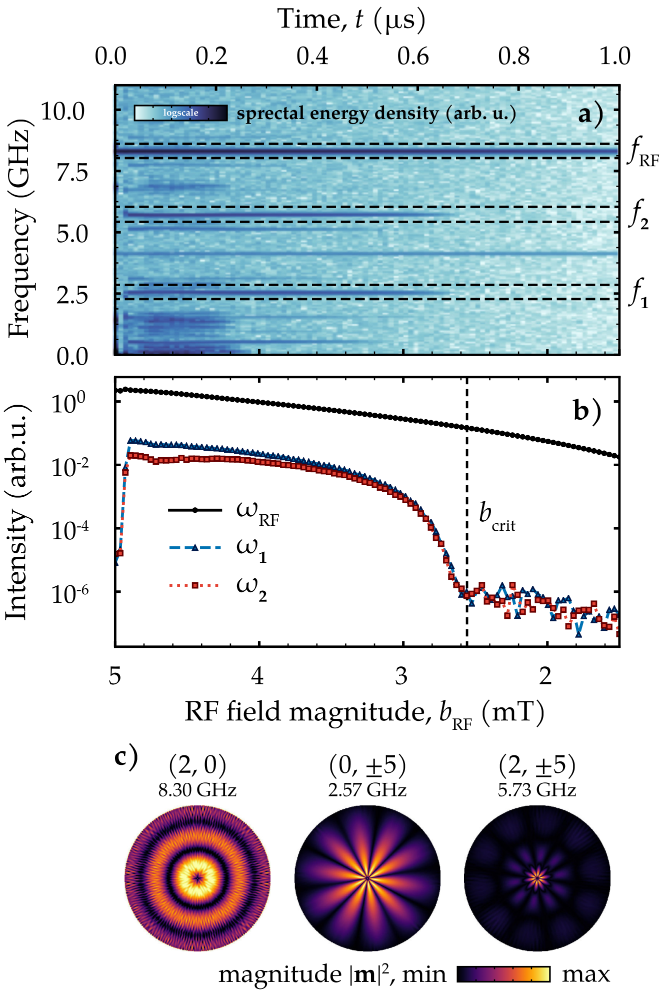

FIGURE 5.6: Determination of the threshold field b_{crit} at $f_{RF} = 8.3\,\text{GHz}$ with **a)** the total-energy spectrogram of a down-sweep of the RF field magnitude over 1 µs. The highlighted areas mark the frequency channels which were integrated and **b)** plotted against field to allow for an extraction of the critical field b_{crit} of the **c)** modes of this channel.

The procedure of determining the threshold of a particular channel using MuMax^3 is quite similar to the experimental one by means of BLS. One simply sweeps the excitation power of the RF field at a given excitation frequency and then searches for the appearance of the secondary modes (e.g. see Fig.3a in [20]). However, in the experiments it is difficult to determine the exact amplitude of the RF field generated by the micrometer-sized antenna around the sample. Only the power of the microwave generator is known with certainty. This is the reason, why a quantitative comparison with theory and simulation in terms of threshold fields is not possible up to this point[2]. For this thesis, a lightweight approach was developed to acquire the threshold fields using only a single simulation per excitation frequency. One starts with a field amplitude above the threshold (this starting field is determined by trial and error) and then slowly decreases the amplitude of the excitation field over the course of 1 µs. The reason, why we do not increase the field from zero is the following: The secondary modes only appear after a certain time delay with respect to the RF field which excites the direct mode. This is due to the fact that the directly excited mode first has to build up its amplitude before it reaches the decay instability. If we increase the field too fast, then we will miss the threshold field. It is therefore better to decrease the field and wait for the secondary modes to disappear. Of course, in a BLS experiment this problem does not occur since field sweeps are performed over several seconds or even minutes. But in numerics, a simulation time of 1 µs is already huge (typical simulation times in micromagnetics are in the order of 10–100 ns). Additionally, performing a spatially dependent Fourier transform over such a time span is not feasible. The effectiveness of this methods now lies in the fact that we perform a time-frequency analysis only on the total magnetic energy, which is a spatially independent quantity. The time-frequency analysis is achieved by performing a windowed FFT within smaller time slices. As a result, one obtains a spectrogram – that is, a time-dependent FFT – of the total magnetic energy. A more elaborate description is found in Appx. A.1. For example, in Fig. 5.6, we see the total-energy spectrogram of a field sweep from 5 to 1.5 mT at an excitation frequency of 8.3 GHz. After a certain amount of time, the secondary modes disappear. This point in time approximately corresponds to the point for which the field drops below the threshold. By integrating the spectral density over a certain interval around the frequencies of the secondary modes and changing over from time-axis to field-axis (see Fig. 5.6b) one can obtain the threshold field.

---

[2] Although in-situ field measurements using NV-centers or SiC-defects have been proposed [86, 87].

Finally, the modes within a channel are identified by performing an additional 100 ns long simulation at a constant RF field amplitude above the threshold. The mode profiles (Fig. 5.6c) are then obtained using the full spatially-dependent Fourier analysis. The threshold fields from simulation and theory can be seen in Tab. 5.1 together with the mode indices in each channel. The indices are the same for simulation, theory and, in fact, also experiment [20]. This means, that simulation and the theoretical analysis by calculating $V_{\mathbf{12,0}}$ are successful in predicting the correct channels with the lowest threshold. The threshold fields from simulation are slightly higher than the ones from theory which can be due to the high sensitivity of the threshold fields on the mode frequency as well as the fact that the vortex core was neglected in the theoretical analysis.

f_{RF} (GHz)	$b_{\mathrm{crit}}^{(\mathrm{theo})}$ (mT)	$b_{\mathrm{crit}}^{(\mathrm{sim})}$ (mT)	n_0	n_1	n_2	$\lvert m\rvert$
6.1	1.12	1.26	0	1	0	12
7.2	2.75	3.40	1	1	0	4
8.3	2.95	2.62	2	2	0	5
8.9	0.93	1.80	2	2	1	9
9.0	1.45	2.10	2	2	1	8

TABLE 5.1: Threshold fields (theory $b_{\mathrm{crit}}^{(\mathrm{theo})}$ and simulation $b_{\mathrm{crit}}^{(\mathrm{sim})}$) and mode indices for the channels $(n_0, 0) \to (n_1, |m|) + (n_2, |m|)$ with the lowest threshold at different excitation frequencies f_{RF}.

Chapter 6

Influence of static external fields

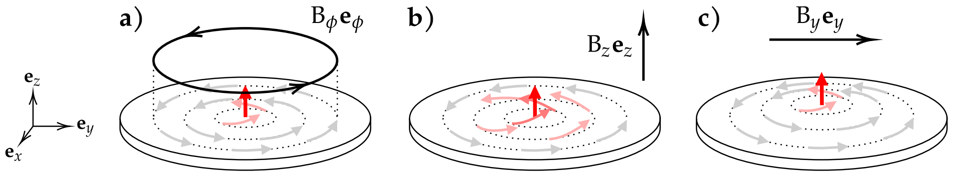

azimuthal
in-plane field

homogeneous
out-of-plane field

homogeneous
in-plane field

FIGURE 6.1: Schematics of the different external field orientations with respect to the vortex disk. The resulting new equilibrium magnetization is additionally outlined by the gray and red arrows (color-coded with increasing out-of-plane component).

The three-magnon scattering channels within a magnetic vortex can change quite drastically if static external fields $\mathbf{B}_{\text{ext}}$ are applied. Such fields will lead to a change of the equilibrium magnetization $\mathbf{M}_{\text{eq}}$, thereby inducing a change in the mode profiles and frequencies. The present chapter shall take a small detour to touch on this matter for the case of static homogeneous out-of-plane (OOP) and in-plane (IP) fields. The former case retains the cylindrical symmetry whereas the latter case will break it. Quite counter-intuitively, we will see that OOP fields suppress three-magnon scattering, whereas IP fields will open up the route to completely new and exotic vortex modes. Both of these cases will turn out to be far too extensive to cover them here to the extend they would deserve. For the sake of completeness, the initial section will briefly cover the case of an azimuthal in-plane field.

6.0 Azimuthal in-plane field

In addition to being the most difficult to realize experimentally, the case of an azimuthal in-plane field $\mathbf{B}_{\text{ext}} = B_\phi \mathbf{e}_\phi$ (see Fig. 6.1a) is also the least fascinating. Next to a change in the vortex core radius, applying a static field anti-/parallel to the original equilibrium magnetization will only decrease or increase the effective internal field. The change in mode profiles and dispersion will not qualitatively change the resonant channels. One has to admit that using an azimuthal in-plane field can be advantageous, for example, if it leads to a more pronounced backward-volume character of the dispersion, meaning that the radial modes are shifted to larger frequencies relatively to azimuthal modes with large $|m|$. As a consequence, the frequency space of possible scattering channels could be widened.

6.1 Homogeneous out-of-plane field

Under the influence of a homogeneous OOP field $\mathbf{B}_{\text{ext}} = B_z \mathbf{e}_z$ (see Fig. 6.1b), a (circular) magnetic vortex will transform into a cone-state vortex. Depending on whether the polarity of the vortex is parallel or anti-parallel to the external field, the core will either grow or shrink, whereas the surrounding magnetization will tend to align itself parallel to the field. One may refer the first case (core polarity parallel to the field) as a *light* vortex and to the latter case (core polarity anti-parallel to the field) as a *heavy* vortex. A heavy vortex is not easily modeled in micromagnetic simulation as the core radius can decrease down to a few lattice constants before the core finally flips and aligns itself parallel to the field. In such an extreme case, speaking of a continuous magnetization becomes ambitious. The terminology light and heavy was introduced by Prof. Boris Ivanov in reminiscence of the energy barrier between the two orientations [73]. Ivanov et al. studied both cases in great detail from a theoretical point of view. During the work on this thesis, a collaboration with Prof. Ivanov emerged which has its focus on the linear characteristics of spin-wave modes in a (light) cone-state vortex. Nevertheless, there are also consequences on the nonlinear characteristics because, as already mentioned, the three-magnon scattering in a cone-state is suppressed.

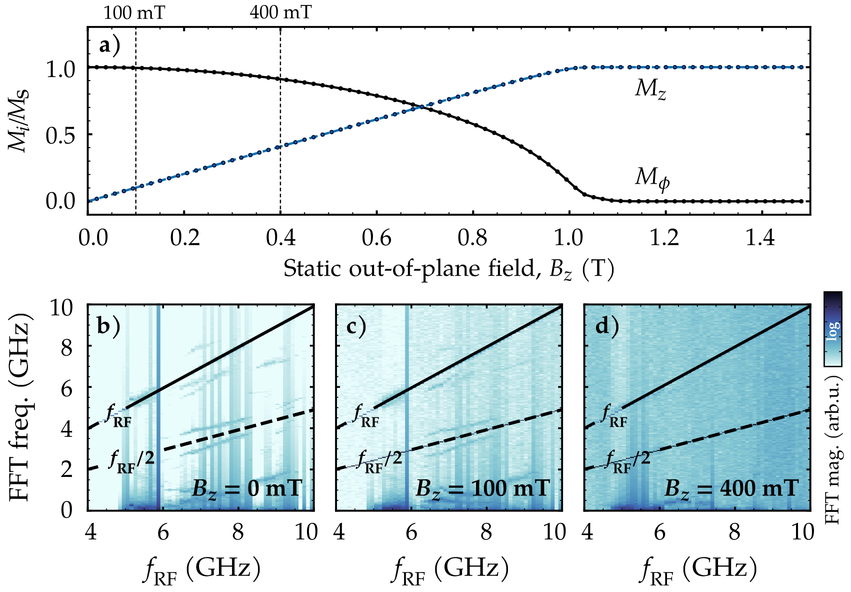

FIGURE 6.2: **a)** Averaged out-of-plane Mz and in-plane component $M_\phi = \left\langle \sqrt{M_x(\mathbf{r})^2 + M_y(\mathbf{r})^2} \right\rangle$ of a light vortex as a function of applied OOP-field. The dissappearance of the secondary modes can be seen by comparing th the simulated RF sweeps for **b)** 0 mT, **c)** 100 mT and **c)** 400 mT static OOP-field strength.

In Fig. 6.2a, we see the phase transition[1] of an in-plane vortex to a light cone-state vortex to the fully saturated state in the case of our 5.1 µm diameter permalloy disk, expressed by the averaged out-of-plane M_z and in-plane component M_ϕ. This transition in the ground state (and also in the spin-wave modes which we will discuss in a moment) was for example also investigated by Taurel et al. in [76]. We see the disk is fully saturated as soon as the OOP field is equal to the saturation magnetization, $B_z = \mu_0 M_s \approx 1\,\mathrm{T}$ (for permalloy). The data for the field-dependent ground state was acquired with MuMax^3 by running an OOP-field sweep with increased $\alpha_G = 0.5$ to suppress dynamics, and recording the magnetization in a given time/field interval. If we look at simulated excitation frequency sweeps for exemplary OOP field values (see Fig. 6.2b-d), we see that the secondary modes disappear with increasing field. The sweeps were obtained by running a 100 ns long simulation for each RF excitation frequency at $b_{\mathrm{RF}} = 5\,\mathrm{mT}$ and subsequently taking the Fourier transform of the total magnetic energy (see Sec. 5.2 and Appx. A.1).

---

[1] The system undergoes a transition from circularity number $\chi = \pm 1$ to $\chi = 0$. Thus, the phase transition is of a topological nature.

There are a couple of distributions that may lead to a suppressed intensity of the secondary modes:

(i) The most obvious but not most drastic reason is the decreased transversal coupling of the RF field (which is also an OOP field) as the equilibrium magnetization points more and more out-of-plane. However, for $B_z = 400\,\mathrm{mT}$ the magnetization still retains a considerable in-plane component, yet the secondary modes have completely disappeared. This holds true even if one increases the RF power to counteract the decreased coupling efficiency.[2] As a consequence, there have to be other contributions.

(ii) The second possible reason is a change of the mode profiles (see e.g. [76]) which leads to a change in the three-magnon efficiency $V_{\mathbf{0},\mathbf{12}}$. To solidify this, one has to calculate the mode profile for a number of static OOP-fields. However, decreasing the three-magnon efficiency is in some way equivalent to decreasing the pumping efficiency of the direct mode - at least when it comes to threshold fields. Thus, the same argument made at the end of the previous point holds.

(iii) The third and probably most important reason is that the degeneracy of the duplets $\pm m$ is lifted when an OOP-field is applied, rendering the three-magnon channels to be off-resonant. Hence, we will discuss this reason in more detail.

The last of the aforementioned reasons makes the spin-wave modes in a cone-state vortex quite interesting. We can see in Fig. 6.3 for the case of $|m| = 8$ that all mode frequencies go down with increasing OOP field. This is expected for in-plane materials which are exposed to an OOP field and quite common in ferromagnetic resonance experiments [26].

However, in addition to the decrease in frequency, the duplets split up with increasing OOP-field strength. The data in Fig. 6.3 was acquired the same way like the spectra for the dispersion in 4.3, only that the field and not the azimuthal index was changed from simulation to simulation. The reason for lifting of the degeneracy is a topological effect which was proposed for spin waves by Braun [88], Hertel [89] or Dugaev [90] and is the subject of the collaboration with Boris Ivanov. The situation is that the azimuthal modes acquire a Berry phase in the presence of a static OOP field. This

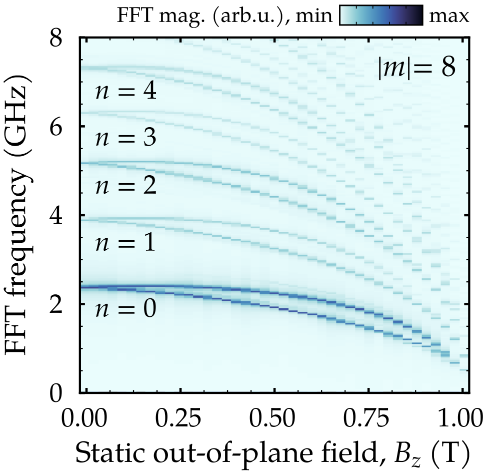

FIGURE 6.3: Splitting of the duplets with $|m| = 8$ as a function of applied OOP field.

---

[2] Tobias Hula performed BLS experiments to support this. The results are not published yet.

Berry phase, in return, intrinsically leads to a non-reciprocity in ϕ-direction. The lifting of the duplet degeneracy together with the fact that all mode frequencies decrease (generally in a quite individual way) makes it increasingly more difficult for the three-magnon channels to maintain resonance. For $B_z = 100\,\mathrm{mT}$ the duplets are already split but the respective channel are still resonant within line width. However, at $B_z = 400\,\mathrm{mT}$, the resonance is gone completely.

6.2 Homogeneous in-plane field

As already mentioned, the situation is very different if a homogeneous in-plane field applied which breaks the cylindrical symmetry. Against intuition, three-magnon scattering will not be suppressed. On the contrary, it will uncover rather exotic spin-wave modes. Consider the case of the IP-field $\mathbf{B}_{\mathrm{ext}} = B_y \mathbf{e}_y$ being applied in the y-direction as in Fig. 6.4.

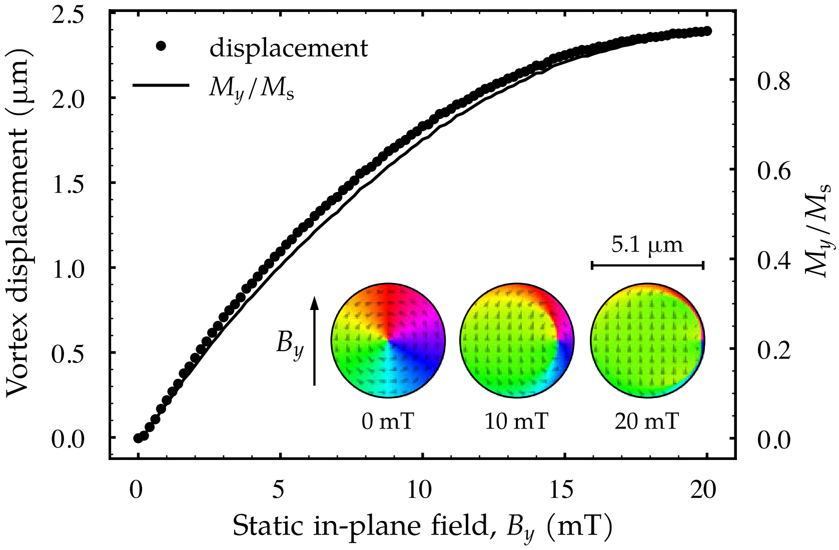

FIGURE 6.4: Displacement of the vortex in a 50 nm thick permalloy disk of 5.1 µm diameter as a function of applied IP field B_y compared with the ratio M_y/M_s. The vortex position was acquired using peak-fitting of the simulation data along line scans. The insets show the color-coded polar angle of the equilibrium magnetization $\mathbf{M}_{\mathrm{eq}}$ for exemplary IP-field values.

The data was again acquired by means of micromagnetic simulation performing a sweep of the external field with increased damping. We see that the vortex is displaced transversal to the IP-field, with the exact direction being defined by the circularity of the vortex. At a field of $B_y = 20\,\mathrm{mT}$, the vortex is almost completely pushed towards the edge of the disk. Furthermore, we see that the ratio M_y/M_s (with the averaged component parallel to the IP-field M_y) provides a good estimate for the relative displacement for the vortex.

In the following, we will take a look at what happens to the nonlinear dynamics – in particular the scattering channels – with increasing IP-field for the exemplary case of $f_{\mathrm{RF}} = 6.1\,\mathrm{GHz}$ at $b_{\mathrm{RF}} = 3\,\mathrm{mT}$. For this purpose, a series of micromagnetic simulations was performed using a RF excitation. In Fig. 6.5a, we see the respective power spectra for increasing IP-field B_y. First of all, the secondary modes do not disappear if the IP-field is increased. On the contrary, at some critical field $B_y \approx$

2.5 mT the signal of the secondary modes splits into two branches each. On top of it, we will shortly see that the secondary modes will be divided into two qualitatively very different sets.

Recall, that the splitting of the azimuthal modes for OOP-fields in the previous section was a purely *linear* effect. Here, we observe a splitting of the secondary modes which are produced by a *nonlinear* effect.

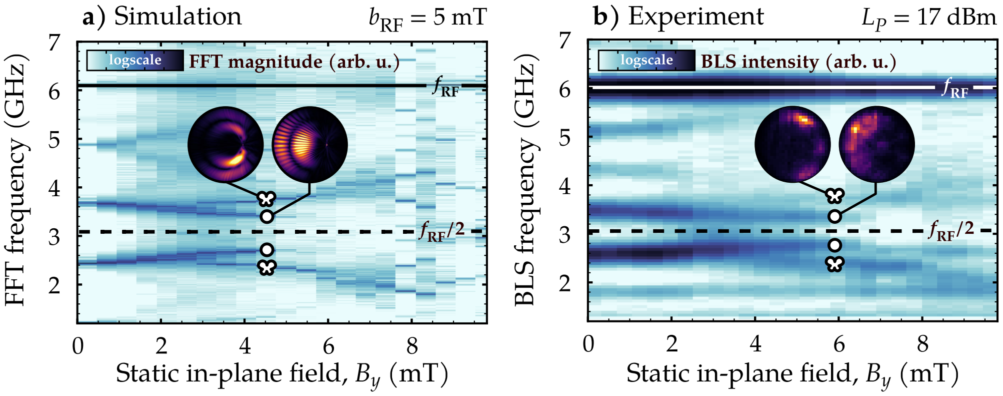

FIGURE 6.5: Frequency spectra of the three-magnon channel(s) at $f_{\mathrm{RF}} = 6.1\,\mathrm{GHz}$ as a function of applied IP field B_y acquired with **a)** micromagnetic simulation and **b)** micro-focused BLS. The insets in both subfigures show the mode profiles at the respective frequencies, obtained from simulation or by µBLS. The experimental data was obtained by scanning over a ring-shaped area on the disk and integrating the respective Stokes and Anti-Stokes signal. The circles and butterfly shapes indicate the branches of the two different classes of vortex modes, as well as the points for which the mode profiles shown later in Fig. 6.6 were taken.

The micromagnetic simulations described in this section motivated the experimental realization by means of µBLS, performed by Katrin Schultheiß on 5.1 µm iameter permalloy disks as well. The experimental results are in a gratifying qualitative agreement with numerics (see Fig 6.5b). Discrepancies could be related to the lack of knowledge of the exact RF power level L_P in the experiments, as well as discretization effects in the numerical data. It could be, that in the experiment, the excitation field is slightly higher than in the simulation. Additionally, at the time of the experiments, there was a setup-related asymmetry between Stokes and Anti-Stokes signal. This is why in all the measurements presented here, both sides are always accumulated.

If we take a look at the mode profiles (see insets in Fig. 6.5), we find that the secondary modes split into two classes of modes, one type located on the far sight of the displaced vortex, which are the usual vortex modes associated modes in an undisplaced vortex.

It has to be noted that azimuthal modes in a displaced vortex have been studied both numerically as well as experimentally e.g. in [91, 92], however only for modes up to $|m| \leq 2$, due to limitations by computational power or experimental design. In extension to the undisplaced case presented [20], three-magnon scattering provides the means to excite higher-order azimuthal modes ($|m| \gg 2$) in a displaced magnetic vortex.

Coming back to the present analysis, we see that the other branches in the IP-field sweep belong to secondary modes with a more exotic profile. These *butterfly* vortex modes (as we will call them for the lack of a better term) have their main amplitude right next to the vortex, generating a butterfly pattern (see Fig 6.6).

Notably, both the regular vortex modes as well as the butterfly vortex modes generated by three-magnon scattering in a displaced vortex still obey the same selection rules which we have discussed for the undisplaced case in Sec. 5.0. In other words, the selection rules of the decay of a radial vortex mode into other modes in a magnetic vortex are robust against displacement of the vortex.

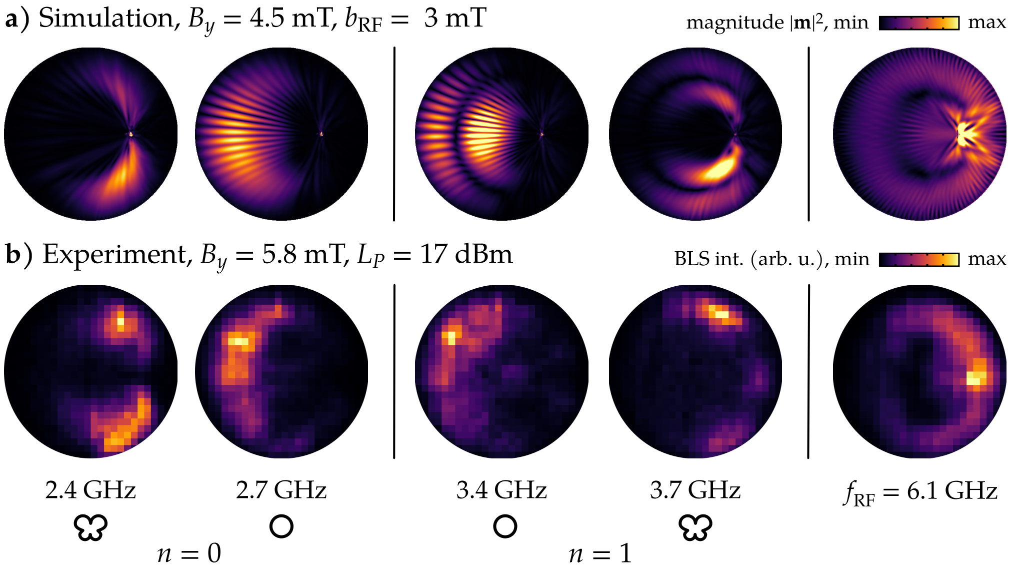

FIGURE 6.6: Mode profiles of the two different classes of regular (circle) and butterfly vortex modes acquired by **a)** micromagnetic simulation and **b)** micro-focused BLS. The respective IP fields were set to a value for which all modes are in co-existence (see Fig. 6.5). As a consequence, the vortex displacement for simulation and experiment is slightly different. The experimental profiles were acquired by integrating in a certain line width and adding up the respective Stokes and Anti-Stokes peaks.

In order to fully understand the transition of the secondary modes even only for the exemplary case presented in Figs. 6.5 and 6.6, it is vital to gain knowledge about the dispersion $\omega(\mathbf{k}, B_y)$ and mode profiles also for higher order azimuthal modes as a function of applied the IP field. Unfortunately, theoretical approaches such as the projection method [77] or the numerical approach developed in Sec. 4.3 must fail as we cannot make a priori assumptions about the mode profiles (such as the azimuthal dependence $\propto e^{im\phi}$) in order to transform the LLG equation of motion to an ordinary differential equation on the one hand, or to find suitable excitation fields on the other hand. The only way out may be the rigorous numerical diagonalization of the linearized LLG equation of motion using a dynamics matrix approach such as the one introduced by Grimsditch et al. [93] (which has already been used in the aforementioned publication [91] to calculate lower azimuthal modes) or the even more recently extended one by d'Aquino et al. [94]. Such an effort would go far beyond the scope of this thesis but is a project envisaged for the future.

Chapter 7

Rate equations for nonlinear dynamics

In the previous chapters, we have shed light on the linear characteristics of the spin-wave modes in a vortex, discussed the possible three-magnon-scattering channels, and obtained their threshold for exemplary cases. In order to take the next step and study the time- and power-dependence of the three-magnon scattering – that is, understanding the evolution of the spin-wave numbers $N_{\mathbf{k}}(t)$ involved in a particular channel – one needs to engage into nonlinear spin-wave theory. During the work on this thesis, a considerable amount of time was spent in literature research and practice in order to be able to apply this theory to the nonlinear dynamics that were observed experimentally [20] as well as in simulations. The objective was to develop rate equations which describe the evolution and interaction of the complex amplitudes $c_{\mathbf{k}}(t)$ of the spin waves taking part in the scattering, using the classical Hamiltonian formalism presented in Sec. 2.3.3. After having developed the rate equations in this chapter, we will use them to further study the nonlinear spin-wave dynamics in the following chapters. The reader which is eagerly waiting for the next physical results is encouraged to skip this chapter and continue with Chap. 8.

Recall, that a complex spin-wave amplitude $c_{\mathbf{k}}(t)$ (and its complex conjugate $c^*_{\mathbf{k}}(t)$) is a classical analogon to the quantum mechanical annihilation and creation operators $c_{\mathbf{k}}$ and $c^\dagger_{\mathbf{k}}$. Accordingly, the modulus square $N_{\mathbf{k}} = |c_{\mathbf{k}}|^2$ of the respective spin-wave amplitude is analogous to the magnon occupation number and proportional to the measured intensity in a BLS experiment, therein. A particular rate equation for a given complex spin-wave amplitude $c_{\mathbf{k}}(t)$ will be of the form

$$\frac{\mathrm{d}c_{\mathbf{k}}}{\mathrm{d}t} = -i\omega_{\mathbf{k}}c_{\mathbf{k}} - \underbrace{\Gamma_{\mathbf{k}}(c_{\mathbf{k}}}_{\text{(i)}} - \underbrace{c_{\mathbf{k},\text{th}})}_{\text{(ii)}} + \underbrace{iP_{\mathbf{k}}b_{\text{RF}}e^{-i\omega_{\text{RF}}t}}_{\text{(iii)}} - \underbrace{i\frac{\partial\mathcal{U}_{\text{int}}}{\partial c^*_{\mathbf{k}}}}_{\text{(iv)}}, \tag{7.1}$$

with the damping rate $\Gamma_{\mathbf{k}}$ and the coupling $P_{\mathbf{k}}$ to an external microwave field with magnitude b_{RF} and angular frequency ω_{RF}.

For each mode taking part in the nonlinear dynamics, we will acquire such an equation. After having obtained the numerical solutions, the modulus square of these can be compared with experimental data. The numerical solutions for the equations are obtained by an implementation in Python [95, 96]. Several revisions of the code were done to improve performance. The curious reader is encouraged to visit Appx. A.3 which documents this matter.

In the rate equations (such as Eq. 7.1), we have included (i) linear mode damping, (ii) thermal spin waves, (iii) pumping by external microwave fields, as well as (iv) the nonlinear interaction with other spin-wave modes. In the following sections of this chapter, the development as well as the implementation of these different terms will be described and justified in detail.

7.1 Linear mode damping

Not only does the damping of a spin-wave mode influence the linear dynamics, as it leads to an attenuation of its propagation, but it also plays a crucial role in the nonlinear regime. For example, the instability threshold of a directly excited mode crucially depends on the damping of the secondary modes (see again Sec. 5.2). In the rate equations derived by a classical spin-wave Hamiltonian $\mathcal{U}$, damping is typically included in the following way [4]:

If we neglect all nonlinear processes and set $\mathcal{U} = \mathcal{U}^{(2)}$, then the canonical equations for the different modes are completely decoupled and we obtain

$$\left[\frac{\mathrm{d}}{\mathrm{d}t} + i\omega_{\mathbf{k}}\right] c_{\mathbf{k}}(t) = 0. \tag{7.2}$$

The solutions are of the form $c_{\mathbf{k}}(t) \propto e^{-i\omega_{\mathbf{k}}t}$. In order to include linear damping, an imaginary part $-i\Gamma_{\mathbf{k}}$ is added to the frequency $\omega_{\mathbf{k}}$. This is done in a phenomenological manner in anticipation of an exponential decay. This can also be understood by looking at the LLG equation since Gilbert damping is proportional to $\mathrm{d}\mathbf{M}/\mathrm{d}t$. The origin of wave damping can be of various natures. Thus

$$\left[\frac{\mathrm{d}}{\mathrm{d}t} + \Gamma_{\mathbf{k}} + i\omega_{\mathbf{k}}\right] c_{\mathbf{k}}(t) = 0. \tag{7.3}$$

Now, the solutions are exponentially decaying $c_{\mathbf{k}}(t) \propto e^{-\Gamma_{\mathbf{k}}t}e^{-i\omega_{\mathbf{k}}t}$. This procedure is only valid as long as the damping rates $\Gamma_{\mathbf{k}} \ll \omega_{\mathbf{k}}$ are small. Large dampings must be treated differently, since adding an imaginary part to the frequency leads to a complex value of the spin-wave Hamiltonian $\mathcal{U}$.

In principle, the damping of a spin-wave mode is nonlinear, i.e., it depends on the spin-wave numbers $N_{\mathbf{k}} = |c_{\mathbf{k}}|^2$ of the excited modes in the system,

$$\Gamma_{\mathbf{k}} = \Gamma_{\mathbf{k},0} + \sum_{\mathbf{k}'} \mu(\mathbf{k}, \mathbf{k}') N_{\mathbf{k}} + \ldots \tag{7.4}$$

This fact is very important, for example, in the theory of spin-torque oscillators, for which the power of the spin-wave mode that corresponds to the auto-oscillation is typically not limited by a decay into other modes.[1] In that case, the power of this mode can grow very large and lead to a nonlinear damping [17]. However, in the case of three-magnon scattering in a vortex, it is reasonable to assume that the spin-wave numbers are limited by the decay processes such that damping remains in the linear regime – at least for excitation powers not far above the threshold. It is possible that for excitation powers which are far above threshold, an extension of the presented theory has to be made in order to account for nonlinear damping.

In general, the linear damping of a spin-wave mode $c_{\mathbf{k}}$ in a thin magnetic element is described by

$$\Gamma_{\mathbf{k}} = \alpha_G \epsilon_{\mathbf{k}} \omega_{\mathbf{k}}, \tag{7.5}$$

with the Gilbert damping α_G. The coefficient $\epsilon_{\mathbf{k}}$ is related to the elliptic precession of the dynamic magnetization and can depend on the spatial mode profiles. In the case of spatially uniform precession in a bulk material, this factor is equal to one and leads to $\Gamma = \alpha_G \omega$ but is usually larger in thin elements, leading to an increased damping. The origin and determination of this coefficient $\epsilon_{\mathbf{k}}$ is found in great detail e.g. in [68] by Verba et al. In fact, Dr. Verba provided the ellipticity coefficients for the spin-wave modes in the 5.1 µm diameter disk. The coefficients as well as the resulting damping rates which were calculated using the dispersion data from Sec. 4.3 can be seen in Fig. 7.1 for the first three radial branches ($n = 0, 1, 2$).

---

[1] Usually, auto-oscillations build up from the lowest mode of the spin-wave spectrum at hand [17].

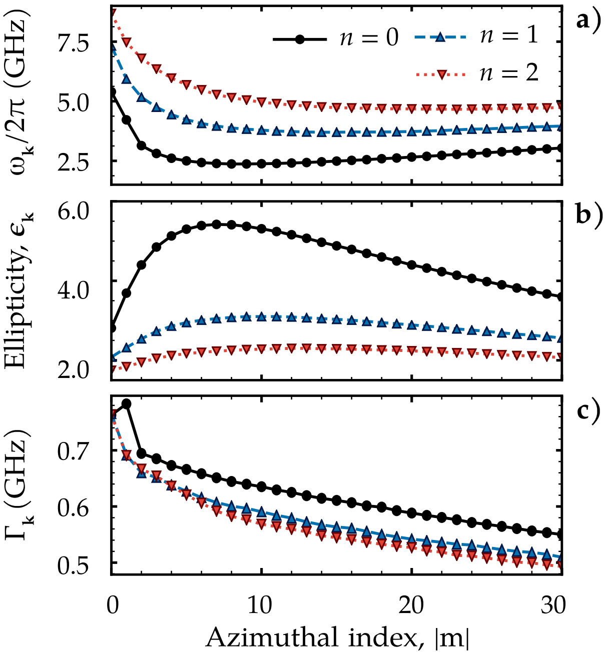

FIGURE 7.1: Dispersion, ellipticity and damping rate of the spin-wave modes with $n = 0, 1, 2$ in a 50 nm thick permalloy disk with 5.1 µm diameter. **a)** The dispersion was acquired by micromagnetic simulation, as described in Sec. 4.3. **b)** The ellipticity $\epsilon_{\mathbf{k}}$, which contributes to the damping of the modes, was obtained from the mode profiles by Roman Verba [68]. Finally, **c)** the damping rate $\Gamma_{\mathbf{k}}$ of the modes was calculated according to Eq. 7.5 for a Gilbert damping of $\alpha_G = 0.008$. The dispersion data acquired in Sec. 4.3 was used.

Overall, we see that the coefficient $\epsilon_{\mathbf{k}}$ is the largest for modes with $n = 0$. As a consequence, these modes have larger damping than modes with $n > 0$, although being lower in frequency. More counter-intuitively, even for higher order azimuthal modes $m > 10$ the damping goes down, as the decrease in the ellipticity coefficient $\epsilon_{\mathbf{k}}$ overcompensates the increase in frequency. These observations illustrate, that the assumption of $\Gamma_{\mathbf{k}} = \alpha_G \omega_{\mathbf{k}}$ would be insufficient. One has to add, that mechanical imperfections of the sample, which could lead to an increased Gilbert damping at the edge of the disk [68], were ignored in this discussion.

7.2 Pumping by external microwave fields

Before discussing the announced thermal spin-waves, we will discuss the effect of external microwave fields, because we can use this knowledge to model thermal spin-waves in the next section.

To drive spin-wave dynamics into the nonlinear regime, the modes need to be driven by an external stimulus which, in our case, is an out-of-plane RF field $\mathbf{b}_{\mathrm{RF}}(\mathbf{r}, t)$ acting on the magnetization $\mathbf{M}(\mathbf{r}, t)$. The following will give an overview how the effect of such a field is included in the rate equations. The curious reader can find the detailed derivation, which has been performed for this thesis, in Appx. A.2.

7.2.1 Determination of the mode coupling

The coupling to a certain spin-wave mode $c_{\mathbf{k}}(t)$ within the classical Hamiltonian formalism can be retrieved by evaluating the Zeemann energy functional (in units of frequency)

$$\mathcal{U}_\mathrm{Z} = -\frac{\gamma}{M_\mathrm{s} V} \int_V \mathrm{d}^3 r \, \mathbf{b}_\mathrm{RF}(\mathbf{r}, t) \cdot \mathbf{M}(\mathbf{r}, t). \tag{7.6}$$

Following the classical Hamiltonian formalism, this is achieved by accurately converting the magnetization $\mathbf{M}(\mathbf{r}, t)$ into spin-wave amplitudes $c_{nm}(t) = c_{\mathbf{k}}(t)$ and finally performing the integral over the whole sample volume. We will write out the mode indices (n, m) explicitly as they will be important for the coupling to RF fields. We have already pointed out before that the azimuthal modes with $m \neq 0$ do not exhibit a net magnetic moment and, as a consequence, do not couple to a homogeneous OOP field. One needs an external field with the same azimuthal symmetry as the respective mode – a fact that was used e.g. in Sec. 4.3 to calculate the dispersion relation of the vortex modes. If we take such a field with azimuthal index m',

$$\mathbf{b}_\mathrm{RF}(\phi, t) = b_\mathrm{RF} e^{i\omega_\mathrm{RF} t} \cos\left(m'\phi\right) \cdot \mathbf{e}_z \tag{7.7}$$

and perform all the conversion steps, the Zeemann Hamiltonian can be written as

$$\mathcal{U}_\mathrm{Z} = -b_\mathrm{RF} e^{i\omega_\mathrm{RF} t} \sum_{nm} P_{nmm'} c_{nm}(t) + \mathrm{c.c.} \tag{7.8}$$

The coupling $P_{nmm'}$ is in its essence retrieved by integrating the product of the external field and the respective mode profile over the sample volume,

$$\begin{aligned} P_{nmm'} &= \frac{\gamma}{\pi R^2} \int_A \mathrm{d}r \, \mathrm{d}\phi \; r \; \Psi_{nm}(r) e^{im\phi} \cos\left(m'\phi\right) \\ &= \frac{\gamma}{2\pi R^2} \int_A \mathrm{d}r \, \mathrm{d}\phi \; r \; \Psi_{nm}(r) e^{im\phi} \left(e^{im'\phi} + e^{-im'\phi}\right) \\ &= \frac{\gamma}{R^2} \int_0^R \mathrm{d}r \; r \; \Psi_{nm}(r) (\delta_{m,-m'} + \delta_{m,m'}). \end{aligned} \tag{7.9}$$

Here, A is the base area of the disk, Ψ_{nm} is again the radial profile of the respective modes, that was introduced in Sec. 4.1 and δ_{ij} is the Kronecker delta. It becomes clear that the mode coupling to an azimuthal field is only nonzero if $m' = \pm m$, and we can confirm that an azimuthal field given by Eq. 7.7 couples to both modes of a duplet. Moreover, it couples to all radial indices n. This allows us to omit the primes and rewrite the Zeemann term as

$$\mathcal{U}_\mathrm{Z} = -b_\mathrm{RF} e^{i\omega_\mathrm{RF} t} \sum_{n} P_{nm} (c_{n,-m}(t) + c_{nm}(t)) + \mathrm{c.c.} \tag{7.10}$$

The rate equation of a particular mode c_{nm} is then retrieved by taking

$$\frac{\mathrm{d}c_{nm}}{\mathrm{d}t} = -(i\omega_{nm} + \Gamma_{nm}) c_{nm} + i P_{nm} e^{-i\omega_\mathrm{RF} t}. \tag{7.11}$$

Notably, this includes the case of homogeneous pumping ($m = 0$). Again, concrete values for the coupling P_{nm} can be obtained by integrating over the radial profiles. In the following analysis, we shall only use effective values. For example, in the rate equation calculations, we will gauge the coupling $P_\mathbf{0} = P_{n0}$ of the directly excited mode to be in consistence with the numerically determined threshold field $b_{\text{crit}}^{(\text{sim})}$ from Sec. 5.2. However, an approximate dependence of P_{nm} on the radial n has been obtained for this thesis to explain the alternating intensity of the branches obtained by simulation in Sec. 4.3 and can be found in Appx. A.2.

7.2.2 Implementation of pulse modulation

In order to allow for the RF field to be turned on and off at certain times in the rate equation calculations, we replace the constant field magnitude

$$b_{\text{RF}} \to b_{\text{RF}} \cdot w(t) \tag{7.12}$$

by introducing a (real-valued) windowing function $w(t)$. This windowing function is borrowed from the mathematical field of differential geometry [97],

$$w(t) = s(u) \cdot s(t_{\text{PW}}/t_{\text{r}} - u) \quad \text{where} \quad u = (t - t_0)/t_{\text{r}} \tag{7.13}$$

with the auxiliary functions

$$s(u) = \frac{q(u)}{q(u) + q(1-u)} \quad \text{and} \quad q(u) = \begin{cases} 0 & \text{for} \quad u \le 0 \\ \exp(-1/u) & \text{for} \quad u > 0. \end{cases} \tag{7.14}$$

The parameters which enter are the offset time t_0, the width of the pulse t_{PW} as well as the rise/fall time t_{r}. This definition might look over-complicated, but in fact, this windowing function has the advantage of truly vanishing to zero outside of the window defined by t_0 and t_{PW} and being infinitely differentiable everywhere. It might not accurately model the experimental reality but is very well suited for numerical applications. Fig. 7.2 illustrates the shape of the pulse as well as the role of the different parameters. Here, the rise/fall time t_{r} is chosen to be very large for illustration purposes. In all following calculations, a more realistic value of $t_{\text{r}} = 2\,\text{ns}$ is used.

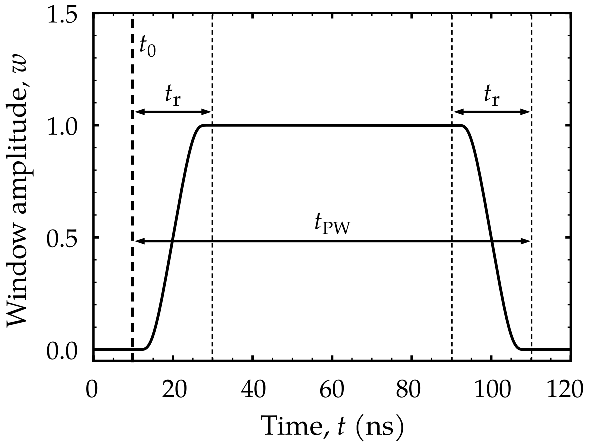

FIGURE 7.2: Windowing function $w(t)$ for the external field pulse with starting time $t_0 = 10\,\text{ns}$, ramp time $t_{\text{r}} = 20\,\text{ns}$ and pulse width $t_{\text{PW}} = 100\,\text{ns}$.

7.3 Modeling of thermal magnons

At finite temperatures, all spin-wave modes in a magnetic systems are excited to a small degree, even in the absence of an external magnetic field. Quantum-mechanically speaking, all the magnon states are occupied according the Bose-Einstein-distribution. In the classical continuum approximation, spin-wave statistics may be described by the Rayleigh-Jeans distribution $|c_{\mathbf{k},th}|^2 \propto T/\omega_{\mathbf{k}}$. The existence of a thermal spin-wave bath prohibits the spin-wave numbers $N_{\mathbf{k}}$ from vanishing to zero. They will rather relax to their corresponding average thermal level $N_{\mathbf{k},\mathrm{th}}$ according to

$$\frac{\mathrm{d}N_{\mathbf{k}}}{\mathrm{d}t} = -2\Gamma_{\mathbf{k}}\left(N_{\mathbf{k}} - N_{\mathbf{k},\mathrm{th}}\right). \tag{7.15}$$

with the analytical solution

$$N_{\mathbf{k}}(t) = (N_{\mathbf{k}}(0) - N_{\mathbf{k},\mathrm{th}})e^{-2\Gamma_{\mathbf{k}}t} + N_{\mathbf{k},\mathrm{th}}. \tag{7.16}$$

Even though the spin-wave amplitudes necessary for nonlinear interactions are far greater than the thermal level, the latter still plays a crucial role in the phenomena observed:

(i) In order for three-magnon scattering to take place, the secondary modes must possess a finite amplitude already, otherwise they will not couple to the directly excited mode.

(ii) When a spin-wave mode is excited by means of a scattering process, its intensity departs exponentially from the thermal level. As a consequence, the point in time when this mode reaches a *detectable* spin-wave number or itself starts to undergo nonlinear processes, will directly depend on the thermal level.

The inclusion of thermal fluctuations into an oscillator equation is usually done by adding a Langevin force $\eta_{\mathbf{k}}(t)$ to the right side,

$$\frac{\mathrm{d}c_{\mathbf{k}}}{\mathrm{d}t} = -i\omega_{\mathbf{k}}c_{\mathbf{k}} - \Gamma_{\mathbf{k}}c_{\mathbf{k}} + \eta_{\mathbf{k}}(t). \tag{7.17}$$

Typically, such a random fluctuating force has a Gaussian profile, with a variance proportional to the temperature of the thermal (magnon) bath. This approach, however, will render the rate equations to *stochastic* differential equations, which recover the thermodynamic behavior described by Eq. 7.15 if treated *on average*. For a single spin-wave mode, this problem has been solved in the theory of nonlinear spin-torque oscillators [17]. Treating a larger set of spin-wave modes with thermal fluctuations as a function of time is not an easy task – and numerically, a very time-consuming one. For our purpose, it is not necessary to treat this problem in a stochastic manner because spin-wave numbers in the nonlinear regime are typically far above the thermal level. The main objective here is rather to examine the time-dependence of the nonlinear dynamics.

For this purpose, a useful approximation was found by the author that treats the thermal magnons as a *coherent* noise. In the following, this approximation will be derived and verified for different thermal levels and relaxation rates. In reminiscence of the previous section, we write the thermal noise as an external magnetic field

$$\eta_{\mathbf{k}}(t) = F_{\mathbf{k}}e^{i(\phi_{\mathrm{th}} - \omega_{\mathbf{k}}t)} \quad \text{with} \quad F_{\mathbf{k}} = \Gamma_{\mathbf{k}}\sqrt{N_{\mathbf{k},th}}. \tag{7.18}$$

which has the same frequency as the corresponding spin-wave mode itself. The assumption is that only the *resonant* Fourier component of the thermal noise will couple to the mode, although it can inherit a random phase ϕ_{th}. The prefactor $F_{\mathbf{k}}$ was chosen, such that a relaxation to the correct thermal level is reached. By including the field given by Eq. 7.18 in the rate equation and averaging over all possible thermal phases, one can recover the correct macroscopic behavior described by Eq. 7.16. This can be seen in Fig. 7.3a, in which exemplary relaxation curves for different thermal phases are plotted together with their ensemble average.

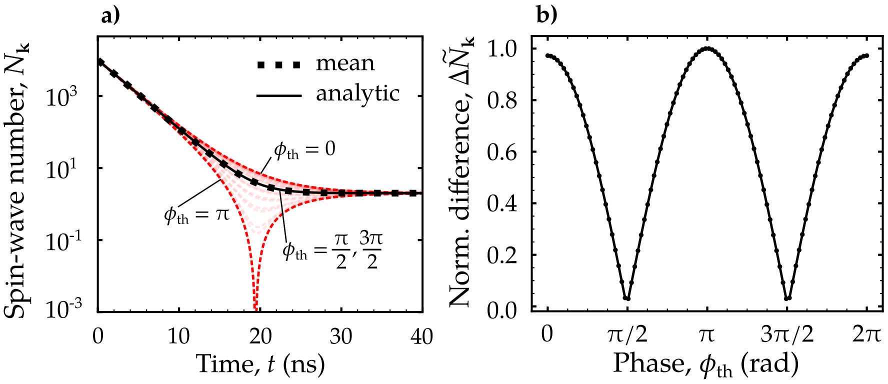

FIGURE 7.3: **a)** Relaxation curves of a single spin-wave mode for different phases ϕ_{th} of the thermal field. The mean is aquired by averaging the results of the rate equations over 100 phases between 0 and 2π. The analytical curve follows Eq. 7.16. Finally, **b)** shows the time-accumulated difference of the rate equation solution for each ϕ_{th} to the analytical curve.

The average curve "mean" – that is, the average of the modulus square of all rate equation solutions – completely coincides with the analytic solution Eq. 7.16. In fact, there are two thermal phases, namely $\phi_{\text{th}} = \frac{\pi}{2}$ and $\phi_{\text{th}} = \frac{3\pi}{2}$, for which the respective rate equations themselves recover the correct thermodynamic behavior. One can verify this by taking the accumulated difference of the rate equations to correct average at each point in time (see Fig. 7.3). This difference is minimized for the aforementioned phases. Without loss of generality, the phase $\phi_{\text{th}} = \frac{\pi}{2}$ will be fixed, allowing the rate equations to be written in the compact form,

$$\frac{\mathrm{d}c_{\mathbf{k}}}{\mathrm{d}t} = -i\omega_{\mathbf{k}}c_{\mathbf{k}} - \Gamma_{\mathbf{k}}(c_{\mathbf{k}} - c_{\mathbf{k},\text{th}}) \quad \text{with} \quad c_{\mathbf{k},\text{th}} = \sqrt{N_{\mathbf{k},th}}\, i e^{-i\omega_{\mathbf{k}}t}. \tag{7.19}$$

To verify this approximation, various relaxation curves of a single mode can be seen for different damping rates and thermal levels in Fig. 7.4. Here again, the modulus square $N_{\mathbf{k}} = |c_{\mathbf{k}}|^2$ of the solution of each rate equation is compared with the corresponding analytical solution. One can see, that the agreement is very good even for large thermal levels.

The last step in this implementation is inclusion of realistic values for the thermal level $N_{\mathbf{k},\text{th}}$. As already mentioned, the thermal level is determined by the Rayleigh-Jeans-distribution

$$N_{\mathbf{k},\text{th}} = \frac{k_B T}{\nu \omega_{\mathbf{k}}}, \tag{7.20}$$

with the temperature T and the Boltzmann constant k_B. The factor ν depends on the normalization of the spin-wave modes $c_{\mathbf{k}}$. It is a remnant of the conversion

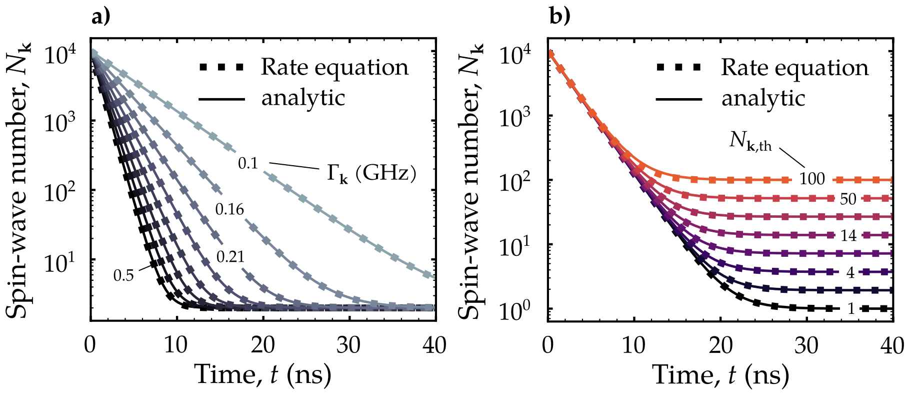

FIGURE 7.4: Verification of the approximation made for the thermal magnons for **a)** different damping rates $\Gamma_{\mathbf{k}}$ and **b)** different thermal levels $N_{\mathbf{k},th}$. The rate-equation results were obtained by numerical integration of Eq. 7.19, whereas the analytical curve follows Eq. 7.16.

of the spin-wave Hamiltonian to frequency units. Thus, in our case $\nu = M_s V/\gamma$. The dispersion $\omega(\mathbf{k})$ was found for different disks in Sec. 4.3. Finally, the thermal distribution for the vortex modes in a 5.1 µm diameter disk at room temperature can be seen in Fig. 7.5.

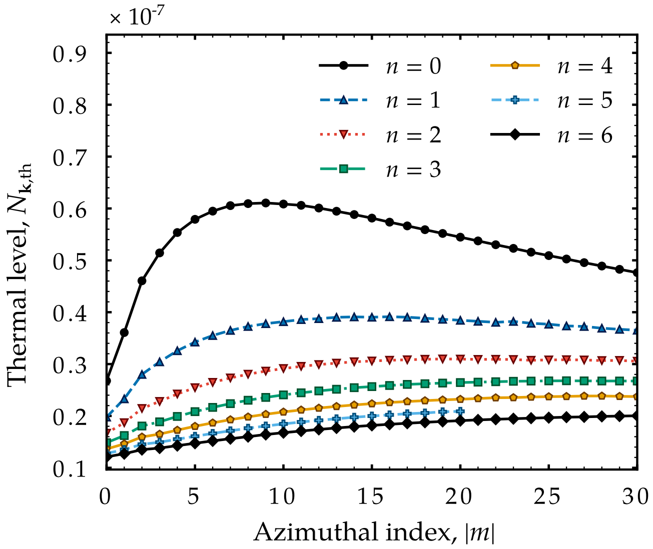

FIGURE 7.5: Thermal distribution $N_{\mathbf{k},\text{th}}$ for the spin-wave modes in a permalloy disk with 5.1 µm diameter and 50 nm thickness. The curves were calculated by means of Eq. 7.20 using a temperature of $T = 293\,\text{K}$ and the dispersion law that was numerically acquired in Sec. 4.3.

In wave-vector space, the modes with $n = 0$ are the most populated ones, as they inhibit the lowest frequencies. For all integrations of the rate equations, it makes sense to set $c_{\mathbf{k}}(0) = c_{\mathbf{k},\text{th}}$. In other words, the modes will always start at the thermal spin-wave numbers.

Just to bring the order of magnitude in the thermal level into perspective, recall from Sec. 2.3.3 that the micromagnetic spin-wave number $N_{\mathbf{k},\text{th}}$ can be related to the quantum-mechanical magnon particle number by $N^{(\text{qm})}_{\mathbf{k},\text{th}} \approx M_s V N_{\mathbf{k},\text{th}}/(\gamma\hbar)$. Inserting the material parameters for a 5.1 µm permalloy disk, one obtains thermal-magnon particle numbers in the order of $N^{(\text{qm})}_{\mathbf{k},\text{th}} \gtrsim 2500$.

7.4 Nonlinear interactions

7.4.1 Three-magnon scattering

Up to this point, we have included all the necessary linear behavior, namely damping, interaction with external microwave fields, as well as coupling to the thermal spin-wave bath. By including nonlinear interactions, the rate equations for the different modes will become coupled and need to be treated as a system of differential equations. The lowest order of nonlinear spin-wave interactions in a magnetic vortex is the three-magnon scattering, which can be retrieved from the corresponding part of the spin-wave Hamiltonian,

$$\mathcal{U}^{(3)} = \sum_{\mathbf{012}} \left(V_{\mathbf{0},\mathbf{12}} c_{\mathbf{1}} c_{\mathbf{2}} c_{\mathbf{0}}^* + \text{c.c.} \right) \delta_{m_1+m_2,m_0}. \tag{7.21}$$

The Kronecker-δ represents conservation of the canonical angular momentum k_ϕ. For the sake of brevity, we again use the short form "$\mathbf{0}$" for $\mathbf{k}_0 \mathrel{\hat{=}} (n_0, m_0)$ and so forth. We have already discussed in Sec. 5.0, that the decay of a radial mode obeys certain selection rules. Let the following channel be the one with the lowest threshold:

A) $(n_0, 0) \rightarrow (n_1, m) + (n_2, -m)$ with $n_1 \neq n_2$

In the previous discussion, not much attention has been given to the fact, that there is indeed a second resonant process with the exact same threshold, namely the one, for which the azimuthal indices of the secondary modes is exchanged (pay attention to the signs!),

B) $(n_0, 0) \rightarrow (n_1, -m) + (n_2, m)$ with $n_1 \neq n_2$.

In fact, every resonant channel found in Sec. 5.1 in fact consists of two channels, which is why $|m|$ was used at that point. The origin of this symmetry is the fact that the modes within one duplet $\pm m$ share the same mode profile and, as a consequence, contribute to the three-magnon efficiency $V_{\mathbf{0},\mathbf{12}}$ in the same way. This leads to the emergence of standing waves at the frequencies of the secondary modes, which is observed both in micromagnetic simulation as well as in BLS experiments. The relation between all of these modes is additionally illustrated in Fig. 7.6.

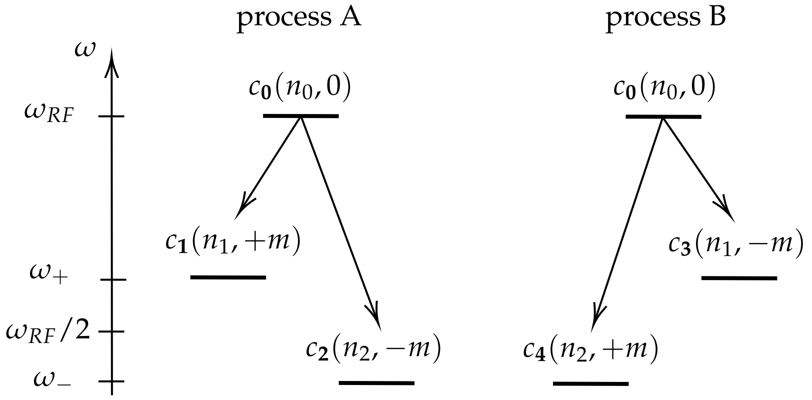

FIGURE 7.6: Visualization of the two equivalent three-magnon decay processes A and B of a radial mode $c_{\mathbf{0}}$ with $(n_0, 0)$ at excitation frequency ω_{RF}.

In summary, one ends up with five rate equations modeling the directly excited mode at ω_{RF} as well as the two degenerate duplets at $\omega_{\mathbf{1},\mathbf{3}}$ and $\omega_{\mathbf{2},\mathbf{4}}$. For the sake of readability, we rename

$$\omega_{\mathbf{1,3}} \equiv \omega_+ \approx \omega_{\mathrm{RF}}/2 + \Delta\omega \quad \text{and} \quad \omega_{\mathbf{2,4}} \equiv \omega_- \approx \omega_{\mathrm{RF}}/2 - \Delta\omega \tag{7.22}$$

for the duplets higher and lower in frequency.[2]

$$\frac{\partial c_{\mathbf{0}}}{\partial t} = -i\omega_{\mathrm{RF}} c_{\mathbf{0}} - \Gamma_0 (c_{\mathbf{0}} - c_{\mathbf{0},\mathrm{th}}) + iP_{\mathbf{0}}^* h_{\perp,\mathbf{0}}^*(t) - iV_{\mathbf{0},\mathbf{12}}(c_{\mathbf{1}}c_{\mathbf{2}} + c_{\mathbf{3}}c_{\mathbf{4}}) \tag{7.23}$$

$$\frac{\partial c_{\mathbf{1}}}{\partial t} = -i\omega_+ c_{\mathbf{1}} - \Gamma_+ (c_{\mathbf{1}} - c_{\mathbf{1},\mathrm{th}}) - iV_{\mathbf{0},\mathbf{12}}^* c_{\mathbf{2}}^* c_{\mathbf{0}} \tag{7.24}$$

$$\frac{\partial c_{\mathbf{2}}}{\partial t} = -i\omega_- c_{\mathbf{2}} - \Gamma_- (c_{\mathbf{2}} - c_{\mathbf{2},\mathrm{th}}) - iV_{\mathbf{0},\mathbf{12}}^* c_{\mathbf{1}}^* c_{\mathbf{0}} \tag{7.25}$$

$$\frac{\partial c_{\mathbf{3}}}{\partial t} = -i\omega_+ c_{\mathbf{3}} - \Gamma_+ (c_{\mathbf{3}} - c_{\mathbf{3},\mathrm{th}}) - iV_{\mathbf{0},\mathbf{12}}^* c_{\mathbf{4}}^* c_{\mathbf{0}} \tag{7.26}$$

$$\frac{\partial c_{\mathbf{4}}}{\partial t} = -i\omega_- c_{\mathbf{4}} - \Gamma_- (c_{\mathbf{4}} - c_{\mathbf{4},\mathrm{th}}) - iV_{\mathbf{0},\mathbf{12}}^* c_{\mathbf{3}}^* c_{\mathbf{0}} \tag{7.27}$$

in which we included the interaction of the directly excited mode $c_{\mathbf{0}}(t)$ with the external pumping field as well as the thermal magnons $c_{\mathbf{k},\mathrm{th}}(t)$ for all modes from the previous sections.

In principle, this set of rate equations could now be integrated and compared with the experimental data. Again, in the case of a non-degenerate system the number of photons detected in a µBLS experiment is proportional to the spin-wave number $N_{\mathbf{k}} = |c_{\mathbf{k}}|^2$. However, in our case, we have degenerate duplets and the focused laser-beam of the µBLS system cannot distinguish between $+m$ and $-m$. As a consequence, we observe standing waves produced by the interference of the modes in one duplet which are exactly in phase. The spin-wave number of these standing waves is then

$$\begin{aligned} N_+ &= |c_{\mathbf{1}} + c_{\mathbf{3}}|^2 \\ N_- &= |c_{\mathbf{2}} + c_{\mathbf{4}}|^2. \end{aligned} \tag{7.28}$$

These standing spin-wave numbers N_+ and N_- together with the spin-wave number of the directly excited mode $N_0 = |c_{\mathbf{0}}|^2$ are the three quantities, which we will compare with experiments in the following analysis.

7.4.2 Amplitude limitation

By comparing our results with experimental data, we find that there is a second class of nonlinear interactions which has a crucial effect on the time-dependence of the mode amplitudes, even for excitation powers not far above threshold. More specific, it is an effect which limits the spin-wave numbers. Once the secondary modes exhibit a certain spin-wave number, they will undergo four-magnon scattering with each other. This leads to a nonlinear frequency shift of these modes and thereby their decoherence with the directly excited mode. Ultimately, this limits the energy flux of the pumping to the secondary modes. Such an amplitude limitation is very common in parallel parametric pumping [4], and therefore, it is not surprising that we observe a similar behavior of the secondary modes in three-magnon scattering.

---

[2] Do not confuse this convention with the sign of azimuthal index $\pm m$.

To include this dephasing effect into the rate equations, one can consider the following four-magnon terms in the Hamiltonian which is diagonal in pairs,

$$\mathcal{U}_S^{(4)} = \sum_{\mathbf{kk}'} W_{\mathbf{kk}'} c^*_{\mathbf{k}} c_{\mathbf{k}} c^*_{\mathbf{k}'} c_{\mathbf{k}'} + \frac{1}{2} \sum_{\mathbf{kk}'} S_{\mathbf{kk}'} c^*_{\mathbf{k}} c_{\mathbf{k}'} c^*_{-\mathbf{k}} c_{-\mathbf{k}'}, \tag{7.29}$$

with $W_{\mathbf{kk}'} = W_{\mathbf{kk}',\mathbf{kk}'}$ and $S_{\mathbf{kk}'} = W_{\mathbf{k},-\mathbf{k},\mathbf{k}',-\mathbf{k}'}$. In our case, $-\mathbf{k} \mathrel{\hat{=}} (n, -m)$. The theory of these parametric interactions is called S-theory [4].

7.5 Comparison with experiment

The results of the rate equations (with and without dephasing) will be compared with time-resolved µBLS experiments (see Fig. 7.7a)[3] for the channel $(1,0) \to (0,\pm 12) + (1,\mp 12)$ at an excitation frequency of $f_{\mathrm{RF}} = 6.1\,\mathrm{GHz}$. The frequencies of the secondary modes according to the micromagnetic simulations (Sec. 4.3) are

$$\begin{aligned} f_+ &= 3.73\,\mathrm{GHz} \\ f_- &= 2.41\,\mathrm{GHz}. \end{aligned} \tag{7.30}$$

These frequencies are close to the experimentally observed ones [20]. Accordingly, the linear damping of the modes is $\Gamma = \alpha_G \epsilon \omega$ (see Sec. 7.1) and the effective coupling of the directly excited mode is set to $P_0 = 11.7\,\mathrm{rad GHz/T}$. This value is chosen such that the growth rate of the secondary modes departs from zero when the pumping field is equal to the threshold field $b_{\mathrm{crit}}^{(\mathrm{sim})} = 1.26\,\mathrm{mT}$ found in Sec. 5.2.[4] A conditional equation for this coupling will be found later in Sec. 8.1. The theoretical value for the three-magnon efficiency for this channel is

$$V_{\mathbf{0},\mathbf{12}}/2\pi = 5.67\,\mathrm{GHz}. \tag{7.31}$$

In the experiments the RF field was applied in pulses of 100 ns. As already mentioned, it is difficult to measure the magnitude of this field experimentally. However, a value of $b_{\mathrm{RF}} = 1.79\,\mathrm{mT}$ provides some agreement of the rate equations with the measurement at hand.

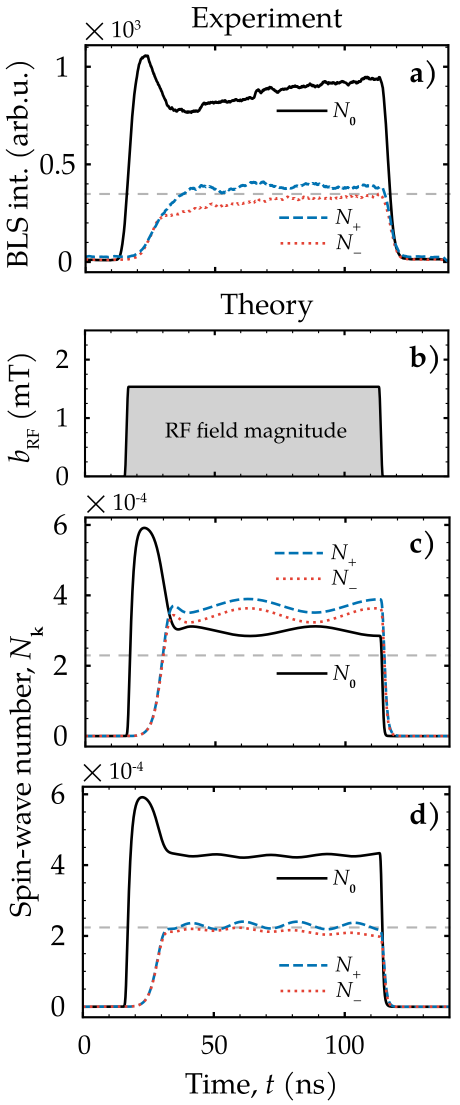

FIGURE 7.7: **a)** Time-resolved BLS measurement of the scattering channel at 6.1 GHz, compared with the results of the corresponding rate equations **c)** without and **d)** with amplitude limitation. The RF-field pulse used for the rate equations is illustrated in **b)**.

First, we consider the case of only three-magnon scattering being present. We see in Fig. 7.7c), that the rate equation theory can model the time-dependence of the experimental data already quite well. After the directly excited mode has reached a certain amplitude, the secondary modes appear and, in return, reduce the amplitude of the directly excited mode. However, in the rate equations, the secondary modes stay at a higher spin-wave number than the directly excited mode after this overshoot. This is in contrast to the experimental observations and means that we have to include the four-magnon terms from Eq. 7.29 which lead to the amplitude limitation of the secondary modes. For simplicity, we choose $W_{\mathbf{kk}'}/2\pi = S_{\mathbf{kk}'}/2\pi = 300\,\mathrm{GHz}$ which gives good agreement with the experimental results (see Fig. 7.7d). The spin-wave numbers of the secondary modes now stay below the directly excited mode. To guide the eye, this level is indicated with a gray dashed line. The oscillations in the equilibrium level of the modes is a result of the detuning from the resonance condition of the three-magnon scattering – in fact they are very sensitive to the detuning and disappear in the case of resonance. Accordingly, these oscillations change if the nonlinear frequency shift is introduced, which arises due to the four-magnon scattering among the secondary modes. Because of these two points, one should take the period of these oscillations with a grain of salt and not try to compare them with experimental results. The good match in this particular case is possibly a coincidence, yet a welcome one. Furthermore, calculating the real values of $T_{\mathbf{kk}'}$ and $S_{\mathbf{kk}'}$ is a rather complicated task and would go beyond the scope of this thesis.[5]

---

[3] These experiments were performed by Toni Hache and the author.

[4] We will find the rigorous definition used for this calibration later in Sec. 8.1.

One can argue, that the reduced BLS intensity of the secondary modes is due to the decreased sensitivity of BLS for larger wave vectors or that the probing laser spot was at a location of the disk, where the secondary modes have nodal lines (standing waves). Although there might be a contribution of this matter, this does not negate an amplitude limitation due to the dephasing mechanism. In fact, we observe this ratio of spin-wave numbers also in the spectra of micromagnetic simulations, where we only look at the frequency-sensitive response of the system. For example, take again a look at the spectrogram in Fig. 5.6a, in which the secondary modes are always much lower in spectral density than the directly excited mode.

---

[5] See for example the humongeous expressions in Eq. 63, 64, 65 and 70 in [39].

Chapter 8

Power dependence

Nonlinear spin-wave dynamics inherit an intrinsic power dependence. Not only a certain power of the excitation field is needed to reach the nonlinear regime, but the dynamics can change considerably when increasing the power even further. For example, the frequencies of the secondary modes will be shifted with increasing excitation field power. Furthermore, in BLS experiments, it has been observed that for larger powers, different secondary modes appear than for lower powers. In this chapter, we will shed light on these phenomena by exploring the nonlinear dynamics further above threshold. It has to be noted, that we will stay in the nonlinear regime that is dominated by three-magnon scattering. The transition to four-magnon scattering dominated dynamics at even larger powers has been studied experimentally by Tobias Hula [23].

After we have established the rate equations of nonlinear dynamics in the previous chapter, we will use them to study the temporal evolution of the three-magnon scattering with increasing excitation field powers. Following up, the nonlinear frequency shift as well as the change in modes will be studied by micromagnetic simulation.

8.1 Change of time scales

As has already been indicated before, it takes less and less time for the secondary modes to appear when the power of the excitation field is increased. Again, this behavior is very characteristic for parametric processes such as the three-magnon scattering in a magnetic vortex. We will take the opportunity to study the different landmarks in the temporal evolution of the mode amplitudes which reveal themselves when changing excitation power. Only saying that the secondary modes appear *earlier* is a rather superficial observation. In fact, there are three different time scales that, with increasing field, change in a seemingly independent manner from each other. The important landmarks of the three-magnon scattering are (in chronological order)

(i) the opening of the three-magnon channel with the lowest threshold (t_{crit}),

(ii) the overshoot of the directly excited mode (t_{OS}), and

(iii) the secondary modes reaching their quasi-equilibrium level (t_{sec}).

In the following two sections, these points will be discussed with respect to their power dependence. All considerations will be made for the case of a 6.1 GHz excitation in a permalloy disk with 5.1 µm diameter and 50 nm thickness.

8.1.1 Critical time of instability

The time delay t_{crit} of the opening of the first three-magnon channel with respect to application of an external RF field can be defined by the time that the directly excited mode needs to reach its critical amplitude. Everything before this point in time is below threshold. Thus, in order to discuss the aforementioned time delay, we only need to consider the linear dynamics of the directly excited mode,

$$\frac{\mathrm{d}c_{\mathbf{0}}}{\mathrm{d}t} = -i\omega_{\text{RF}}c_{\mathbf{0}} - \Gamma_{\mathbf{0}}(c_{\mathbf{0}} - c_{\mathbf{0},\text{th}}) + iP_{\mathbf{0}}b_{\text{RF}}e^{-i\omega_{\text{RF}}t} \tag{8.1}$$

Of course, this assumption is only valid for the channel of the excitation frequency at hand which appears *first*. Otherwise we would have to consider feedback of the secondary modes with the directly excited mode. Above the critical amplitude of the directly excited mode, Eq. 8.1 is not valid anymore. But for now, we can solve this ordinary differential equation analytically (see Appx. A.4). Taken that the external field is turned on at $t = 0$ and with the initial condition $c_{\mathbf{0}}(0) = i\sqrt{N_{\mathbf{0},\text{th}}}$, we obtain

$$N_{\mathbf{0}}(t) = |c_{\mathbf{0}}(t)|^2 = \left[\sqrt{N_{\mathbf{0},\text{th}}} + \frac{P_{\mathbf{0}}b_{\text{RF}}}{\Gamma_{\mathbf{0}}}\left(1 - e^{-\Gamma_{\mathbf{0}}t}\right)\right]^2. \tag{8.2}$$

In Fig. 8.1a, we see the spin-wave number $N_{\mathbf{0}}(t)$ of the direclty excited mode below its cricital amplitude for various excitation field magnitudes.

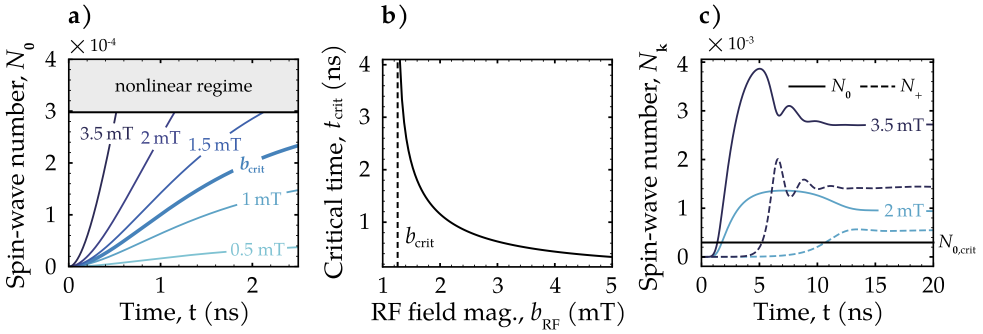

FIGURE 8.1: **a)** Growth of the directly excited mode for different excitation fields, calculated according to Eq. 8.2. The direct mode reaches the nonlinear regime at **b)** the critical time t_{crit}, which decreases with increasing excitation power. **c)** shows integrations of the rate equations for two different excitation fields. For the sake of visibility, only the direct mode and the duplet, which is higher in frequency, are plotted.

Again, the first channel is opened – in other words, the secondary modes will start to rise from their thermal level – when $N_{\mathbf{0}}(t_{\text{crit}}) = N_{\mathbf{0},\text{crit}}$. From this condition, we can write the critical time as

$$t_{\text{crit}} = -\frac{1}{\Gamma_{\mathbf{0}}}\ln\left(1 - \frac{\Gamma_{\mathbf{0}}\left(\sqrt{N_{\mathbf{0},\text{crit}}} - \sqrt{N_{\mathbf{0},\text{th}}}\right)}{P_{\mathbf{0}}b_{\text{RF}}}\right) \tag{8.3}$$

with the critical spin-wave number of the directly excited mode from Sec. 5.2.1,

$$N_{\mathbf{0},\text{crit}} = |c_{\mathbf{0},\text{crit}}|^2 = \frac{\Gamma_{\mathbf{1}}\Gamma_{\mathbf{2}}}{|V_{\mathbf{0},\mathbf{12}}|^2}\left(1 + \frac{\Delta\Omega^2}{(\Gamma_{\mathbf{1}} + \Gamma_{\mathbf{2}})^2}\right). \tag{8.4}$$

One could use Eq. 8.3 as a conditional equation for the effective coupling $P_\mathbf{0}$ of the directly excited mode to an external field. Directly at threshold, the critical time t_crit has to diverge as the argument of the natural logarithm approaches zero (below threshold it is undefined – as it should be). In fact, the effective coupling which is used since the end of the previous chapter in Sec. 7.5 was determined that way.

We see in Fig. 8.1, that the critical time already decreases rather rapidly for fields just above the threshold field b_crit. Already at $2b_\text{crit}$, it takes only about a nanosecond for the direct mode to reach instability. However, if we look at integrations of the full set of rate equations including nonlinear interactions for comparable fields (Fig. 8.1c), we find that the secondary modes *appear* – that is, they reach a considerable spin-wave number – much later. Moreover, the overshoot of the directly excited mode appears long after it has reached instability (compare the orders of magnitude of the spin-wave numbers in Fig. 8.1a and c).

8.1.2 Timescale of overshoot and mode growth

The reason for these different and seemingly independent time scales is that the growth rates of the secondary modes crucially depend on the population of the directly excited mode, i.e.

$$N_\pm \propto e^{\nu t} \quad \text{with} \quad \nu = \nu(N_\mathbf{0}(t), \ldots). \tag{8.5}$$

At $N_\mathbf{0} = N_{\mathbf{0},\text{crit}}$, the growth rate is zero. Just above threshold $b_\text{RF} \gtrsim b_\text{crit}$, the secondary modes will need a large amount of time to *appear* and lead to a considerable feedback on the direct mode. This can take up to 1 µs if the excitation field is only a tiny bit above threshold. Again, this was the reason why a down-sweep of the RF field was performed for determination of the threshold fields in Sec. 5.2. The growth-rate of the secondary modes will increase faster if the direct mode grows faster – that is, for larger RF field powers. Finally, at the point of overshoot t_OS, the pumping of the direct mode is equal to the losses due to the three-magnon scattering (and damping, of course). After that, it is overcompensated, and the secondary modes appear more rapidly until t_sec. Accordingly, the overshoot becomes more narrow in time with increasing power. This last time delay t_sec is the most relevant for applications. After this delay, the secondary modes are at their quasi-equilibrium level. Finding nice analytical expressions like Eq. 8.3 for these larger time delays t_OS and t_sec is not trivial and we have to rely on integrations of the rate equations (see Fig. 8.2a).

From the solutions for different excitation field magnitudes, the overshoot time was extracted as the point in time when $N_\mathbf{0}$ is at its maximum. In a similar fashion, the delay of the secondary modes was extracted as the point in time of most negative curvature in the spin-wave number of the secondary modes $\min_t \left[\partial^2 N_\pm / \partial t^2\right]$ (see Fig. 8.2b). This is the point, when the growth rate of the secondary modes decreases the fastest, indicating the onset of quasi-equilibrium. For t_sec, the theoretical values show a good agreement with data extracted from time-resolved BLS measurements for the same conditions (see. 8.2c). From the measurements, this time delay was approximately found by fitting the time-dependence of a charging capacitor to the direct mode and a sigmoid function to the secondary modes. Moreover, observing the overshoot in experiments is often not easy, as it tends to become very narrow in time. Again, it is difficult to relate b_RF directly to the output power of the microwave generator. That is why the experimental results are plotted as a function of microwave power level. However, one finds agreement in the overall trend as well as the values of t_sec. Similar to the critical time t_crit, the overshoot time t_OS as well as the time when the secondary modes reach quasi-equilibrium t_{sec} decrease rapidly with increasing power, but are overall larger. It has to be noted that none of the time delays can follow a simple exponential law, such as $e^{-\lambda b_{\text{RF}}}$, because no such law – even scaled or shifted – could diverge at finite times. The closer to the threshold, the further apart the time delays are from each other. For excitation field powers further above threshold, other effects have to be taken into account and we will not be able to restrict our discussion to only one channel.

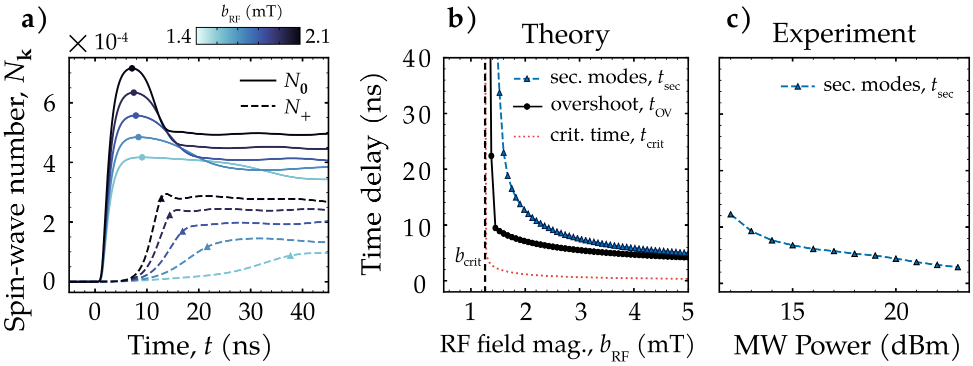

FIGURE 8.2: The power dependence of the different time scales were obtained from **a)** solutions of the rate equations with increasing excitation field (only direct mode and upper duplet are plotted). The time of overshoot (dots) and of the secondary modes reaching quasi-equilibrium (triangles) were extracted from theses curves and plotted in **b)**. There is a good agreement with the experimentally obtain data in **c)**.

8.2 Activation of higher-threshold channels and frequency shift

The situation for excitation field powers which are further above threshold is more complicated. Within micromagnetic simulations, one can observe a change pronounced in the frequency of the secondary modes (see Fig. 8.3a), which was also found experimentally by means of BLS (see Fig. 8.3b). The numerical data was acquired by calculating the power spectrum of CW simulations for different excitation field magnitudes b_{RF} at 6.1 GHz. The experimental data was acquired by Katrin Schultheiß [20]. We can see that, with increasing power, the secondary modes come closer in frequency and then depart again. There are a couple of effects which can contribute to this behavior. First of all, with increasing excitation field power, more and more channels with higher threshold fields will be activated. In the frequency spectra of the micromagnetic simulations in Fig. 8.3a, we can sometimes even see four peaks at the same time (e.g. for $b_{\text{RF}} = 3.5\,\text{mT}$). When more than one pair of azimuthal duplets is excited, we cannot simply take the inverse FFT at the frequencies of the secondary modes and count the periods in azimuthal direction. We have shown in Sec. 4.3, that the inter-mode distance between modes of neighboring $|m|$ can be very small, especially at the bottom of each radial branch. As a consequence, multiple azimuthal modes can appear in a single Fourier component when performing the *discrete* FFT, and the mode indices have to be analyzed more carefully. For this, we calculate the *angular* Fourier transform $\mathcal{G}_m$ of the mode profiles of lower frequency peaks (for which we expect radial index $n = 0$) approximately by

$$\begin{aligned} \mathcal{A}_m &= \langle m_z(\mathbf{r}, \omega_-) \cdot \cos(m\phi) \rangle \\ \mathcal{B}_m &= \langle m_z(\mathbf{r}, \omega_-) \cdot \sin(m\phi) \rangle \\ \mathcal{G}_m &= \sqrt{\mathcal{A}_m^2 + \mathcal{B}_m^2}. \end{aligned} \tag{8.6}$$

As expected (in agreement with Chap. 5), for excitation field powers not far above the threshold field $b_{\text{crit}} = 1.26\,\text{mT}$, we see that only azimuthal modes with $|m| = 12$ are present (see Fig. 8.3b). With increasing power, more and more channels with different azimuthal indices are activated, leading to a shift in the frequency spectrum.

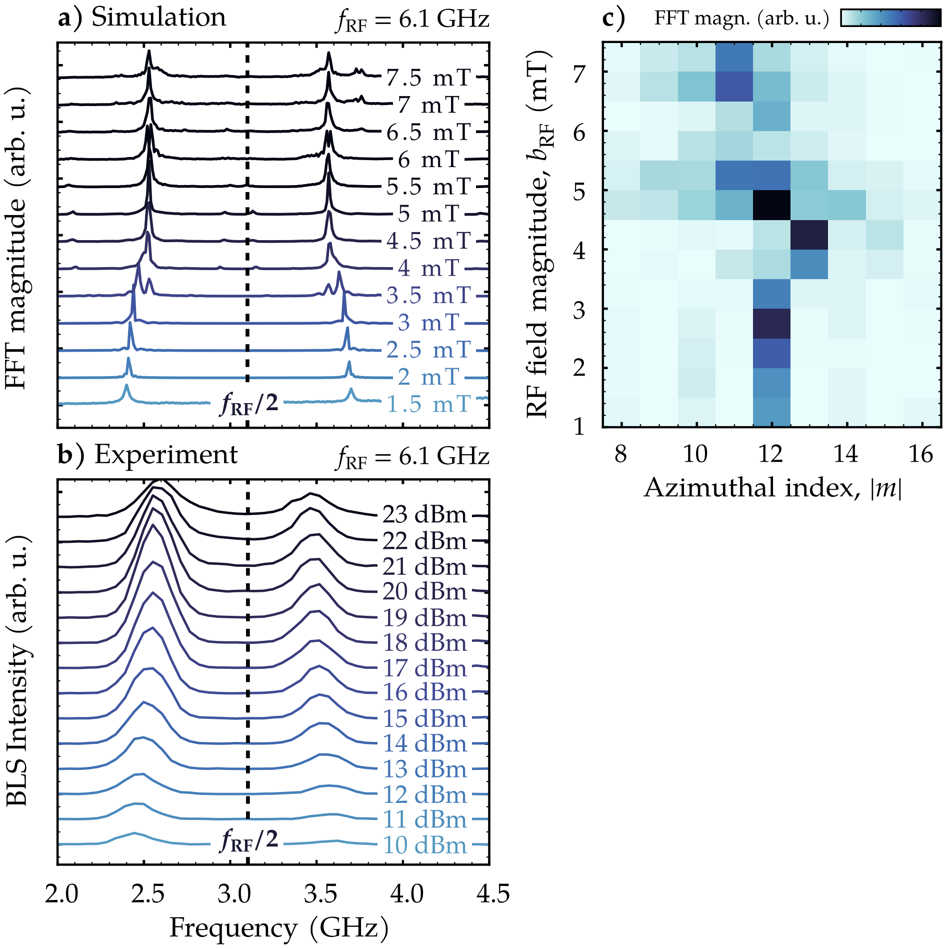

FIGURE 8.3: **a)** Numerical as well as **b)** experimental spectra of a 50 nm thick permalloy disk with 5.1 µm diameter pumped at 6.1 GHz for different excitation field magnitudes / power levels. **c)** shows the result of the angular FFT performed on the numerical data as a function of applied field magnitude.

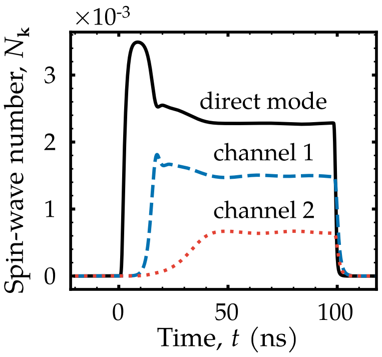

FIGURE 8.4: Prove-of-concept solution of the rate equations including two channels with different thresholds.

An additional contribution to the shift in frequency can be due to the cross-frequency shift of the secondary modes in the presence of the very strongly excited direct mode. Such a shift can happen due to four-wave processes of the form $(\mathbf{0}, \mathbf{k}) \to (\mathbf{0}, \mathbf{k})$ (with the direct mode $\mathbf{0}$ and the respective secondary mode $\mathbf{k}$). However, a concise analysis of this contribution would go beyond the scope as the calculation of the four-magnon coefficients is cumbersome using the present methods. In order to study the temporal evolution of the modes further above threshold, one has to include the additional spin-wave amplitudes in the set of rate equations. This means, for each additional $|m|$, one has to include four more rate equations. A qualitative examination of what happens when more than one channels is activated is shown in Fig. 8.4. The data was acquired using only the five initial rate equations and boldly setting different efficiencies for process A and process B (recall Sec. 7.4.1, there are two equivalent processes with equal probability). However, a proper treatment of the situation further above threshold requires a much more elaborate extension of the rate-equation model developed for this thesis. For this reason, the well-disposed reader is directed to the outlook in Chap. 10 at this point.

Chapter 9

Towards application: Stimulated three-magnon scattering

Up to now, the majority of this thesis has dealt with the fundamental properties of nonlinear spin-wave dynamics in magnetic vortices. We have learned about the origin of the three-magnon-scattering channels in magnetic vortices and their influence on external fields. A model was developed to study the nonlinear temporal evolution of the spin-wave amplitudes and studied the power dependence of the three-magnon scattering. In order to round off this thesis, its last chapter will put the acquired knowledge to use and explore a possible technical application, i.e., the integration of three-magnon scattering within magnonic circuits.

In recent years, nonlinear networks have been given great attention for novel computing techniques such as neural networks [98] or more specifically reservoir computing [99]. In the first case, the nonlinear activation functions of individual neurons play an important role in the training success of a network [100] – thresholds are important. On the other hand, the second case completely relies on the nonlinear digestion of a particular input signal – for example frequency conversion. Until now, most implementations of the aforementioned paradigms are software-based. It is not groundless that the nonlinear system studied in this thesis could be suited for a hardware-based implementation. We have already discussed in the previous sections that the three-magnon scattering in a magnetic vortex inherits a rich set of discrete and well defined channels of mode conversion which can be tuned e.g. by changing the nanodisk dimension (Sec. 5.1), the input power (Chap. 8) or by application of a static in-plane magnetic field (Sec. 6.2), to begin with. Without skating on thin ice by attempting to give a concise proposal for a possible implementation of three-magnon scattering within a nonlinear network, we will use this chapter to explore one of the basic ingredients necessary for it.

In order to built a nonlinear network, one has to find a way to trigger the three-magnon scattering more flexible than just with a large enough RF field. We have already discussed in Sec. 8.1, that the time delay t_{sec} until the secondary modes have reached their quasi-equilibrium level can vary drastically, depending on the input power. Furthermore, information has to be carried to the disk and away from it. The following sections will show using micromagnetic simulation as well as the rate equations developed in Chap. 7, that it is possible to solve these problems by coupling a vortex disk to a magnonic waveguide and using a mechanism to explicitly stimulate three-magnon scattering. The simulations were designed as a prove of principle, however, specifically with experimental realization in mind (which is – to the date of submission of this thesis – in progress). Parts of the following results have been presented at the Magnonics Conference 2019 [101].

9.1 Motivation of stimulation and design

When studying the time-dependence of the three-magnon scattering as a function of excitation field power in Sec. 8.3, we have learned, that the time delay of the secondary modes depends on the growth rate of the directly excited mode. Vice versa, a rapid growth of the secondary modes leads to a considerable feedback on the directly excited mode, as observed in the modulation of the overshoot. This interconnection raises the question of what would happen if we were to excite one of the secondary mode duplets directly (e.g. at ω_-), taken that the direct mode at ω_{RF} is excited below threshold. Can we expect a response at ω_+?

To answer this question, we will need to find a way to excite the secondary modes directly. Recall, that these modes are azimuthal modes which do not inherit a net magnetic moment. As a consequence, there is no coupling to the homogeneous out-of-plane field which is used to excite the direct mode. Using an out-of-plane field with an azimuthal dependence proportional to $\cos(m'\phi)$ is useful for numerics (e.g. to calculate the dispersion, see again Sec. 4.3), but can hardly be realized experimentally – at least not for large $|m|$.

A way out of this misery is to use a magnonic waveguide right next to the disk (see. Fig 9.1). Spin waves propagating in this stripe will produce a dipolar field with a broad spectrum of m-components at the site of the disk. The disk and the waveguide were modeled in a 10 µm × 10 µm grid (roughly keeping the cell size used for previous simulations). The stripe was chosen to be 2 µm wide and, for simplicity, to be of the same thickness and material as the disk (50 nm thick permalloy). Furthermore, the distance between disk and stripe was set to 100 nm. The magnetization within the waveguide was initialized to be longitudinal. In order to mimique an infinitely long waveguide, before relaxation, the magnetization was additionally stabilized by employing a 300 nm wide region of frozen magnetization, housed in a 500 nm wide region of increased damping ($\alpha_G = 0.5$).[1]

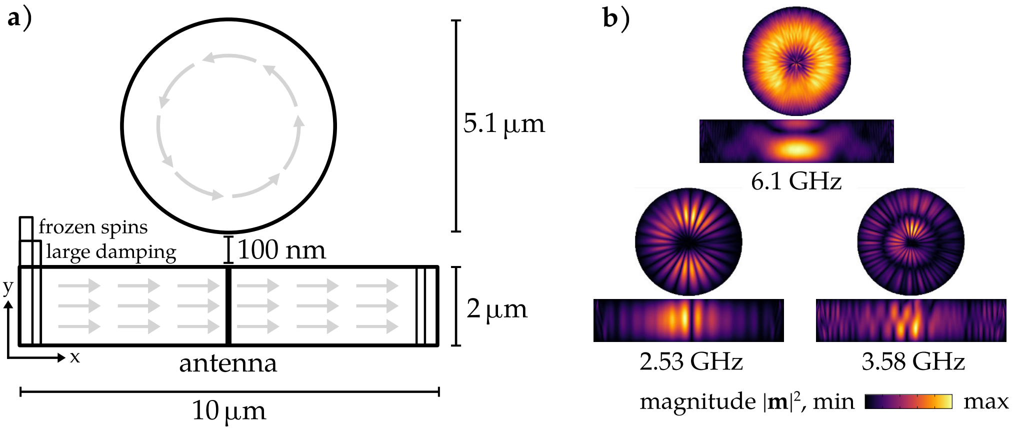

FIGURE 9.1: **a)** Schematics of a vortex disk coupled to a magnonic waveguide and **b)** mode profiles at the frequency of the direct excitation as well as of the secondary modes for when the disk is excited in the nonlinear regime, showing a successfull coupling of the vortex modes into the waveguide.

---

[1] This is done to absorb possible spin waves arriving at the end of the waveguide.

Of course, this particular design could be optimized (e.g. stripe width, materials, artificial anisotropies[2] and so forth), but it will serve its purpose for this prove of concept.

In order to verify that the modes in the waveguide can indeed couple to the azimuthal modes in the disk, the inverse effect was shown. In a first simulation, the disk was pumped above threshold and the dynamics within the waveguide at the frequencies of the secondary modes were probed by means of Fourier analysis. The mode profiles in Fig. 9.1b confirm that the secondary modes produced by three-magnon scattering can couple *back* into a waveguide.

Finally, to inject spin-waves into the waveguide, an RF field with a spatial dependence of $\mathrm{sinc}(k_c x)$ centered with respect to the stripe (see again Fig. 9.1a) is used to excite all wave-vectors with maximum efficiency. The cut-off wave vector k_c is set to correspond to twice the cell size of the simulation. This is, of course, not very close to experimental reality, but was done to achieve more spin-wave amplitude directly next to the disk. In a real, but also prove-of-concept experiment, one could use a microwave antenna on either end of the waveguide to excite standing waves.

9.2 Stimulation and channel selection below threshold

To stimulate the three-magnon scattering, the RF field at the frequency of the directly excited mode $f_{\mathrm{RF}} = 6.1\,\mathrm{GHz}$ is applied to to the disk at a magnitude of $b_{\mathrm{RF},\mathbf{0}} = 1.2\,\mathrm{mT}$, which is just below threshold. Spin waves in the waveguide will be injected at $f_- = 2.4\,\mathrm{GHz}$ with a much higher magnitude of $b_{\mathrm{RF},-} = 15\,\mathrm{mT}$ to ensure a strong enough dipolar field at the site of the disk, which is caused by the propagating spin waves in the waveguide.

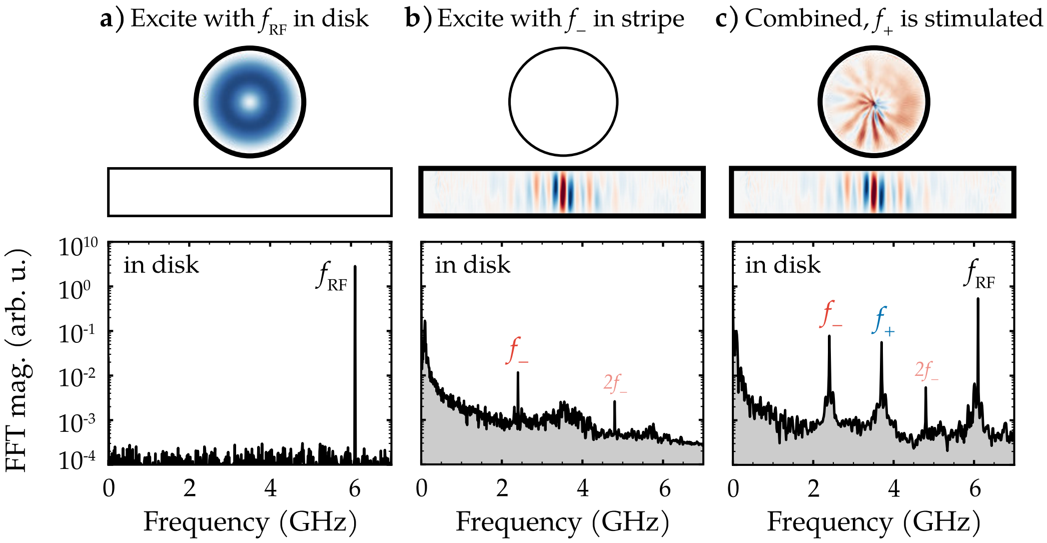

FIGURE 9.2: Stimulated scattering in micromagnetic simulation, showing the power spectrum within the disk for when **a)** only the disk is pumped at f_{RF}, **b)** only the waveguide is pumped at f_-, and **c)** both combined, resulting in an additional signal at f_+.

---

[2] With an in-plane uniaxial anisotropy transversal to the stripe, propagating spin-waves would have a higher group velocity. Such an anisotropy can be achieved e.g. by focused ion beam irradiation [102].

If we only apply the homogeneous RF field $b_{\mathrm{RF},\mathbf{0}}$ to the disk and look at the power spectrum (see Fig. 9.2a) of the disk, we only see a response at the frequency of the directly excited mode.[3] On the other hand, if we only excite with $b_{\mathrm{RF},\mathbf{0}} = 1.2\,\mathrm{mT}$ in the waveguide and look at the power spectrum in the disk, we indeed also see a signal at f_- (see Fig. 9.2b). This means, that spin waves also couple from the waveguide *into* the disk. This is not very surprising, as we have observed the inverse effect in the previous section. Additionally, we see a signal at $2f_-$ which originates from the second harmonic of the mode excited in the waveguide. It is a consequence of the strong excitation, but will not perturb the three-magnon dynamics within the disk.

Finally, when both the lower duplet at f_- as well as the direct mode at f_{RF} are excited by combining the two excitation schemes, we observe an additional peak at the frequency of the upper duplet f_+ (see Fig. 9.2c). Additionally, one can see that the signal at f_- is now also much stronger than in the previous case, whereas the directly excited mode at f_{RF} is weaker. This is already a strong hint, that a three-magnon channel has been activated and that energy is being transferred from the directly excited to the secondary modes.

In order to solidify this hypothesis, we will model the same procedure using the rate-equation theory. To include the effect of the waveguide, we will write the dipolar field of the spin waves propagating in the stripe as an external field $b_{\mathrm{RF},-}$ acting on the duplet modes with frequency f_-. In other words, we have to add the term

$$+\, iP_{\mathbf{2},\mathbf{4}} b_{\mathrm{RF},-} e^{-i\omega_- t} \tag{9.1}$$

to the rate equations of the amplitudes $c_{\mathbf{2}}(t)$ and $c_{\mathbf{4}}(t)$, respectively. The exact value of the product $P_{\mathbf{2},\mathbf{4}} b_{\mathrm{RF},-}$ is not important and will be estimated such that the duplet is excited with a lower power than the direct mode at f_{RF}, similar to the simulation.[4] To have a clearer understanding of what is happening, the second RF field $b_{\mathrm{RF},-}$ will be slightly delayed to the first RF field $b_{\mathrm{RF},\mathbf{0}}$.

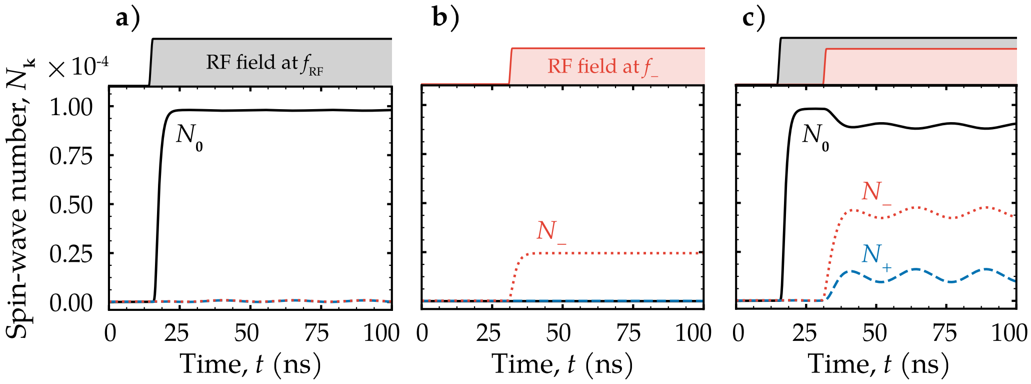

FIGURE 9.3: Verification of stimulation below threshold using the rate equations. The RF field to couple to the lower duplet N_- in **b)** is slightly delayed to the RF field which couples to the direct mode $N_{\mathbf{0}}$ in **a)**. When both are on in **c)**, we see the upper duplet N_+ appearing as well.

In Fig. 9.3, we find confirmation that stimulated scattering is also observed when probed with the rate equations. One can see in Fig. 9.3c that as soon as the second RF field $b_{\mathrm{RF},-}$ is applied in addition to $b_{\mathrm{RF},\mathbf{0}}$, the spin-wave number of the direct mode drops down whereas the secondary modes rapidly reach quasi-equilibrium and even show the oscillations which we attributed to the detuning of the channel from the resonance condition (in Sec. 7.5). In agreement with the results of micromagnetic simulation, the spin-wave number of the pumped duplet N_- is greater when the direct mode $N_\mathbf{0}$ is pumped, too. This confirms the assumption, that a three-magnon channel has been opened. Moreover, the response to the stimulation is almost instant – compared with the very large time delays $t_{\mathrm{sec}} \gg 10\,\mathrm{ns}$ for regular three-magnon scattering just above threshold.

---

[3] For time-consumption reasons, the simulation for this sanity check (seen in Fig. 9.2 was conducted using only a disk without a stripe next to it.

[4] Although the fact that the duplets are being pumped with a lower power than the direct mode is not crucial for stimulation in any way.

Turning back to the micromagnetic simulation, we can extract the mode profiles at f_- and f_+ to confirm, that the signals truely belong to azimuthal modes (see Fig. 9.4a). As expected, these modes satisfy the selection rules (same $|m|$ and different n) of the decay of a radial mode. By bringing all of the aforementioned observations to the table, we can conclude that we have successfully stimulated a three-magnon scattering channel below its threshold.

Up to this point, there is no reason, why stimulation should be restricted to only this particular channel. Indeed, if we change the excitation frequency of $b_{\mathrm{RF},-}$ in the waveguide, we obtain an accordingly mirrored response in the disk (see Fig. 9.4b). Lowering the input frequency f_- will raise the output frequency f_+. In fact, changing the input frequency one can excite different azimuthal modes which belong to a different three-magnon channel (see Fig. 9.4). This corresponds to an activation of one of the silent channels which we encountered in Sec. 5.1.

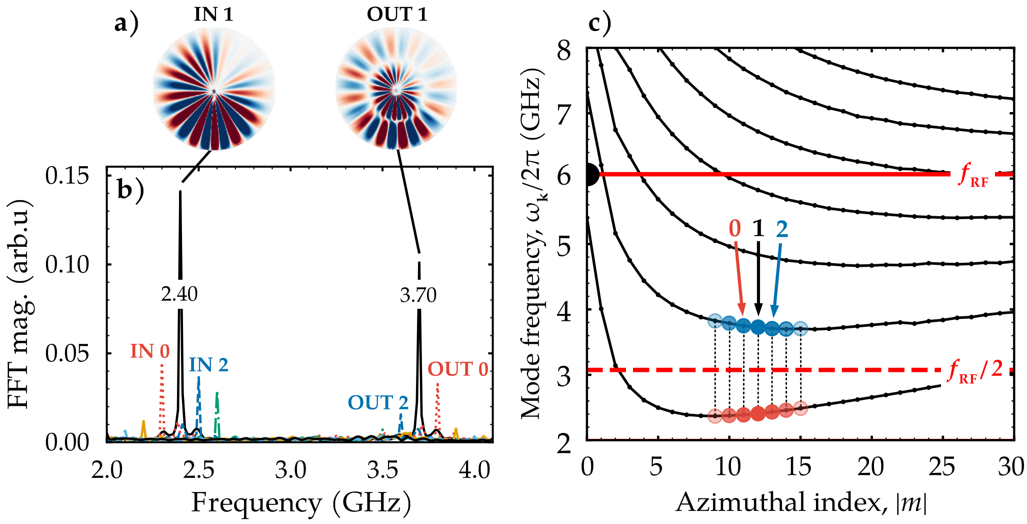

FIGURE 9.4: **a)** Mode snapshots (m_z) reveal, that signals at f_+ and f_- correspond to real azimuthal modes, satisfying the selection rules. **b)** Stimulation can also performed at different frequencies, which results in a possible activation of **c)** all resonant channels.

In conclusion, not only can the additional excitation of one secondary duplet stimulate three-magnon scattering below threshold and with an almost instant response. Stimulation also provides a tool to harness the full set of resonant scattering channels.

9.3 Stimulation above threshold

The situation above threshold is slightly different but also quite interesting. We will study this case using the rate equations. Of course, above threshold, the secondary modes are already present after a certain time delay t_{sec} – which we have shown to be dependent on the magnitude of the excitation field $b_{\mathrm{RF},\mathbf{0}}$ in Sec. 8.1. Below threshold, the response to the simulation was almost instant. We can use this fact to almost completely overcome the time delay above threshold. Quite interestingly, even a very short RF pulse $b_{\mathrm{RF},-}$ at the frequency of one of the duplets is enough to activate a channel in a sustainable manner – taken that this particular channel is the one with the lowest threshold.

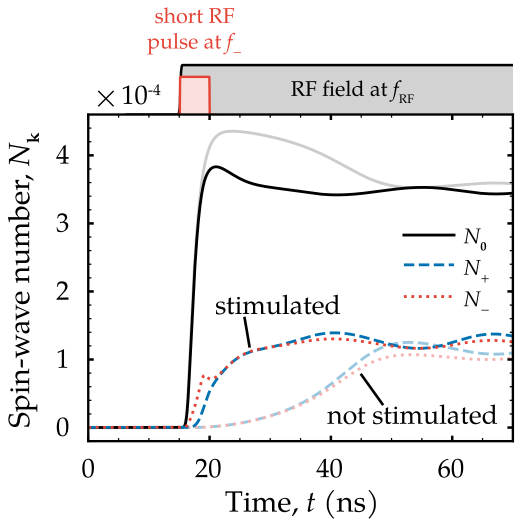

FIGURE 9.5: Stimulated scattering above threshold by applying a short RF pulse to one secondary duplet. The transparent lines show the regular scattering above threshold and without stimulation.

Consider an excitation of the direct mode at 6.1 GHz with $b_{\mathrm{RF},\mathbf{0}} = 1.5\,\mathrm{mT}$, which is sightly above threshold. According to Sec. 8.1, we expect the secondary modes to reach quasi-equilibrium after a delay of $t_{\mathrm{sec}} = 38\,\mathrm{ns}$ with respect to the application of the excitation field (see Fig. 9.5). If we additionally apply the second RF field $b_{\mathrm{RF},-}$ at f_- even for only a short period of 5 ns the secondary modes will appear almost instantly. In Fig. 9.5, the extreme case is shown for when the second RF field as applied at the same time as the first RF field. The secondary modes reach their quasi-equilibrium after approximately 10 ns and remain there even after the second RF pulse has been switched of long before. In conclusion, one can prematurely trigger the secondary modes above threshold with only a short auxiliary RF pulse.

In contrast, if we were to stimulate a silent channel above threshold – which is of course different from the preferred channel with the lowest threshold – the system will only retain in this state as long as the second RF field is applied. As soon as it is switched off, the proper channel with the lowest threshold will be activated again.

Chapter 10

Summary and outlook

Using micromagnetic simulations as well as the classical Hamiltonian formalism for spin waves, this thesis shed light on the nonlinear dynamics in magnetic vortices, with special focus on three-magnon scattering in soft-magnetic permalloy disks. The results were compared with experimental data obtained by means of Brillouin light-scattering microscopy (μBLS). In particular, the following objectives were dealt with:

(i) What is the origin of the three-magnon-scattering channels in magnetic vortex disks? Can we predict them and how are they influenced by external perturbations?

(ii) How can we describe the temporal evolution of the nonlinearly interacting spin-wave modes and how does this evolution depend on the excitation power?

(iii) Can we control and actively trigger (stimulate) nonlinear spin-wave dynamics?

The purpose of this chapter is to highlight the major achievements of this thesis regarding the aforementioned objectives as well as to discuss possible extensions.

In order to predict the possible three-magnon-scattering channels, first the mode profiles as well as the dispersion of the spin-wave modes in a magnetic vortex was numerically calculated for large azimuthal wave vectors while being in agreement with the semi-analytical results of Roman Verba. For this, a method was found to obtain the full dispersion (up to degeneration) from micromagnetic simulations. It was found, that the spin-wave spectrum in a vortex disk favors three-magnon scattering, more specifically the decay of radial modes, as they are well above the azimuthal modes in frequency. The resonant channels were predicted by applying the selection rules of three-magnon scattering to the dispersion and are in agreement with experimental data. Moreover, the secondary modes, which appear first when increasing the excitation power, were obtained from micromagnetic simulations and are in agreement with experiment and theory. For this, a lightweight approach, the total magnetic energy spectrogram, was conceived in order to qualitatively obtain the temporal evolution of the spin-wave intensities from micromagnetic simulations.

The three-magnon scattering was found to be suppressed if a static OOP field is applied which induces a Berry phase to the azimuthal modes and lifts their degeneracy. On the other side, applying a static homogeneous IP field, which displaces the magnetic vortex from the disk center does not suppress three-magnon scattering. Surprisingly, it rather leads to the appearance of additional secondary modes, termed *butterfly modes*, which inherit a qualitatively different mode profile than the ordinary vortex modes. After the prediction by means of micromagnetic simulation, the author suggested μBLS experiments which confirmed the existence of these modes.

In order to study the temporal evolution of the magnon modes, the author learned nonlinear spin-wave theory which was utilized to develop rate equations, that can predict the time-dependence of three-magnon scattering, in agreement with experiments. Within this context, an approximation was achieved to include thermal spin waves. This nonlinear theory was applied to study the power-dependence and uncover the different time-scales of three-magnon scattering. Micromagnetic simulations confirmed a frequency shift of the secondary modes as well as the activation of additional resonant channels with increasing excitation power.

Finally, stimulated three-magnon scattering below and above threshold was demonstrated using micromagnetic simulations and the developed rate equations. It was found, that three-magnon scattering channels can be selected and activated below their natural threshold. This was achieved by coupling the vortex disk to a magnonic waveguide which allows to excite one of the secondary modes next to the direct mode. Moreover, above threshold, the time delay of the secondary modes can be overcome. The possibility to control three-magnon scattering provides means to implement these nonlinear dynamics into magnonic circuits and other possible technical applications.

All in all, the author of this thesis hopes to have provided a broad analysis of the three-magnon scattering in magnetic vortices while leaving room for possible in-depth extensions and follow-up projects, both of a scientific and of a methodical nature. A general extension could be the usage of a different material such as CoFe which has a lower Gilbert damping than permalloy. This, in return, could reduce the input power needed for nonlinear interactions. Furthermore, one could include spin-transfer-torque which leads to an additional amplification of nonlinear behavior by introducing anti-damping. Finally, asymmetric interactions such as the Dzyaloshinskii–Moriya interaction which for example leads to a nonreciprocal nonlinear frequency shift [53] and may strongly influence the selection rules of three-magnon scattering.

The parametric excitation of spin waves in a displaced magnetic vortex opened the route to exotic vortex modes. Understanding the transition in the scattering channels as well as the nature of the butterfly modes requires the calculation of the field-dependent mode spectrum e.g. by means of a dynamic matrix approach.

In order to study the power-dependence of three-magnon scattering in greater detail, the four-magnon scattering efficiencies are necessarily to be calculated, for example using the newly developed vector Hamiltonian formalism. Thinking even further, as the spin waves in a magnetic vortex inherit a discrete mode spectrum, one could write a program which calculates the spin-wave modes using an eigensolver, computes the necessary interaction coefficients and solves the corresponding rate equations for *all* possible modes below a certain cut-off frequency. Such an approach would work without preconceptions about which modes take part in the nonlinear interactions. It would be a very laborious undertaking but, once implemented, could be used for general nonlinear spin-wave dynamics in confined magnetic elements. A similar approach was proposed by Rowlands et al. [103].

The method obtaining the spin-wave intensities from the total magnetic energy of a micromagnetic simulation needs to be properly formalized but could provide a direct bridge between simulations and the classical Hamiltonian formalism. A more proper but more costly approach would be to implement a spatially dependent short-time Fourier transform (STFT).

Finally, the possibility to stimulate three-magnon scattering needs to be confirmed by experiments (in progress). Moreover, in the long-term an extended study could be performed in designing a large network of multiple disks and waveguides in order to deploy it as a reservoir for nonlinear computing.

Own publications and given talks

[20] K. Schultheiss, R Verba, F Wehrmann, K Wagner, L Körber, T Hula, T Hache, A Kákay, A. A. Awad, V Tiberkevich, A. N. Slavin, J Fassbender, and H Schultheiss, "Excitation of Whispering Gallery Magnons in a Magnetic Vortex", *Physical Review Letters*, vol. 122, no. 9, p. 097 202, 2019, ISSN: 0031-9007. DOI: `10.1103/PhysRevLett.122.097202`.

[101] L. Körber, K. Schultheiss, T. Hula, R. Verba, T. Hache, and H. Schultheiss, "Control and stimulation of three-magnon scattering in a magnetic vortex", in *Magnonics Conference 2019*, 2019.

[112] L Körber, K Wagner, A Kákay, and H Schultheiss, "Spin-Wave Reciprocity in the Presence of Néel Walls", *IEEE Magnetics Letters*, vol. 8, pp. 1–4, 2017, ISSN: 1949-307X. DOI: `10.1109/LMAG.2017.2762642`.

[113] N Sato, K Schultheiss, L Körber, N Puwenberg, T Mühl, A. A. Awad, S. Arekapudi, O Hellwig, J Fassbender, and H Schultheiss, "Domain Wall Based Spin-Hall Nano-Oscillators", *Physical review letters*, vol. 123, no. 5, p. 57 204, 2019. DOI: `10.1103/PhysRevLett.123.057204`.

Bibliography

[1] https://doi.org/10.1242/jcs.033340 Schwartz, Martin A.Schwartz, M. A. (2008). The importance of stupidity in scientific research. Journal of Cell Science, 121(11), "The importance of stupidity in scientific research", *Journal of Cell Science*, vol. 121, no. 11, pp. 1771–1771, 2008, ISSN: 0021-9533. DOI: `10.1242/jcs.033340`.

[2] J. S. Russell, "Report on waves", in *14th meeting of the British Association for the Advancement of Science*, vol. 311, 1844, p. 1844.

[3] M. Laurent and N. Kellershohn, "Multistability: a major means of differentiation and evolution in biological systems", *Trends in biochemical sciences*, vol. 24, no. 11, pp. 418–422, 1999.

[4] V. S. L'vov, *Wave turbulence under parametric excitation: applications to magnets*. Springer Science & Business Media, 2012.

[5] H. Poincaré, "Sur le problème des trois corps et les équations de la dynamique", *Acta mathematica*, vol. 13, no. 1, A3–A270, 1890.

[6] R. D. Richtmyer, "Nonlinear Problems: Fluid Dynamics", in *Principles of Advanced Mathematical Physics*, Berlin, Heidelberg: Springer Berlin Heidelberg, 1978, pp. 364–408. DOI: `10.1007/978-3-642-46378-5_17`.

[7] H. A. Dijkstra, *Nonlinear climate dynamics*. Cambridge University Press, 2013.

[8] D. Christodoulou, "Nonlinear nature of gravitation and gravitational-wave experiments", *Physical review letters*, vol. 67, no. 12, p. 1486, 1991.

[9] J. M. Epstein, *Nonlinear Dynamics, Mathematical Biology, and Social Science: Wise Use of Alternative Therapies*. CRC Press, 2018.

[10] V. Makarenko and R. Llinás, "Experimentally determined chaotic phase synchronization in a neuronal system", *Proceedings of the National Academy of Sciences*, vol. 95, no. 26, pp. 15 747–15 752, 1998.

[11] A. Hubert and R. Schäfer, *Magnetic domains: the analysis of magnetic microstructures*. Springer Science & Business Media, 2008.

[12] T. Sebastian, K. Schultheiss, B. Obry, B. Hillebrands, and H. Schultheiss, "Micro-focused Brillouin light scattering: imaging spin waves at the nanoscale", *Frontiers in Physics*, vol. 3, p. 35, 2015, ISSN: 2296-424X. DOI: `10.3389/fphy.2015.00035`.

[13] N. Bloembergen and R. W. Damon, "Relaxation Effects in Ferromagnetic Resonance", *Physical Review*, vol. 85, no. 4, pp. 699–699, 1952, ISSN: 0031-899X. DOI: `10.1103/PhysRev.85.699`.

[14] R. W. Damon, "Relaxation Effects in the Ferromagnetic Resonance", *Reviews of Modern Physics*, vol. 25, no. 1, pp. 239–245, 1953, ISSN: 0034-6861. DOI: `10.1103/RevModPhys.25.239`.

[15] N. Bloembergen and S. Wang, “Relaxation Effects in <i>Para</i> - and Ferromagnetic Resonance”, *Physical Review*, vol. 93, no. 1, pp. 72–83, 1954, ISSN: 0031-899X. DOI: 10.1103/PhysRev.93.72.

[16] S. Kaka, M. R. Pufall, W. H. Rippard, T. J. Silva, S. E. Russek, and J. A. Katine, “Mutual phase-locking of microwave spin torque nano-oscillators”, *Nature*, vol. 437, no. 7057, p. 389, 2005.

[17] A. Slavin and V. Tiberkevich, “Nonlinear Auto-Oscillator Theory of Microwave Generation by Spin-Polarized Current”, *IEEE Transactions on Magnetics*, vol. 45, no. 4, pp. 1875–1918, 2009, ISSN: 0018-9464. DOI: 10.1109/TMAG.2008.2009935.

[18] M. Haidar, A. A. Awad, M. Dvornik, R. Khymyn, A. Houshang, and J. Åkerman, “A single layer spin-orbit torque nano-oscillator”, *Nature Communications*, vol. 10, no. 1, p. 2362, 2019, ISSN: 2041-1723. DOI: 10.1038/s41467-019-10120-4.

[19] A. V. Sadovnikov, S. A. Odintsov, E. N. Beginin, S. E. Sheshukova, Y. P. Sharaevskii, and S. A. Nikitov, “Toward nonlinear magnonics: Intensity-dependent spin-wave switching in insulating side-coupled magnetic stripes”, *Physical Review B*, vol. 96, no. 14, p. 144 428, 2017, ISSN: 2469-9950. DOI: 10.1103/PhysRevB.96.144428.

[20] K. Schultheiss, R Verba, F Wehrmann, K Wagner, L Körber, T Hula, T Hache, A Kákay, A. A. Awad, V Tiberkevich, A. N. Slavin, J Fassbender, and H Schultheiss, “Excitation of Whispering Gallery Magnons in a Magnetic Vortex”, *Physical Review Letters*, vol. 122, no. 9, p. 097 202, 2019, ISSN: 0031-9007. DOI: 10.1103/PhysRevLett.122.097202.

[21] Y. Kobljanskyj, G. Melkov, K. Guslienko, V. Novosad, S. D. Bader, M. Kostylev, and A. Slavin, “Nano-structured magnetic metamaterial with enhanced nonlinear properties”, *Scientific Reports*, vol. 2, no. 1, p. 478, 2012, ISSN: 2045-2322. DOI: 10.1038/srep00478.

[22] F. Wehrmann, “Nichtlineare Spinwellen in magnetischen Vortexstrukturen”, Bachelor Thesis, Technical University of Dresden, 2016.

[23] T. Hula, “Nichtlineare Spinwellen unter zeitlich veränderlichen Anregungsbedingungen”, Master Thesis, University of Applied Sciences Zwickau, 2018.

[24] S. Blundell, *Magnetism in Condensed Matter*. New York: Oxford University Press Inc., 2001, ISBN: 0 19 850592 2.

[25] D. D. Stancil and A. Prabhakar, *Spin waves : theory and applications*. Springer, 2009, ISBN: 9780387778655.

[26] A. G.A. G. Gurevich and G. A.G. A. Melkov, *Magnetization oscillations and waves*. CRC Press, 1996, p. 445, ISBN: 9780849394607.

[27] H. Bethe, “Zur Theorie der Metalle”, *Zeitschrift für Physik*, vol. 71, no. 3-4, pp. 205–226, 1931, ISSN: 1434-6001. DOI: 10.1007/BF01341708.

[28] B. N. Figgis and J. Lewis, “The Magnetic Properties of Transition Metal Complexes”, in, John Wiley & Sons, Ltd, 2007. DOI: 10.1002/9780470166079.ch2.

[29] A. P. G. E.R.P. Novais, “Phase diagram of magnetic configurations for soft magnetic nanodots of circular and elliptical shape obtained by micromagnetic simulation”, 2009.

[30] N. Usov and S. Peschany, “Magnetization curling in a fine cylindrical particle”, *Journal of Magnetism and Magnetic Materials*, vol. 118, no. 3, pp. L290–L294, 1993, ISSN: 0304-8853. DOI: 10.1016/0304-8853(93)90428-5.

[31] J. K. Ha, R. Hertel, and J. Kirschner, “Micromagnetic study of magnetic configurations in submicron permalloy disks”, *Physical Review B*, vol. 67, no. 22, p. 224 432, 2003, ISSN: 0163-1829. DOI: `10.1103/PhysRevB.67.224432`.

[32] A. Akhiezer, V. Bar’yakhtar, and S. Peletmisky, *Spin Waves*. North-Holland, Amsterdam, 1968.

[33] T. L. Gilbert, “A phenomenological theory of damping in ferromagnetic materials”, *IEEE Transactions on Magnetics*, vol. 40, no. 6, pp. 3443–3449, 2004, ISSN: 00189464. DOI: `10.1109/TMAG.2004.836740`.

[34] N. Smith, “Comment on "Adiabatic domain wall motion and Landau-Lifshitz damping"”, *Physical Review B - Condensed Matter and Materials Physics*, vol. 78, no. 21, pp. 1–6, 2008, ISSN: 10980121. DOI: `10.1103/PhysRevB.78.216401`.

[35] M. D’Aquino, “Computation of Magnetization Normal Oscillation Modes in Complex Micromagnetic Systems”, *IFAC Proceedings Volumes*, vol. 45, no. 2, pp. 504–509, 2012, ISSN: 1474-6670. DOI: `10.3182/20120215-3-AT-3016.00088`.

[36] B. A. Kalinikos and A. N. Slavin, “Theory of dipole-exchange spin wave spectrum for ferromagnetic films with mixed exchange boundary conditions”, *Journal of Physics C: Solid State Physics*, vol. 19, no. 35, pp. 7013–7033, 1986, ISSN: 0022-3719. DOI: `10.1088/0022-3719/19/35/014`.

[37] A. M. Ferona and R. E. Camley, “Nonlinear and chaotic magnetization dynamics near bifurcations of the Landau-Lifshitz-Gilbert equation”, *Physical Review B*, vol. 95, no. 10, p. 104 421, 2017, ISSN: 2469-9950. DOI: `10.1103/PhysRevB.95.104421`.

[38] A. Ferona and R. Camley, “Nonlinear power-dependent effects in exchange-coupled magnetic bilayers”, *Physical Review B*, vol. 99, no. 6, p. 064 405, 2019, ISSN: 2469-9950. DOI: `10.1103/PhysRevB.99.064405`.

[39] P. Krivosik and C. E. Patton, “Hamiltonian formulation of nonlinear spin-wave dynamics: Theory and applications”, *Physical Review B*, vol. 82, no. 18, p. 184 428, 2010, ISSN: 1098-0121. DOI: `10.1103/PhysRevB.82.184428`.

[40] D. Slobodianiuk, G. Melkov, K. Schultheiss, H. Schultheiss, and R. Verba, “Nonlinear ferromagnetic resonance in the presence of 3-magnon scattering in magnetic nanostructures”, *IEEE Magnetics Letters*, pp. 1–1, 2019, ISSN: 1949-307X. DOI: `10.1109/LMAG.2019.2913132`.

[41] E. Schlömann, “Technical Report No. R-48”, 1959.

[42] ——, “Fine structure in the decline of the ferromagnetic resonance absorption with increasing power level”, *Physical Review*, 1959, ISSN: 0031899X. DOI: `10.1103/PhysRev.116.828`.

[43] V. L’vov, “Scale invariant theory of fully developed hydrodynamic turbulence-Hamiltonian approach”, *Physics Reports*, vol. 207, no. 1, pp. 1–47, 1991, ISSN: 0370-1573. DOI: `10.1016/0370-1573(91)90081-V`.

[44] Y. Lvov and E. G. Tabak, “A Hamiltonian formulation for long internal waves”, *Physica D: Nonlinear Phenomena*, vol. 195, no. 1-2, pp. 106–122, 2004, ISSN: 0167-2789. DOI: `10.1016/J.PHYSD.2004.03.010`.

[45] G. Falkovich, “Inverse cascade and wave condensate in mesoscale atmospheric turbulence”, *Physical Review Letters*, vol. 69, no. 22, pp. 3173–3176, 1992, ISSN: 0031-9007. DOI: `10.1103/PhysRevLett.69.3173`.

[46] E. A. Kuznetsov, “Weak magnetohydrodynamic turbulence of a magnetized plasma”, *Journal of Experimental and Theoretical Physics*, vol. 93, no. 5, pp. 1052–1064, 2001, ISSN: 1063-7761. DOI: 10.1134/1.1427116.

[47] F. Sahraoui, G. Belmont, and L. Rezeau, “Hamiltonian canonical formulation of Hall-magnetohydrodynamics: Toward an application to weak turbulence theory”, *Physics of Plasmas*, vol. 10, no. 5, pp. 1325–1337, 2003, ISSN: 1070-664X. DOI: 10.1063/1.1564086.

[48] V. E. Zahkarov, V. S. Lvov, and S. S. Starobinets, “Turbulence of spin waves beyond the threshold of their parametric excitation”, *Uspekhi Fizicheskikh Nauk*, vol. 114, pp. 609–654, 1974.

[49] V. S. L’vov, “Solitons and nonlinear phenomena in parametrically excited spin waves”, in *Modern Problems in Condensed Matter Sciences*, vol. 17, Elsevier, 1986, pp. 241–300.

[50] V. S. L’vov and L. A. Prozorova, “Spin waves above the threshold of parametric excitations”, *Spin waves and magnetic excitations. Borovik-Romanov, AS, Sinha, SK (eds.)*, vol. 1, pp. 233–285, 1988.

[51] T. Holstein and H. Primakoff, “Field dependence of the intrinsic domain magnetization of a ferromagnet”, *Physical Review*, 1940, ISSN: 0031899X. DOI: 10.1103/PhysRev.58.1098.

[52] Zakharov, “The instability of waves in nonlinear dispersive media”, *Sov. Phys. JETP*, vol. 24, no. 4, pp. 740–744, 1967.

[53] R. Verba, V. Tiberkevich, and A. Slavin, “Hamiltonian formalism for nonlinear spin wave dynamics under antisymmetric interactions: Application to Dzyaloshinskii-Moriya interaction”, *Physical Review B*, vol. 99, no. 17, p. 174 431, 2019, ISSN: 2469-9950. DOI: 10.1103/PhysRevB.99.174431.

[54] V. S. Tiberkevich, A. N. Slavin, and J.-V. Kim, “Temperature dependence of nonlinear auto-oscillator linewidths: Application to spin-torque nano-oscillators”, *Physical Review B*, vol. 78, no. 9, p. 092 401, 2008, ISSN: 1098-0121. DOI: 10.1103/PhysRevB.78.092401.

[55] J.-V. Kim, V. Tiberkevich, and A. N. Slavin, “Generation Linewidth of an Auto-Oscillator with a Nonlinear Frequency Shift: Spin-Torque Nano-Oscillator”, *Physical Review Letters*, vol. 100, no. 1, p. 017 207, 2008, ISSN: 0031-9007. DOI: 10.1103/PhysRevLett.100.017207.

[56] Y. Zhou, V. Tiberkevich, G. Consolo, E. Iacocca, B. Azzerboni, A. Slavin, and J. Åkerman, “Oscillatory transient regime in the forced dynamics of a nonlinear auto oscillator”, *Physical Review B*, vol. 82, no. 1, p. 012 408, 2010, ISSN: 1098-0121. DOI: 10.1103/PhysRevB.82.012408.

[57] F. Sanches, V. Tiberkevich, K. Y. Guslienko, J. Sinha, M. Hayashi, O. Prokopenko, and A. N. Slavin, “Current-driven gyrotropic mode of a magnetic vortex as a nonisochronous auto-oscillator”, *Physical Review B*, vol. 89, no. 14, p. 140 410, 2014, ISSN: 1098-0121. DOI: 10.1103/PhysRevB.89.140410.

[58] K. Vogt, O. Sukhostavets, H. Schultheiss, B. Obry, P. Pirro, A. A. Serga, T. Sebastian, J. Gonzalez, K. Y. Guslienko, and B. Hillebrands, “Optical detection of vortex spin-wave eigenmodes in microstructured ferromagnetic disks”, *Physical Review B - Condensed Matter and Materials Physics*, vol. 84, no. 17, p. 174 401, 2011, ISSN: 10980121. DOI: 10.1103/PhysRevB.84.174401.

[59] A. Vansteenkiste, J. Leliaert, M. Dvornik, M. Helsen, F. Garcia-Sanchez, and B. Van Waeyenberge, "The design and verification of MuMax3", *AIP Advances*, vol. 4, no. 10, p. 107 133, 2014, ISSN: 2158-3226. DOI: 10.1063/1.4899186.

[60] A. Kakay, *Curvilinear micromagnetism*. [Online]. Available: https://www.hzdr.de/db/Cms?pOid=55944{\&}pNid=107 (visited on 09/17/2019).

[61] J. Sandercock, "A light scattering study of the ferromagnet CrBr3", *Solid State Communications*, vol. 15, no. 10, pp. 1715–1719, 1974, ISSN: 0038-1098. DOI: 10.1016/0038-1098(74)91219-8.

[62] P. Grünberg and F. Metawe, "Light Scattering from Bulk and Surface Spin Waves in EuO", *Physical Review Letters*, vol. 39, no. 24, pp. 1561–1565, 1977, ISSN: 0031-9007. DOI: 10.1103/PhysRevLett.39.1561.

[63] The Table Stable LTD, "High Contrast Tandem Fabry-Pérot In- terferometer TFP-2 HC - Operator Manual. 1", Tech. Rep., 2015.

[64] J. R. Dormand and P. J. Prince, "A family of embedded Runge-Kutta formulae", *Journal of Computational and Applied Mathematics*, vol. 6, no. 1, pp. 19–26, 1980, ISSN: 0771050X. DOI: 10.1016/0771-050X(80)90013-3.

[65] M Buess, T. P. J. Knowles, R Höllinger, T Haug, U Krey, D Weiss, D Pescia, M. R. Scheinfein, and C. H. Back, "Excitations with negative dispersion in a spin vortex", *Physical Review B*, vol. 71, no. 10, p. 104 415, 2005. DOI: 10.1103/PhysRevB.71.104415.

[66] K. Y. Guslienko, A. N. Slavin, V. Tiberkevich, and S.-K. Kim, "Dynamic Origin of Azimuthal Modes Splitting in Vortex-State Magnetic Dots", *Physical Review Letters*, vol. 101, no. 24, p. 247 203, 2008. DOI: 10.1103/PhysRevLett.101.247203.

[67] B. A. Ivanov and C. E. Zaspel, "High Frequency Modes in Vortex-State Nanomagnets", *Physical Review Letters*, vol. 94, no. 2, p. 27 205, 2005. DOI: 10.1103/PhysRevLett.94.027205.

[68] R. Verba, V. Tiberkevich, and A. Slavin, "Damping of linear spin-wave modes in magnetic nanostructures: Local, nonlocal, and coordinate-dependent damping", *Physical Review B*, vol. 98, no. 10, p. 104 408, 2018. DOI: 10.1103/PhysRevB.98.104408.

[69] K. Y. Guslienko, B. A. Ivanov, V. Novosad, Y. Otani, H. Shima, and K. Fukamichi, "Eigenfrequencies of vortex state excitations in magnetic submicron-size disks", *Journal of Applied Physics*, vol. 91, no. 10, p. 8037, 2002, ISSN: 00218979. DOI: 10.1063/1.1450816.

[70] A. Y. Galkin, B. A. Ivanov, and C. E. Zaspel, "Collective modes for an array of magnetic dots in the vortex state", *Physical Review B*, vol. 74, no. 14, p. 144 419, 2006, ISSN: 1098-0121. DOI: 10.1103/PhysRevB.74.144419.

[71] D. D. Sheka, I. A. Yastremsky, B. A. Ivanov, G. M. Wysin, and F. G. Mertens, "Amplitudes for magnon scattering by vortices in two-dimensional weakly easy-plane ferromagnets", *Physical Review B*, vol. 69, no. 5, p. 054 429, 2004, ISSN: 1098-0121. DOI: 10.1103/PhysRevB.69.054429.

[72] B. A. Ivanov, H. J. Schnitzer, F. G. Mertens, and G. M. Wysin, "Magnon modes and magnon-vortex scattering in two-dimensional easy-plane ferromagnets", *Physical Review B*, vol. 58, no. 13, pp. 8464–8474, 1998, ISSN: 0163-1829. DOI: 10.1103/PhysRevB.58.8464.

[73] B. A. Ivanov and C. E. Zaspel, “Magnon modes for thin circular vortex-state magnetic dots”, *Applied Physics Letters*, vol. 81, no. 7, pp. 1261–1263, 2002, ISSN: 0003-6951. DOI: 10.1063/1.1499515.

[74] G. Lv, H. Zhang, X. Cao, F. Gao, and Y. Liu, “Micromagnetic simulations of magnetic normal modes in elliptical nanomagnets with a vortex state”, *Applied Physics Letters*, vol. 103, no. 25, p. 252 404, 2013, ISSN: 0003-6951. DOI: 10.1063/1.4850537.

[75] I. Neudecker, K. Perzlmaier, F. Hoffmann, G. Woltersdorf, M. Buess, D. Weiss, and C. H. Back, “Modal spectrum of permalloy disks excited by in-plane magnetic fields”, *Physical Review B*, vol. 73, no. 13, p. 134 426, 2006, ISSN: 1098-0121. DOI: 10.1103/PhysRevB.73.134426.

[76] B. Taurel, T. Valet, V. V. Naletov, N. Vukadinovic, G. de Loubens, and O. Klein, “Complete mapping of the spin-wave spectrum in a vortex-state nanodisk”, *Physical Review B*, vol. 93, no. 18, p. 184 427, 2016, ISSN: 2469-9950. DOI: 10.1103/PhysRevB.93.184427.

[77] M Buess, Y Acremann, A Kashuba, C. H. Back, and D Pescia, “Pulsed precessional motion on the back of an envelope”, *Journal of Physics: Condensed Matter*, vol. 15, no. 24, R1093–R1100, 2003, ISSN: 0953-8984. DOI: 10.1088/0953-8984/15/24/203.

[78] F. Hoffmann, G. Woltersdorf, K. Perzlmaier, A. N. Slavin, V. S. Tiberkevich, A. Bischof, D. Weiss, and C. H. Back, “Mode degeneracy due to vortex core removal in magnetic disks”, *Physical Review B*, vol. 76, no. 1, p. 014 416, 2007, ISSN: 1098-0121. DOI: 10.1103/PhysRevB.76.014416.

[79] M. Buess, R. Hollinger, T. Haug, K. Perzlmaier, U. Krey, D. Pescia, M. R. Scheinfein, D. Weiss, and C. H. Back, “Fourier Transform Imaging of Spin Vortex Eigenmodes”, *Physical Review Letters*, vol. 93, no. 12, p. 129 902, 2004, ISSN: 0031-9007. DOI: 10.1103/physrevlett.93.129902.

[80] X. Zhu, Z. Liu, V. Metlushko, P. Grütter, and M. R. Freeman, “Broadband spin dynamics of the magnetic vortex state: Effect of the pulsed field direction”, *Physical Review B*, vol. 71, no. 18, p. 180 408, 2005, ISSN: 1098-0121. DOI: 10.1103/PhysRevB.71.180408.

[81] A. Kakay, E. Westphal, and R. Hertel, “Speedup of FEM Micromagnetic Simulations With Graphical Processing Units”, *IEEE Transactions on Magnetics*, vol. 46, no. 6, pp. 2303–2306, 2010, ISSN: 0018-9464. DOI: 10.1109/TMAG.2010.2048016.

[82] W. Scholz, *Magpar*, 2010. [Online]. Available: magpar.net (visited on 09/19/2019).

[83] T. Fischbacher, M. Franchin, G. Bordignon, and H. Fangohr, “A Systematic Approach to Multiphysics Extensions of Finite-Element-Based Micromagnetic Simulations: Nmag”, *IEEE Transactions on Magnetics*, vol. 43, no. 6, pp. 2896–2898, 2007, ISSN: 0018-9464. DOI: 10.1109/TMAG.2007.893843.

[84] M.-A. Bisotti, M. Beg, W. Wang, M. Albert, D. Chernyshenko, D. Cortés-Ortuño, R. A. Pepper, M. Vousden, R. Carey, H. Fuchs, A. Johansen, G. Balaban, L. Breth, T. Kluyver, and H. Fangohr, *FinMag: finite-element micromagnetic simulation tool*, 2018. DOI: 10.5281/zenodo.1216011. [Online]. Available: https://zenodo.org/record/1216011{\#}.XYDDMJMzb1I.

[85] R. Verba, L. Körber, V. Tiberkevich, K. Schultheiss, H. Schultheiss, and A. Slavin, “CC-05. Three-Magnon Splitting in Vortex-State Magnetic Nanodots”, in *MMM 2019 Las Vegas*, Las Vegas, 2019.

[86] L. M. Pham, D. Le Sage, P. L. Stanwix, T. K. Yeung, D Glenn, A. Trifonov, P. Cappellaro, P. R. Hemmer, M. D. Lukin, H. Park, and Others, "Magnetic field imaging with nitrogen-vacancy ensembles", *New Journal of Physics*, vol. 13, no. 4, p. 45 021, 2011.

[87] H Kraus, V. A. Soltamov, F Fuchs, D Simin, A Sperlich, P. G. Baranov, G. V. Astakhov, and V. Dyakonov, "Magnetic field and temperature sensing with atomic-scale spin defects in silicon carbide", *Scientific reports*, vol. 4, p. 5303, 2014.

[88] H. B. Braun and D. Loss, "Berry's phase and quantum dynamics of ferromagnetic solitons", *Physical Review B - Condensed Matter and Materials Physics*, vol. 53, no. 6, pp. 3237–3255, 1996, ISSN: 1550235X. DOI: `10.1103/PhysRevB.53.3237`. arXiv: `9601153 [cond-mat]`.

[89] R. Hertel, W. Wulfhekel, and J. Kirschner, "Domain-wall induced phase shifts in spin waves", *Physical Review Letters*, vol. 93, no. 25, 2004, ISSN: 00319007. DOI: `10.1103/PhysRevLett.93.257202`.

[90] V. K. Dugaev, P Bruno, B Canals, and C Lacroix, "Berry phase of magnons in textured ferromagnets", *Physical Review B*, vol. 72, no. 2, p. 24 456, 2005. DOI: `10.1103/PhysRevB.72.024456`.

[91] L. Giovannini, F. Montoncello, F. Nizzoli, G. Gubbiotti, G. Carlotti, T. Okuno, T. Shinjo, and M. Grimsditch, "Spin excitations of nanometric cylindrical dots in vortex and saturated magnetic states", *Physical Review B*, vol. 70, no. 17, p. 172 404, 2004, ISSN: 1098-0121. DOI: `10.1103/PhysRevB.70.172404`.

[92] F. G. Aliev, J. F. Sierra, A. A. Awad, G. N. Kakazei, D.-S. Han, S.-K. Kim, V. Metlushko, B. Ilic, and K. Y. Guslienko, "Spin waves in circular soft magnetic dots at the crossover between vortex and single domain state", *Physical Review B*, vol. 79, no. 17, p. 174 433, 2009, ISSN: 1098-0121. DOI: `10.1103/PhysRevB.79.174433`.

[93] M. Grimsditch, L. Giovannini, F. Montoncello, F. Nizzoli, G. K. Leaf, and H. G. Kaper, "Magnetic normal modes in ferromagnetic nanoparticles: A dynamical matrix approach", *Physical Review B*, vol. 70, no. 5, p. 054 409, 2004, ISSN: 1098-0121. DOI: `10.1103/PhysRevB.70.054409`.

[94] M. D'Aquino, C. Serpico, G. Miano, and C. Forestiere, "A novel formulation for the numerical computation of magnetization modes in complex micromagnetic systems", *Journal of Computational Physics*, vol. 228, no. 17, pp. 6130–6149, 2009, ISSN: 10902716. DOI: `10.1016/j.jcp.2009.05.026`.

[95] G. Van Rossum and F. L. Drake Jr, *Python tutorial*. Centrum voor Wiskunde en Informatica Amsterdam, 1995.

[96] G. Van Rossum and F. L. Drake, *Introduction To Python 3: Python Documentation Manual Part 1*. CreateSpace, 2009.

[97] L. W. Tu, *An Introduction to Manifolds*. Springer-Verlag GmbH, 2010, ch. 13, pp. 140–146, ISBN: 1441973990.

[98] W. S. McCulloch and W. Pitts, "A logical calculus of the ideas immanent in nervous activity", *The bulletin of mathematical biophysics*, vol. 5, no. Dec, pp. 115–133, 1943. DOI: `10.1007/BF02478259`.

[99] B. Schrauwen, D. Verstraeten, and J. Van Campenhout, "An overview of reservoir computing: theory, applications and implementations", in *Proceedings of the 15th european symposium on artificial neural networks.*, 2007, pp. 471–482.

[100] M. Leshno, V. Y. Lin, A. Pinkus, and S. Schocken, “Multilayer feedforward networks with a nonpolynomial activation function can approximate any function”, *Neural networks*, vol. 6, no. 6, pp. 861–867, 1993.

[101] L. Körber, K. Schultheiss, T. Hula, R. Verba, T. Hache, and H. Schultheiss, “Control and stimulation of three-magnon scattering in a magnetic vortex”, in *Magnonics Conference 2019*, 2019.

[102] M. Urbánek, L. Flajšman, V. Křižáková, J. Gloss, M. Horký, M. Schmid, and P. Varga, “Research Update: Focused ion beam direct writing of magnetic patterns with controlled structural and magnetic properties”, *APL Materials*, vol. 6, no. 6, p. 060 701, 2018, ISSN: 2166-532X. DOI: 10.1063/1.5029367.

[103] S. G. E. te Velthuis, “The 14th Joint Magnetism and Magnetic Materials - Intermag Conference”, *AIP Advances*, vol. 9, no. 5, p. 050 401, 2019, ISSN: 2158-3226. DOI: 10.1063/1.5109432.

[104] E. Wigner, “On the Quantum Correction For Thermodynamic Equilibrium”, *Physical Review*, vol. 40, no. 5, pp. 749–759, 1932, ISSN: 0031-899X. DOI: 10.1103/PhysRev.40.749.

[105] R. Polikar, *The Wavelet Tutorial*. [Online]. Available: http://users.rowan.edu/{~}polikar/WTtutorial.html (visited on 10/01/2019).

[106] V. V. Naletov, “Identification and selection rules of the spin-wave eigenmodes in a normally magnetized nanopillar”, *Physical Review B*, vol. 84, no. 22, p. 224 423, 2011, ISSN: 1098-0121. DOI: 10.1103/PhysRevB.84.224423.

[107] G. E. Andrews, R. Askey, and R. Roy, *Special functions*. Cambridge University Press, 1999, p. 664, ISBN: 9781107325937.

[108] S. van der Walt, S. C. Colbert, and G. Varoquaux, “The NumPy Array: A Structure for Efficient Numerical Computation”, *Computing in Science & Engineering*, vol. 13, no. 2, pp. 22–30, 2011, ISSN: 1521-9615. DOI: 10.1109/MCSE.2011.37.

[109] WarrenWeckesser, *GitHub - WarrenWeckesser/odeintw*. [Online]. Available: https://github.com/WarrenWeckesser/odeintw (visited on 10/01/2019).

[110] S. K. Lam, A. Pitrou, and S. Seibert, “Numba”, in *Proceedings of the Second Workshop on the LLVM Compiler Infrastructure in HPC - LLVM '15*, New York, New York, USA: ACM Press, 2015, pp. 1–6, ISBN: 9781450340052. DOI: 10.1145/2833157.2833162.

[111] T. E. Oliphant, “Python for Scientific Computing”, *Computing in Science & Engineering*, vol. 9, no. 3, pp. 10–20, 2007, ISSN: 1521-9615. DOI: 10.1109/MCSE.2007.58.

[112] L Körber, K Wagner, A Kákay, and H Schultheiss, “Spin-Wave Reciprocity in the Presence of Néel Walls”, *IEEE Magnetics Letters*, vol. 8, pp. 1–4, 2017, ISSN: 1949-307X. DOI: 10.1109/LMAG.2017.2762642.

[113] N Sato, K Schultheiss, L Körber, N Puwenberg, T Mühl, A. A. Awad, S. Arekapudi, O Hellwig, J Fassbender, and H Schultheiss, “Domain Wall Based Spin-Hall Nano-Oscillators”, *Physical review letters*, vol. 123, no. 5, p. 57 204, 2019. DOI: 10.1103/PhysRevLett.123.057204.

Appendix A

Appendix

A.1 Total energy spectogram

A.1.1 Motivation

A spectrogram is a representation used to visualize the time-varying frequency spectrum of a certain signal $u(t)$. Spectrograms are commonly used in electrical engineering, music and speech processing, among other fields. There are many different and sophisticated ways to calculate the spectrogram of a signal, such as the Wigner-distribution [104] or the wavelet transform [105]. Probably, the most rudimentary one is the STFT, for which the signal is divided into small chunks before calculating the Fourier transform for each individual chunk. These chunks are addressed using a time-window function $w(t)$. The STFT of the signal $u(t)$ is then defined by

$$\mathrm{STFT}[u](t,\omega) = \frac{1}{\sqrt{2\pi}} \int_{-\infty}^{\infty} \mathrm{d}\tau \, u(\tau) w(\tau - t) e^{-i\omega\tau}.$$

For this thesis, this method was utilized to acquire the time-dependent spectrum of (possibly long) micromagnetic simulations in a light-weight manner, resolving modes without a net magnetic moment but without having to calculate the full spatially resolved FFT in each time chunk and without producing large amounts of data. It has to be noted, that this method is yet to be properly formalized, as it is in its infancy. There is probably great potential for optimization (e.g. by employing Wigner-distributions and so forth). Here, only a short description will be given.

Next to the full spatially resolved snapshots of the magnetization $\mathbf{M}(\mathbf{r},t)$, also the spatially averaged quantity $\langle \mathbf{M} \rangle (t)$ can be saved during a micromagnetic simulation. By performing Fourier analysis of the average magnetization, one can already obtain a superficial insight into the spectrum of that simulation (e.g. the frequency of the $k = 0$ mode). However, only modes with a net magnetic moment will appear in such a spectrum, because all other modes will have $\langle \mathbf{m}_\mathbf{k} \rangle (t) \equiv 0$. Without having to change the code of the micromagnetic software, one can utilize another quantity – the total magnetic energy $E(t)$ – which is usually provided in most micromagnetic codes. By analyzing the frequency components of this spatially independent quantity one can recover the qualitative time-evolution of the spin-wave modes in the system.

We will first express the idea for a non-varying oscillatory signal for which a Fourier transform over the whole simulation time can be applied. We will find that a resonantly pumped spin-wave mode appears at twice its frequency in the spectrum of the total magnetic energy. The following discussion is then easily be transferred to a discrete STFT of time chunks.

A.1.2 Derivation

The total magnetic energy of a sample with volume V can be written as

$$\mathcal{H}(t) = -\int_V \mathrm{d}^3r\, \mathbf{B}_{\mathrm{ext}}(\mathbf{r},t)\cdot\mathbf{M}(\mathbf{r},t) - \frac{1}{2}\int_V \mathrm{d}^3r\, \mathbf{B}_{\mathrm{int}}(\mathbf{r},t)\cdot\mathbf{M}(\mathbf{r},t). \tag{A.1}$$

The internal field $\mathbf{B}_{\mathrm{int}}$ is produced by the magnetization itself (exchange, dipolar interaction, crystal anisotropy, and so forth) and can itself be written as a linear functional

$$\mathbf{B}_{\mathrm{int}}(\mathbf{r},t) = -\mu_0\hat{\mathbf{N}}(\mathbf{r})\cdot\mathbf{M}(\mathbf{r},t). \tag{A.2}$$

Here, $\hat{\mathbf{N}}$ is a linear tensor operator describing the magnetic self-interactions [39, 53, 106].[1] It becomes apparent, that the total magnetic energy contains a part which is linear (external) and a part which is quadratic (internal) in $\mathbf{M}(\mathbf{r},t)$.

Let us assume that, in the linear regime, we can split the magnetization into a static and a dynamic part according to

$$\mathbf{M}(\mathbf{r},t) = \mathbf{M}_{\mathrm{eq}}(\mathbf{r}) + \mathbf{m}(\mathbf{r},t). \tag{A.3}$$

For now, we will discuss the case of a single mode excited at resonance, $\mathbf{m}(\mathbf{r},t) = \mathbf{m}_{\mathbf{k}}(\mathbf{r})e^{i\omega_{\mathrm{RF}}t}$. For simplicity, we will assume that the external field only has an oscillating component, $\mathbf{B}_{\mathrm{ext}}(\mathbf{r},t) = \mathbf{b}_{\mathrm{RF}}(\mathbf{r})e^{i\omega_{\mathrm{RF}}t}$. We can insert all expressions into the total magnetic energy and perform the integrals,

$$\tilde{\mathcal{H}}(t) = C_0 + C_1e^{i\omega_{\mathrm{RF}}t} + C_2e^{i2\omega_{\mathrm{RF}}t}, \qquad \mathcal{H} = \mathrm{Re}(\tilde{\mathcal{H}}) \tag{A.4}$$

with

$$\begin{aligned} C_0 &= -\int_V \mathrm{d}^3r\,\left(\mathbf{B}_{\mathrm{stat}}\mathbf{M}_{\mathrm{eq}} + \mathbf{M}_{\mathrm{eq}}\hat{\mathbf{N}}\mathbf{M}_{\mathrm{eq}}\right)\\ C_1 &= -\int_V \mathrm{d}^3r\,\left(\mathbf{B}_{\mathrm{stat}}\mathbf{m}_{\mathbf{k}} + \mathbf{M}_{\mathrm{eq}}\mathbf{b}_{\mathrm{RF}} + \mathbf{M}_{\mathrm{eq}}\hat{\mathbf{N}}\mathbf{m}_{\mathbf{k}} + \mathbf{m}_{\mathbf{k}}\hat{\mathbf{N}}\mathbf{M}_{\mathrm{eq}}\right)\\ C_2 &= -\int_V \mathrm{d}^3r\,\left(\mathbf{b}_{\mathrm{RF}}\mathbf{m}_{\mathbf{k}} + \mathbf{m}_{\mathbf{k}}\hat{\mathbf{N}}\mathbf{m}_{\mathbf{k}}\right). \end{aligned} \tag{A.5}$$

The explicit computation of these constants is not necessary for a qualitative evaluation. In the frequency domain, the constant C_0 will only lead to a zero-frequency contribution and, therefore, is not important for further analysis. Although there are exceptions, the constant C_1 is usually very small for most of the simulations in this thesis. First, $\mathbf{B}_{\mathrm{stat}} = 0$ and second $\mathbf{M}_{\mathrm{eq}} \perp \mathbf{b}_{\mathrm{RF}}$ almost everywhere except in the very small vortex core region. The discussion of the remaining two terms in C_1 has to wait until this method has been properly formalized. In most simulations in this thesis (except for Chap. 6, one can set

$$\tilde{\mathcal{H}}(t) \approx C_2e^{i2\omega_{\mathrm{RF}}t}. \tag{A.6}$$

This means, that a resonantly excited mode will appear at twice its frequency in the spectrum of the total magnetic energy. Thus, we have to associate $2\omega_{\mathrm{RF}} \to \tilde{\omega}_{\mathrm{RF}}$. In fact, in order to avoid confusion for the reader, the frequency axis in all spectrograms shown in this thesis was tacitly divided by a factor of two. In Sec. 6.1, there are cases for which C_1 is significant. As the static OOP field increases and with it the product $\mathbf{M}_{\mathrm{eq}} \cdot \mathbf{b}_{\mathrm{RF}}$ (the vortex transforms to a cone-state vortex), there is an increasing contribution at $\omega_{\mathrm{RF}} \to \tilde{\omega}_{\mathrm{RF}}/2$.

---

[1] In the cited publications, the integral kernel of this distributive operator is denoted by $\hat{\mathbf{N}}$ and the operator itself is denoted by $\hat{\mathbf{G}}$. However, in the humble opinion of the author, it makes more sense to switch the two names as the integral kernel is similar to a Green's function, which are commonly referred to by G. In the part of the tensor operator describing the dipolar interaction, the integral kernel is widely even referred to as the *magnetostatic Green's function*.

A.1.3 Example

In Fig. A.1, we see the total energy spectrogram of a CW simulation, for a permalloy disk with 5.1 µm diameter and 50 nm thickness, which was excited with 5 mT at 6.1 GHz. The damping in this simulation is with a value of $\alpha_G = 0.007$ sightly lower than in the rest of the thesis ($\alpha_G = 0.008$).[2] The frequency axis has already been divided by a factor of two. As a sanity check, the full time-independent power spectrum, which was acquired by performing the proper FFT of the magnetization at each grid point, is put next to the spectrogram and shows a satisfactory agreement. Of course, the peaks in the spectrogram are much broader, because the division in small time chunks leads to a reduced frequency resolution.

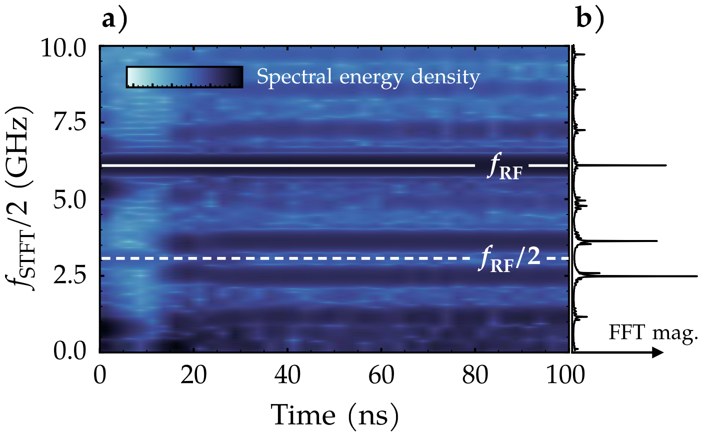

FIGURE A.1: Comparison of the **a)** total magnetic energy spectrogram with the **b)** full spatially resolved power spectrum of a CW simulation at 6.1 GHz and 5 mT of a 5.1 µm permalloy disk with slightly lower damping ($\alpha_G = 0.007$, compared to $\alpha_G = 0.008$ in the rest of this thesis).

A.2 Calculation of the mode coupling to external fieds

Evaluation of the Zeemann energy

To drive spin-wave dynamics in the nonlinear regime, pumping of the modes by an external field has to be included, as well. This coupling is given by the Zeemann energy. In a magnetic vortex, the magnetization lies in-plane with the exception of a small region near the vortex core. In the following analysis we will neglect this region since it will only contribute by a very small amount to the Zeemann energy functional

$$\mathcal{U}_Z = -\frac{\gamma}{M_s V} \int_V \mathrm{d}^3 r\, \mathbf{B}_{\mathrm{ext}}(\mathbf{r}, t) \cdot \mathbf{M}(\mathbf{r}, t). \tag{A.7}$$

---

[2] This is because the simulation was conducted before having all the correct material parameters.

Recall, that the prefactor of $\nu = \gamma / M_s V$ comes from the conversion to frequency units. We express all quantities in a cylindrical coordinate system. For a thin thin disk with $R/L \gg 1$ (with radius R and thickness L) the magnetization will not depend on the out-of-plane coordinate z. Consequently, we can perform this integration right away (and use the two dimensional vector $\boldsymbol{\rho} = (r, \phi)^T$ from thereon),

$$\begin{aligned} \mathcal{U}_Z &= -\frac{\gamma}{M_s V} \int_V \mathrm{d}\rho \, \mathrm{d}\phi \, \mathrm{d}z \;\; r \, \mathbf{B}_{\text{ext}}(r, \phi, z, t) \cdot \mathbf{M}(r, \phi, z, t) \\ &= -\frac{\gamma}{M_s \pi R^2} \int_A \mathrm{d}\rho \, \mathrm{d}\phi \;\; r \, \mathbf{B}_{\text{ext}}(\boldsymbol{\rho}, t) \cdot \mathbf{M}(\boldsymbol{\rho}, t). \end{aligned} \tag{A.8}$$

Following [39], both magnetization and external field are now carried over to complex variables $\hat{\mathbf{M}}$ and $\hat{\mathbf{B}}$ by

$$\hat{\mathbf{M}} = \begin{bmatrix} M_\perp \\ M_\perp^* \\ M_3 \end{bmatrix} \qquad\qquad \hat{\mathbf{B}} = \begin{bmatrix} \frac{1}{\sqrt{2}} B_\perp \\ \frac{1}{\sqrt{2}} B_\perp^* \\ H_3 \end{bmatrix}, \tag{A.9}$$

with $M_\perp = iM_1 + M_2$ and $B_\perp = iB_1 + B_2$. In fact, the Zeemann Hamiltonian retains its form in these variables

$$\mathcal{U}_Z = -\frac{\gamma}{M_s \pi R^2} \int_A \mathrm{d}\rho \, \mathrm{d}\phi \;\; r \, \hat{\mathbf{B}}(\boldsymbol{\rho}, t) \cdot \hat{\mathbf{M}}(\boldsymbol{\rho}, t). \tag{A.10}$$

Here, M_1 and M_2 are again perpendicular and M_3 is parallel to the local magnetization (the components of the external field B_i, respectively). This is important for decomposing the magnetization into canonical variables. Far from the vortex core ($r \gg R_c$) the components are

$$M_1 = -M_z \qquad\qquad M_2 = -M_\rho \qquad\qquad M_3 = M_\phi. \tag{A.11}$$

Writing the Zeemann energy in terms of $\hat{\mathbf{M}}$ and $\hat{\mathbf{B}}$ proves convenient because the magnetization can now easily be connected to the canonical variables by the Schlömann transformation

$$\begin{aligned} \frac{M_\perp}{M_s} &= a(\boldsymbol{\rho}, t) \sqrt{2 - a(\boldsymbol{\rho}, t) a^*(\boldsymbol{\rho}, t)} \\ &\simeq \sqrt{2} a(\boldsymbol{\rho}, t) \left(1 - \frac{1}{4} a(\boldsymbol{\rho}, t) a^*(\boldsymbol{\rho}, t) \right) \\ \frac{M_3}{M_s} &= 1 - a(\boldsymbol{\rho}, t) a^*(\boldsymbol{\rho}, t). \end{aligned} \tag{A.12}$$

To simplify further analysis, we will restrict ourselves to transverse pumping only, since parallel pumping in vortex structures does not coincide with the experimental reality. We can therefore set $B_3 = 0$ and write

$$\begin{aligned} \frac{\hat{\mathbf{B}} \cdot \hat{\mathbf{M}}}{M_s} &= \frac{1}{\sqrt{2} M_s} B_\perp \cdot M_\perp + \text{c.c.} \\ &= B_\perp \cdot a \left(1 - \frac{1}{4} a^* a \right) + \text{c.c.} \end{aligned} \tag{A.13}$$

with c.c. denoting the complex conjugate of the term before. The Hamiltonian is now

$$\begin{aligned}\mathcal{U}_Z &= -\frac{\gamma}{\pi R^2}\int_A \mathrm{d}\rho\,\mathrm{d}\phi\; r\; B_\perp(\boldsymbol{\rho},t)\cdot a(\boldsymbol{\rho},t)\left(1-\frac{1}{4}a(\boldsymbol{\rho},t)a^*(\boldsymbol{\rho},t)\right)+\text{c.c.}\\ &= \underbrace{-\frac{\gamma}{\pi R^2}\int_A \mathrm{d}\rho\,\mathrm{d}\phi\; r\; B_\perp(\boldsymbol{\rho},t)a(\boldsymbol{\rho},t)+\text{c.c.}}_{\mathcal{U}_p}\\ &\quad+\frac{\gamma}{4\pi R^2}\int_A \mathrm{d}\rho\,\mathrm{d}\phi\; r\; B_\perp(\boldsymbol{\rho},t)a(\boldsymbol{\rho},t)a(\boldsymbol{\rho},t)a^*(\boldsymbol{\rho},t)+\text{c.c.}\end{aligned} \tag{A.14}$$

In canonical variables the Zeemann Hamiltonian can be divided into two parts. The first part describes the linear response of the magnetic system to a transversal field. We will call this here the pumping Hamiltonian $\mathcal{U}_p$. The latter part describes processes of three magnons interacting with the field [39]. In the following analysis this last term will be omitted, as it is generally much smaller than the first one. For this reason, in the main thesis, we identify $\mathcal{U}_Z \approx \mathcal{U}_p$. To proceed, the canonical variables can be expanded into normal modes,

$$a(\boldsymbol{\rho},t) = \sum_{n=0}^{\infty}\sum_{m=-\infty}^{\infty} c_{nm}(t)\Psi_{nm}(\rho)e^{im\phi}. \tag{A.15}$$

Here, $c_{nm}(t) = c_{\mathbf{k}}(t)$ are the complex spin-wave amplitudes of the normal modes, but we will write out the mode indices explicitly as they will be important for the coupling RF fields. Again, the radial dependence of these modes is given by $\Psi_{nm}(\rho)$ (as introduced in Sec. 4.1). By evaluating the pumping Hamiltonian in these modes and taking the canonical equations, one can find the rate equations for the spin-wave modes of the form

$$\left[\frac{\partial}{\partial t}+i\omega_{nm}+\Gamma_{nm}\right]c_{nm}(t) = iP_{nm}b^*_{\mathrm{RF}}(t) \tag{A.16}$$

with P_{nm} denoting the coupling of a mode to the field.

Homogeneous transversal fields

In the vast majority of this thesis, the excitation field is spatially homogeneous and has no bias, i.e. $B_\perp(\boldsymbol{\rho},t) = b_{\mathrm{RF}}(t)$. Therefore, we can evaluate the pumping Hamiltonian as

$$\mathcal{U}_p = -b_\perp(t)\sum_{nm} P_{nm}c_{nm}(t)+\text{c.c.} \tag{A.17}$$

with the coupling coefficient

$$\begin{aligned}P_{nm} &= \frac{\gamma}{\pi R^2}\int_A \mathrm{d}\rho\,\mathrm{d}\phi\;\rho\;\Psi_{nm}(\rho)e^{im\phi}\\ &= \frac{\gamma}{\pi R^2}\int_0^R \mathrm{d}\rho\;\rho\;\Psi_{nm}(\rho)\frac{2\sin(\pi m)}{m}.\end{aligned} \tag{A.18}$$

Since m can only take integer values, this coefficient will only survive if $m = 0$, otherwise $\sin(\pi m) = 0$. In the case of $m = 0$, we have

$$\lim_{m\to 0}\frac{2\sin(\pi m)}{m} = 2\pi. \tag{A.19}$$

In fact, we can treat this as a Kronecker-δ as long as m is a principal number.,

$$\frac{\sin(\pi m)}{\pi m} = \delta_{0m}. \tag{A.20}$$

This shows that a homogeneous transversal field cannot couple to azimuthal modes with $m \neq 0$. Therefore we will write P_n instead of P_{n0} with

$$P_n = \frac{2\gamma}{R^2} \int_0^R \mathrm{d}\rho\ \rho\ \Psi_{n0}(\rho). \tag{A.21}$$

Fields with cylindrical spatial symmetry

After examining homogeneous fields, it makes sense to have a look at magnetic fields that exploit the symmetry of the magnetic system and, therefore, the spin-wave modes. In Sec. 4.3, this was utilized to calculate the dispersion of the modes in a vortex. Here, a brief substantiation will be presented. We look again at the case of a field with an azimuthal dependence of $\propto \cos(m'\phi)$, with the principal number m' that counts the azimuthal periods of the field. By expressing the cosine in the spatial profile of the RF field as exponential functions, we can calculate the mode coupling to

$$\begin{aligned} P_{nmm'} &= \frac{\gamma}{\pi R^2} \int_A \mathrm{d}\rho\, \mathrm{d}\phi\ r\ \Psi_{nm}(\rho) e^{im\phi} \cos(m'\phi) \\ &= \frac{\gamma}{2\pi R^2} \int_A \mathrm{d}\rho\, \mathrm{d}\phi\ r\ \Psi_{nm}(\rho) e^{im\phi} \left(e^{im'\phi} + e^{-im'\phi}\right) \\ &= \frac{\gamma}{R^2} \int_0^R \mathrm{d}\rho\ r\ \Psi_{nm}(\rho)(\delta_{m,-m'} + \delta_{m,m'}). \end{aligned} \tag{A.22}$$

We see, that now two indices survive, namely $m = m'$ and $m = -m'$. In other words, a transversal field with a sinusoidal polar dependence will excite both modes of a duplets $\pm m'$ at the same time and with the same efficiency. Moreover, as for the homogeneous case, all radial indices n can be excited. This is illustrated in the pumping term of the Hamiltonian which now reads (for the sake for readability the primes are omitted here)

$$\mathcal{U}_p = -h_m(t) \sum_n P_{nm}(c_{n,-m}(t) + c_{nm}(t)) + \text{c.c.} \tag{A.23}$$

Of course, we could also have started with general fields of this nature and then recover the homogeneous case as the edge case of $m' = 0$. In this case, the last line of Eq. A.22 exactly becomes Eq. A.21.

Qualitative estimate

In order to achieve a qualitative estimate of the coupling coefficients of radial modes to an homogeneous OOP field, one can use the radial profiles found by Buess et al. in [65], which only consider the dipolar interaction,

$$\Psi_n(\varrho) = \kappa_n J_1(k_n\rho) \quad \text{with} \quad \kappa_n = \frac{1}{\sqrt{2}R J_2(j_{1n})}. \tag{A.24}$$

Here J_1 and J_2 are the first and second Bessel function of the first kind, j_{1n} is the nth zero of J_1 and k_n is determined by $k_n R = j_{1n}$. The calculation of the coupling coefficient P_n can be simplified introducing the dimensionless radius $r = \rho/R$. Inserting the radial profile into Eq. A.21, one arrives at

$$\begin{aligned} P_n &= \frac{\sqrt{2}\gamma}{RJ_2(j_{1n})} \int_0^1 \mathrm{d}r\, r J_1(j_{1n} r) \\ &= \frac{\sqrt{2}\gamma j_{1n}}{6RJ_2(j_{1n})} {}_1F_2\left(\left\{\frac{3}{2}\right\}; \left\{2, \frac{5}{2}\right\}; -\frac{j_{1n}^2}{4}\right), \end{aligned} \tag{A.25}$$

with the generalized hypergeometric function ${}_pF_q(\{a_1, \ldots, a_p\}, \{b_1, \ldots, b_q\}, z)$ [107]. If we take a look at the normalized coupling P_n/P_0, one can see that the pumping efficiency rapidly decreases with increasing radial mode index n. Moreover, the coupling does not decrease monotonously, but the coupling for odd radial indices is lower than the one for neighboring even indices. This observation also appears in the power spectra used to calculate the dispersion in Sec. 4.3, Fig. 4.6, in which the spectral intensity is lower for the odd radial modes.

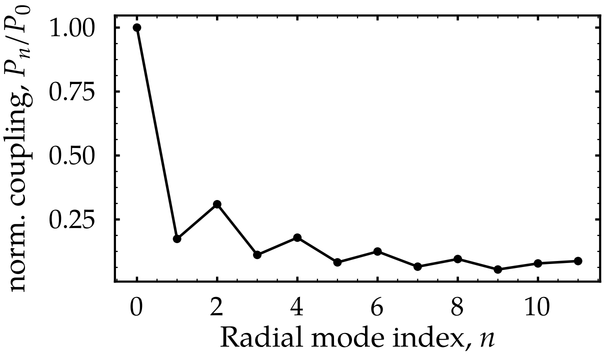

FIGURE A.2: Normalized coupling P_n/P_0 of a vortex mode to an homogeneous OOP field for different radial mode indices n, according to Eq. A.25.

A.3 Implementation of the rate equations in Python

The numerical solution of the rate equations derived in Chap. 7 was carried out in Python3.7 using the following external software packages:

- NumPy 1.16.2 [108]
- odeintw 0.1.2.dev2 [109]
- numba 0.43.1 [110]
- cmath, functools [111]

The core functionality of integrating the set of rate equations was provided by `odeintw` which is a wrapper of the `integrate.odeint` solver provided by the popular `SciPy` package. It allows to integrate complex valued systems of first-order ordinary differential equations (ODEs). When performing mathematical computations on arrays and lists, such as matrix multiplication or even `for`-loops, the `NumPy` package provides a substantial decrease in run time. However, when solving a system of ODEs, single-number computations are carried out at each times step. In such a case, `NumPy` seizes to provide an advantage and can even lead to a serious increase in run time.

In order to perform fast single-number computations, the mathematical functions provided by the `cmath` packages were used instead. Moreover, it is very beneficial to reduce the number of function calls, as they can lead to an unnecessary overhead. For this reason the windowing function introduced in 7.2.2, which includes nested auxiliary functions, is expanded into a single function using only `if-else`-clauses. As an additional performance boost, it is equipped with the `njit`-decorator provided by the `Numba` package, which allows for a translation of Python code into fast mashine code. The aforementioned optimizations led to a speedup of a factor of 16 compared to the `NumPy`-only solution which was initially employed.

A.4 Analytical solution of the rate equation of the direct mode below threshold

We seek the solution of the initial value problem

$$\frac{\mathrm{d}c_0}{\mathrm{d}t} = -i\omega_{\mathrm{RF}}c_0 - \Gamma_0(c_0 - c_{0,\mathrm{th}}) + iP_0 b_{\mathrm{RF}} e^{-i\omega_{\mathrm{RF}}t}, \quad \text{with} \quad c_0(0) = i\sqrt{N_{0,\mathrm{th}}}. \tag{A.26}$$

We will quickly rearrange this by absorbing the thermal spin waves $c_{0,\mathrm{th}}$ into the field term with $\mathcal{P} = \Gamma_0\sqrt{N_{0,\mathrm{th}}} + P_0 b_{\mathrm{RF}}$, such that

$$\frac{\mathrm{d}c_0}{\mathrm{d}t} + (i\omega_{\mathrm{RF}} + \Gamma_0)c_0 = i\mathcal{P}e^{-i\omega_{\mathrm{RF}}t}. \tag{A.27}$$

The general solution is composed by the homogeneous solution (for $\mathcal{P}$) and the particular solution which is obtained by variation of constants,

$$c_0(t) = c_{0,\mathrm{hom}}(t) + c_{0,\mathrm{part}}(t) = \mathcal{C}e^{-\Gamma_0 t}e^{-i\omega_{\mathrm{RF}}t} + \frac{i\mathcal{P}e^{-i\omega_{\mathrm{RF}}t}}{\Gamma_0}. \tag{A.28}$$

The integration constant $\mathcal{C}$ is obtained from the initial condition,

$$c_0(0) = \mathcal{C} + \frac{i\mathcal{P}}{\Gamma_0} = i\sqrt{N_{0,\mathrm{th}}}. \tag{A.29}$$

Thus

$$\begin{aligned} c_0(t) &= ie^{-i\omega_{\mathrm{RF}}t}\left[\frac{\mathcal{P}}{\Gamma_0} + \left(\sqrt{N_{0,\mathrm{th}}} - \frac{\mathcal{P}}{\Gamma_0}\right)e^{-\Gamma_0 t}\right] \\ &= ie^{-i\omega_{\mathrm{RF}}t}\left[\sqrt{N_{0,\mathrm{th}}} + \frac{P_0 b_{\mathrm{RF}}}{\Gamma_0}\left(1 - e^{-\Gamma_0 t}\right)\right]. \end{aligned} \tag{A.30}$$

Now, taking the modulus square, one recovers Eq. 8.2.

Selbstständigkeitserklärung

Hiermit erkläre ich, Lukas Körber, dass ich diese Abschlussarbeit "Theory and simulation on nonlinear spin-wave dynamics in magnetic vortices" im Rahmen der Betreuung am Insitut für Ionenstrahlphysik und Materialforschung des Helmholz-Zentrums Dresden - Rossendorf ohne unzulässige Hilfe Dritter verfasst und alle Quellen als solche gekennzeichnet habe.

Gezeichnet:

Datum: